Characterization of Bipolar Membranes for Electrochemical Applications

J. A. H. Verdonk

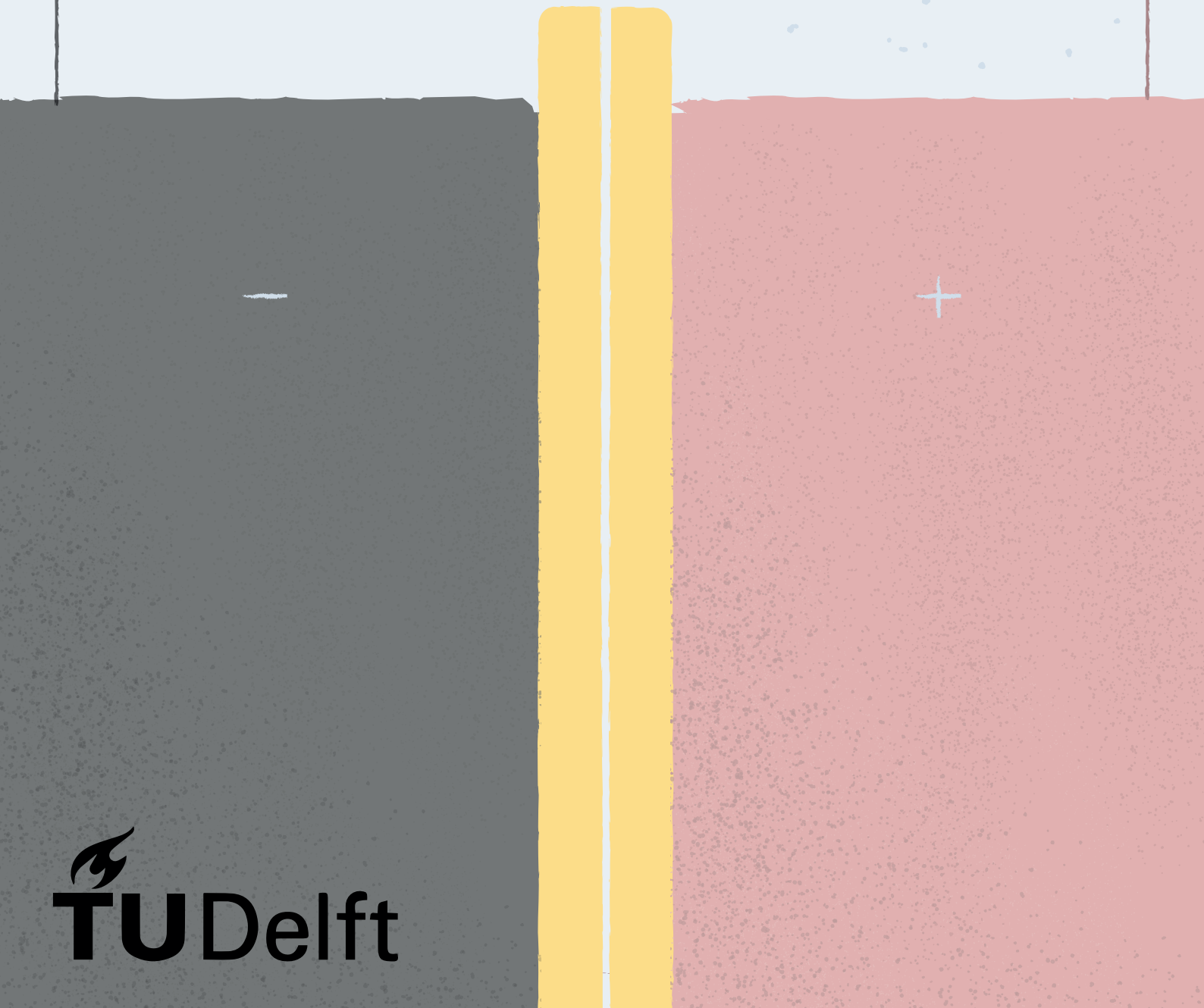

TU Delft

Characterization of Bipolar Membranes for Electrochemical Applications

by

Joost Verdonk

to obtain the degree of Master of Science

at the Delft University of Technology,

to be defended publicly on Thursday July 4, 2019 at 10:00 AM.

Student number:	4251628	
Project duration:	October 1, 2018 – July 4, 2019	
Thesis committee:	Dr. W.A. Smith,	TU Delft, supervisor
	Prof. dr. ir. J.J.C. Geerlings,	TU Delft
	Dr. ir. D.A. Vermaas,	TU Delft
Daily supervisor:	Ir. M.A. Blommaert,	TU Delft

An electronic version of this thesis is available at `http://repository.tudelft.nl/`.

TU Delft

Preface

The past months have been a very interesting and remarkable experience. At the beginning of my thesis I had never heard of the term 'bipolar membrane' and now, eight months later, I have written an entire report on the subject. The field of electrochemistry has really intrigued me and I am amazed how much I have learned regarding the topic in a relative short time frame. Naturally, this was not possible without the help and support from the people around me.

First of all, my biggest thanks go to my daily supervisor Marijn Blommaert. Thank you Marijn, for helping me settle in the lab, for guiding me during this thesis and for always helping me out whenever I ran into a problem. I would also like to thank Wilson Smith for facilitating this research project and Hans Geerlings and David Vermaas for taking place in my thesis committee. Furthermore, I would like to acknowledge the MECS group for the interesting weekly meetings and for assisting me in the lab. A special thanks goes to Martin who helped me out with the NMR measurements. Additionally, I would like to thank Baukje Tersptra (Radiation Science & Technology Department) for all the ICP-OES measurements she performed.

Next, I would like to thank Minouk, Alexandra and Gaius for all the fun lunches and relaxing walks around the faculty. They were there for the entire duration of my thesis and they really helped me to stay focused and motivated. Minouk deserves extra credit all her help during my thesis and for the beautiful figures that she designed, which I am very grateful for. I would also like to thank my roommates, friends and family for supporting me whenever I needed them. And last but not least, I would like to thank Joris and Ellis for designing a beautiful cover page for this report.

I am grateful for the knowledge of electrochemistry that I acquired these last few months and hopefully I can someday make good use of it in a future endeavour!

Joost Verdonk
Delft, June 2019

Abstract

Greenhouse gas concentrations are ever increasing in the Earth's atmosphere, causing the global temperature to have reached over a 1.0 °C increase relative to pre-industrial levels. A further increase in this temperature can have disastrous effects on our society, thus the increase in greenhouse gases must be attenuated. Electrochemical water splitting and CO_2 reduction have been identified as promising routes to generate carbon neutral fuels. Efforts are made to increase the performance of the electrochemical configuration, however, a stable system that is applicable for industrial applications has not yet been achieved. The research field is ever changing and thus the choice of electrolytes and catalysts fluctuates. There is a desire for a stable configuration that can cope with these changes. A bipolar membrane (BPM) has the unique ability to pair two different electrolytes which can be optimized for their respective oxidation and reduction reactions. A BPM configuration is applicable for high performance rates, since it splits water at the interface layer, therefore accelerating the rate of ion transport compared to a conventional monopolar membrane. Despite the advantages of the BPM, there are still knowledge gaps on the exact mechanism behind the BPM and its electrochemical response. It is known that co-ion permeation through the BPM lowers the efficiency of the water dissociation reaction, thus decreasing the stability of the system in the long run. Therefore, it is relevant to further explore the effect of ion characteristics on ion cross-over.

This research focuses on the degree of ion cross-over for a variety of electrolytes, with different pK_a values. Multiple buffer solutions were tested at the cathode in a flow cell configuration for a current density range of 0-150 mA/cm^2. The anolyte was a 0.5M NaOH solution for every tested catholyte. All experiments were performed for a constant period of time, after which the electrolytes were analysed for ion cross-over.

It has been observed that the pK_a value, the mobility and the valence of an ion influence the ion cross-over through the bipolar membrane. A large ion size decreases the ion cross-over to negligible amounts, for permeation through the membrane is limited. However, high BPM potentials have been detected for large molecules due to an assumed diffusion boundary layer, which increases the resistance at the cation exchange layer. For all tested catholytes low co-ion permeation (%) is measured at high current densities. Thereupon, the age of the BPM significantly affects the degree of ion cross-over. This observation is stronger for the anion exchange layer, for its permselectivity is lower. Additionally, the catholyte choice appears to influence the opposing Na^+ flow from the anolyte to the catholyte.

This thesis demonstrates that for high current densities co-ion permeation reaches negligible values. In addition, the results indicate that an ideal ion size region exists, where ions cannot permeate the membrane easily, yet do not form a diffusion boundary layer (thus do not increase the BPM potential). This knowledge is relevant for optimizing the BPM configuration for industrial applications, since a clever choice of electrolytes can further stabilize the system. Future research should focus on up-scaling the set-up and testing the commercial BPM for stability and permselectivity.

Keywords: ion exchange membrane, bipolar membrane, ion cross-over, co-ion permeation, electrochemical CO_2 reduction, water splitting, electrochemical response, electrolytes, ion mobility, pK_a, BPM voltage

List of Symbols

Roman Symbols

A	Surface area	cm^2
C_j	Concentration of species j	$M, mol \cdot cm^{-3}$
C_O	Concentration oxidised species	$mol \cdot L^{-1}$
C_R	Concentration reduced species	$mol \cdot L^{-1}$
D_j	Diffusion coefficient of species j	$cm^2\,s^{-1}$
E	(a) Potential of an electrode versus a reference (b) Thermodynamic potential of a reaction	V
e^-	Electron	
E^0	(a) Standard potential of an electrode or a couple (b) Standard thermodynamic potential of a half-reaction	V
E_{eq}	Equilibrium potential of an electrode	V
F	Faraday's constant	$96{,}485.4\ C{\cdot}mol^{-1}$
i	Current	A
j	Current density	$A \cdot cm^{-2}$
J_j	Flux of species j	$mol \cdot cm^{-2}\,s^{-1}$
K_a	Acid dissociation constant	
k_b	Boltzmann constant	$1.38064852 \times 10^{-23} m^2\,kg \cdot s^{-2}\,K^{-1}$
L	Conductance	$S{=}\Omega^{-1}$
n	Number of electrons in reduction or oxidation reaction	
Q	Charge	C
R	Gas constant	$8.314\ J \cdot mol^{-1}\,K^{-1}$
R	Resistance	Ω
R_S	Stokes radius	$Å{=}\ 10^{-10} m$
R_s	Solution resistance	Ω
R_u	Uncompensated resistance	Ω
T	Temperature	K
u_j	Mobility of ion j	$cm^2\,V^{-1}\,s^{-1}$

v	Velocity	$m \cdot s^{-1}$
z	Valence	
z_j	Valence of species j	
MW	Molecular weight	$g \cdot mol^{-1}$

Greek Symbols

α	Radius of a perfect sphere	Å$= 10^{-10}$m
$\bar{\mu}$	Electrochemical potential	$kJ \cdot mol^{-1}$
$\Delta\phi$	Electrostatic potential difference between two points or phases	V
η	Dynamic viscosity of a solution	$Pa \cdot s$
η	Overpotential	V
κ	Conductivity	$S \cdot cm^{-1}$
ϕ	Electrostatic potential	V

Abbreviations

AEL	Anion exchange layer
AEM	Anion exchange membrane
BPM	Bipolar membrane
CE	Counter electrode
CEL	Cation exchange layer
CEM	Cation exchange membrane
CO2RR	Carbon dioxide reduction reaction
EIS	Electrochemical impedance spectroscopy
HER	Hydrogen evolution reaction
ICP-OES	Inductive Coupled Plasma- Optical Emission Spectrometry
IL	Interface layer
NMR	Nuclear Magnetic Resonance
OER	Oxygen evolution reaction
PTFE	Polytetrafluoroethylene
PVDF	Polyvinylidene fluoride
RE	Reference electrode
RHE	Reversible hydrogen electrode
SE	Sense electrode

SHE Standard hydrogen electrode

WDR Water dissociation reaction

WE Working electrode

List of Figures

List of Tables

Contents

1

Introduction and problem statement

Since the Industrial Revolution, the global consumption of fossil energy has increased more than 1300-fold, and has been estimated to be more than 140,000 TWh (terawatt-hour) in 2017 [10]. The burning of these fossil fuels produces greenhouse gas emissions, and the concentration of these greenhouse gases (GHG) in the Earth's atmosphere have been steadily rising in the last century. It has been scientifically proven that greenhouse gas emissions have increased the average global temperature with 1.0 °C relative to pre-industrial times, causing noticeable climate changes all over the world [10]. Figure 1.1a gives the global temperature change since 1850, showing that the average accumulated temperature change is close to 1.0 °C. Carbon dioxide (CO_2) makes up the majority of these greenhouse gases emissions, and its exponential rise can be seen in figure 1.1b. The Intergovernmental Panel on Climate Change (IPCC) has made an extensive analysis of the potential impacts of climate changes in 2014 and has repeated this message several times the last couple of years [11]. This report contributed to the decision of the UN member parties to set a target of limiting average warming to 2.0 °C above pre-industrial temperatures. The European Commission has ruled that CO_2 emissions must be reduced to 0 by 2050, thus limiting the temperature increase to 1.5 °C (which was actually recommended by the IPCC in 2018) [12, 13].

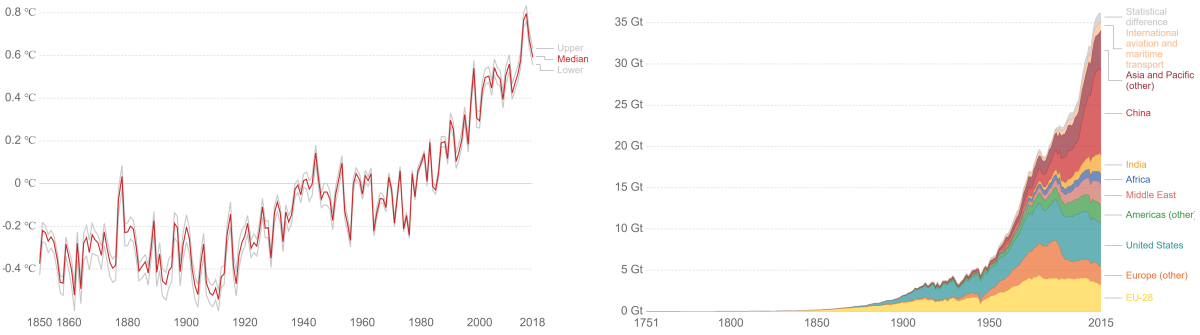

(a) Global average land-sea temperature anomaly relative to the 1961-1990 average temperature in degrees Celsius (°C) [14].

(b) Annual CO_2 emission by world region. The annual CO_2 emissions are measured in billion tonnes (Gt) per year [15].

Figure 1.1: Graphs demonstrating the temperature change (a) and the rise in CO_2 emissions (b) over the last centuries.

Decreasing the CO_2 emissions globally is an ambitious plan, however, considering the growing world population (1% annually) and a staggering rising energy demand, the world is obliged to look for renewable energy technologies [16]. Figure 1.2 demonstrates the consumption of energy worldwide and which energy sources are consumed most. It shows that over 80% of the global energy demand comes from coal, crude oil and natural gas, all emitting CO_2 [1]. Only a small percentage is produced by renewable technologies (*e.g.*, biofuels, solar and wind energy), so a transition of energy is necessary. Even though the research on renewable technologies is accelerating, the current dependency on fossil fuels will remain in the nearby

future, especially in the aviation and tanker sector [17]. Additionally, the renewable power systems still face challenges that have to be overcome, before they can meet the global energy demand.

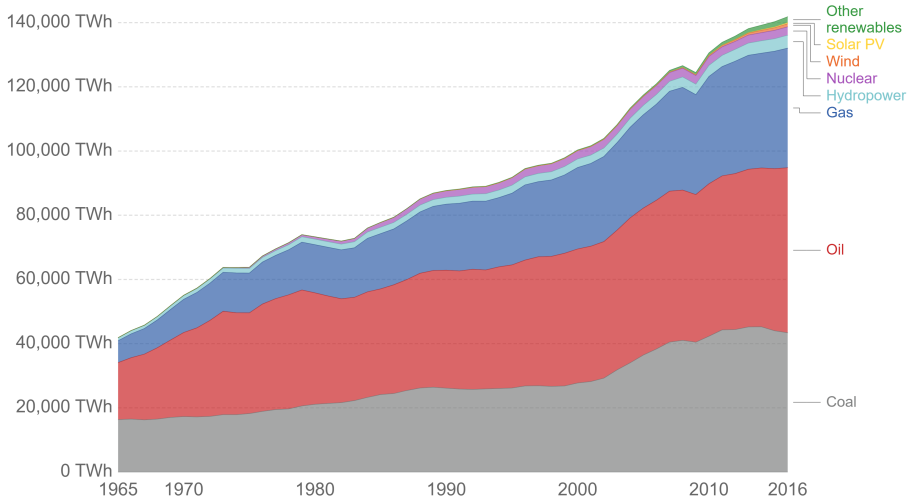

Figure 1.2: Primary energy consumption by source across the world's regions, measured in terawatt-hours (TWh) [1].

A concern with solar and wind energy is that their energy production fluctuates hourly and monthly [18]. These technologies are weather dependent, thus a mismatch occurs between the daily and hourly supply and demand. Therefore, robust technologies are required to store their energy for on-demand use when they ebb [19]. Extensive research is performed on storing any surplus in energy, for instance, in batteries. However, batteries are still expensive and have not been optimized for large scale energy storage yet [20–22]. To decrease the carbon dioxide emissions in the near future, a direct link between renewable energy sources and the fossil fuel demand is favorable. Therefore, a technology is preferable that can bridge the gap for the upcoming decades, consequently enabling our economy to remain carbon based [23, 24].

Electrochemical reduction of CO_2 could be the key to solve the issues regarding the energy transition mentioned previously. CO_2 can be used as a feedstock to create other value added carbon products, such as methanol, ethylene, formic acid and carbon monoxide [19, 23]. Carbon monoxide (CO) is an industrially interesting product, since it can be an intermediate, in the form of syngas (CO with H_2), to produce other high energy hydrocarbon products via the Fisher-Tropsch process [25, 26]. As our global infrastructure is built for the storage and transportation of hydrocarbons, this is an additional advantage for this technology, as no extra changes have to be made to the current situation [19, 27–30]. The emitted CO_2 from the use of these hydrocarbon fuels, can be re-used as a energy source, ideally creating a closed carbon cycle in which the net carbon emissions are 0. Another interesting reduction method is that of water, which can be converted into hydrogen in a similar configuration as that for CO_2 reduction. Hydrogen, just as carbon monoxide, is essential for industry in the form of syngas. Currently, 95% of hydrogen is produced from fossil fuels by steam reforming, emitting tons of carbon dioxide as a byproduct into the atmosphere [31]. Electrochemical reduction (for CO_2 and water) still has some complications, since it cannot yet compete with the cheaper and more energy efficient fossil-based alternatives. Therefore, the selectivity, stability, energy efficiency and current density rate of the configuration should be improved [32, 33].

At the moment, several factors of electrochemical reduction have been extensively researched to optimize the reaction conditions. Most research is conducted to increase performance metrics of parts of the cell. To obtain higher production rates, researchers have focused on changing the electrolyte type and the catalyst type. Therefore, due to the latest breakthroughs, the choice on catalysts and electrolytes differ constantly. An interesting solution for this issue is the use of a bipolar membrane (BPM) in the electrochemical set-up. This type of membrane has the unique ability to pair two different electrolytes which can be optimized for their respective reduction and oxidation reactions [3]. Bipolar membranes have been applied commercially for the production of acid and base (in bipolar membrane electrodialysis), and have only recently been explored for water electrolysis [3, 34–39], photo-electrolysis [40–42] and CO_2 reduction [3, 19, 43]. A BPM consists of a negatively charged cation exchange layer (CEL) and a positively charged anion exchange layer (AEL), therefore no ions should be able to pass through both layers [3, 44]. This results in the dissociation of water

(WDR) at the interface of both membrane layers upon applying an electric field [3]. The water splitting at the BPM interface offers important advantages over conventional monopolar membranes in avoiding polarisation losses in electrochemical water splitting and carbon dioxide reduction [44]. However, the efficiency of the WDR is correlated to co-ion permeation (other ions than H^+/OH^-) through the BPM. The effect of ion characteristics (*e.g.*, ion size and valence) in an electrolyte on ion cross-over have not been studied intensively yet. To further optimise and stabilize a BPM configuration, more research must be performed on the topic.

1.1. Knowledge gaps

Bipolar membranes are a fairly new topic of interest for electrochemical CO_2 reduction and water splitting, where these are namely used in system stabilization applications for electrochemical configurations. However, the mechanism within the BPM has not been studied intensively yet. Vermaas *et al.* did a thorough study on the effect of a pH difference (between the electrolytes) on the BPM voltage [3]. They observed that not only the pH, but also ion cross-over through the membrane influences the electrochemical response of the BPM. Therefore, this research continues on the effects of ion cross-over through the bipolar membrane and how the degree of permeation can be influenced by the characteristics of chosen ions. More research is required on the following points to close the existing knowledge gaps:

- The effect of a pH difference between the electrolytes on the BPM potential.
- The effect of co-ion permeation on the BPM potential and the efficiency of the water dissociation reaction.
- The effect of current density on the BPM potential and the efficiency of the water dissociation reaction.
- The effect of ion cross-over on the pH (and thus the stability) in both electrolytes.

1.2. Problem statement

Through analysing the knowledge gaps of current research, the following main research question has been conducted:

How do ion characteristics influence the ion cross-over through a BPM?

To provide a well constructed answer to the main research question, the following supporting research questions are introduced:

- *How does ion size affect the degree of co-ion permeation?*
- *Does the ion type affect the opposing ion cross-over flux?*
- *How does ion valence influence the degree of co-ion permeation?*
- *What is the relation between ion cross-over and the electrochemical response of the BPM?*

1.3. Outline of thesis

This thesis aims to describe the effect of ion cross-over on the electrochemical response of a BPM. Furthermore, it aims to understand the degree of ion cross-over for different ions. Therefore, the report is structured as follows. First, chapter 2 introduces the theoretical background on electrochemistry and the electrochemical cell. Thereafter, it discusses the BPM and its characteristics, including the water dissociation reaction (WDR), the BPM voltage and ion cross-over. Chapter 3 continues on the experimental set-up used for this thesis. It explains the sequence of experiments and introduces the analytical methods necessary to measure the ion cross-over in samples. Chapter 4 gives the experimental results obtained during this project. These results are discussed and concluded in chapter 5. Finally, chapter 6 gives the recommendations for future research.

2

Theory and background information

This chapter introduces electrochemistry and the electrochemical cell, including its thermodynamics and kinetics, in section 2.2 and 2.3, respectively. The important half reactions that occur in the electrochemical cell, concerning this research, are also discussed in this chapter. Section 2.4 presents ion exchange membranes, including the main subject of this thesis, namely the bipolar membrane (BPM). More specifically, the ion transport through a BPM will be studied. The final subsections (2.4.2-2.4.3) discuss the effect of co-ion permeation on the electrochemical configuration.

2.1. An introduction to electrochemistry

Electrochemistry is the branch of chemistry concerned with the interrelation of electrical and chemical effects [45]. It studies reactions that involve electric charges (and ionic species in a solution) moving between electrodes and through an electrolyte. An electrode is known as an electric conductor and an electrolyte as an ionic conductor.

An electrolytic cell consists of two electrodes and one (or more) electrolytes. Electrodes are typically solid materials that transport charge via the movement of electrons, while electrolytes are solutions (or ionically conductive polymers) containing ionic species for charge transportation [45]. The chemical reactions occur by supplying a charge to the electrodes, which are the cathode and anode. These electrodes transport charge by transporting electrons to and from the reactants. These reactions are called reduction or oxidation (redox) reactions, depending on the flow of electrons. At the cathode, electrons are supplied *to* the reactant, causing a reduction reaction to take place. At the anode, electrons are transported *from* the reactant, causing an oxidation reaction to take place. The basic electrochemical (electron transfer) reaction is given by equation 2.1, where n electrons are transferred in reducing the oxidised species O to the reduced species R [46].

$$O + ne \rightleftharpoons R \tag{2.1}$$

To study these electrochemical redox reaction, an electrochemical cell configuration is often used. Within the electrolytes, two independent half reactions take place, which form the overall chemical reaction of the cell. The important half reactions for this research are discussed in section 2.3. Figure 2.1 shows a simple cell configuration for water electrolysis (overall chemical reaction), that consists of two electrodes, one electrolyte, one ion exchange membrane and a flow of electrons (e^-), which travels from the anode to the cathode. In this thesis, the cathode and catholyte (the electrolyte at the cathode) are always represented in a grey colour, while the anode and anolyte are presented in a red colour.

One is often interested in only one of these half reactions. The electrode at which this reaction occurs is called the working electrode (WE) and the opposing electrode is called the counter electrode (CE). In addition to these electrodes, a reference electrode (RE) is often used to determine the potential of the half reaction at the working electrode. This reference electrode has a fixed potential and is placed close to the working electrode.

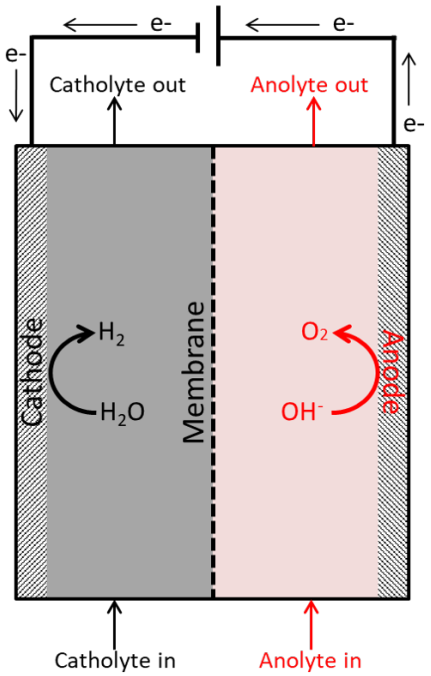

Figure 2.1: Schematic representation of a general cell configuration for electrochemical water electrolysis. H^+ is reduced to H_2 at the cathode and OH^- is oxidized to O_2 at the anode. The catholyte (grey) and the anolyte (red) are separated by an ion exchange membrane. The flow of electrons (e^-) travels from the anode towards the cathode [2].

All half reactions have a thermodynamic potential at which the reaction can occur. These critical potentials are related to the standard potentials, E^0 (V), for the specific chemical substances in the system [45]. Section 2.2 further explains the thermodynamic equations that govern the total cell potential within an electrochemical cell and how the standard potential, E^0, relates to these equations.

2.2. Thermodynamics, cell potential and half reactions

The thermodynamic equations governing the behaviour of an electrochemical configuration are crucial in understanding not only the cell, but also the potential within the system. This section continues on this subject and explains the relevant formulas.

A basic electrochemical reaction requires a total potential (E) to drive the reaction. This potential can be calculated (equation 2.2) by subtracting the theoretical required potential for the reduction reaction (E_{red}) with the theoretical required potential of the oxidation reaction (E_{ox}). The required theoretical potential (E) can also be calculated with the *Nernst equation*, given by equation 2.3. In this equation, E^0 is the standard thermodynamic potential, which can be measured when the concentrations of species O and R, as in equation 2.1, are close to the equilibrium [45]. The standard thermodynamic potentials for the half reactions in this thesis are given in the next section. In equation 2.3, T is temperature, F is the Faraday constant[1] and z is the charge valence [3, 45]. The R in equation 2.3, the gas constant[2], must not be mistaken for species R in equation 2.1. In electrochemistry, when discussing potentials, the standard hydrogen electrode (SHE) can be used as a standard reference. The SHE is a redox electrode which forms the basis of the thermodynamic scale of oxidation-reduction potentials, since it has a standard electrode potential (E^0) of 0 V at 298 K (1 bar, 1 M H^+) [47]. The potential in the Nernst equation correlates to the concentrations of the oxidation and reduction species. These species can be H^+ and/or OH^-, and in that case the potential is pH dependent. This pH dependency is further discussed in subsection 2.2.1.

[1] The Faraday constant is equal to 96485 $C \cdot mol^{-1}$.
[2] The gas constant R is equal to 8.314 $J \cdot K^{-1}$ mol^{-1}.

$$E = E_{red} - E_{ox} \tag{2.2}$$

$$E = E^0 + \frac{RT}{zF} \ln \frac{C_O}{C_R} \tag{2.3}$$

Having determined that every half reaction has a thermodynamically defined E^0, one can theoretically calculate the total potential required to trigger a reaction. However, to drive a reaction at a certain rate an additional overpotential is needed besides the thermodynamic requirement. The kinetic aspects behind this overpotential are discussed in more detail in section 2.3. The following subsection discusses the important half reactions within this research and their reaction pathways.

2.2.1. Half reactions: HER, CO2RR and OER

A goal of this project is to understand and optimize the performance of a bipolar membrane in an electrochemical cell for water electrolysis and/or CO_2 electrolysis. Hence, the hydrogen evolution reaction (HER) and the CO_2 reduction reaction (CO2RR) are the two half reactions, both occurring at the cathode, that are first introduced in this subsection. Additionally, the oxygen evolution reaction (OER) is discussed, since this is the counter reaction at the anode for both the HER and CO2RR.

The electrochemical configuration used in this research is applicable for both water reduction (HER and OER) and CO_2 reduction (CO2RR and OER) [3, 39, 44]. However, only water reduction is performed (the reasoning behind this can be found in chapter 3). The hydrogen evolution reaction has a thermodynamic redox potential (E^0) close to that of CO2RR, 0.00 V vs. RHE[3] and -0.11 V vs. RHE, respectively, as is given in table 2.1. Thus, the HER is competitive with CO_2 reduction [19, 27]. This means that in CO_2 reduction set-ups, the HER occurs as an undesired reaction. There are two situations in which hydrogen evolution can occur, under acidic conditions (equation 2.4) and in neutral/alkaline conditions (equation 2.5). The CO2RR reacts differently in acidic (equation 2.6) and neutral/alkaline environments (equation 2.7) as well, which is also the case for the oxygen evolution reaction, given in equation 2.8 (neutral/acidic) and in equation 2.9 (alkaline).

$$2H^+ + 2e^- \rightleftharpoons H_2 \tag{2.4}$$

$$2H_2O + 2e^- \rightleftharpoons H_2 + 2OH^- \tag{2.5}$$

$$CO_2 + 2H^+ + 2e^- \rightleftharpoons CO + H_2O \tag{2.6}$$

$$CO_2 + H_2O + 2e^- \rightleftharpoons CO + 2OH^- \tag{2.7}$$

$$H_2O \rightleftharpoons \frac{1}{2}O_2 + 2H^+ + 2e^- \tag{2.8}$$

$$2OH^- \rightleftharpoons \frac{1}{2}O_2 + H_2O + 2e^- \tag{2.9}$$

The oxygen evolution reaction (OER) requires a high potential (1.23 V vs. RHE, table 2.1), since H_2O molecules have a high stability. It has been observed that OER operates with high efficiency in alkaline conditions, due to stable behaviour of earth-abundant catalysts (commonly used for OER) [3, 48].

Research has proven that electrocatalysts for HER show the lowest overpotentials in acidic media, thus an acidic catholyte is preferred for HER [3]. HER is a more straightforward reaction, compared to CO2RR, since CO_2 reduction utilizes a variety of intermediates which require stabilization. Both HER and CO2RR consume protons, thus the potential at the cathode is pH dependent, as given by the Nernst equation (2.3). This equation can be rearranged (in multiple steps) to equation 2.2.1, which shows a potential shift caused by a change in pH. The pH is the logarithm of the concentration of H^+, as given in equation 2.2.1. Thus, when protons are consumed, it increases the pH and the potential of the half reaction decreases.

[3] Potentials documented versus RHE (reversible hydrogen electrode) are potentials corrected for pH. This results in a pH independent potential.

Table 2.1: Thermodynamic potentials of oxidation and reduction reactions. The bottom section gives the total cell potential when both half reactions occur. The potentials are documented vs. RHE, a pH independent potential.

Half reaction	**Thermodynamic potential E^0 (V vs. RHE)**
HER	0.00
CO2RR	-0.11
OER	1.23
Total reaction	**Thermodynamic potential E^0 (V vs. RHE)**
HER - OER	-1.23
CO2RR - OER	-1.34

$$E = E_0 + \frac{RT}{zF} \times \ln[\mathrm{H}^+]^{-2} \tag{2.10}$$

$$E = E_0 + \frac{8.314 \times 298}{2 \times 96485} \times -2 \times 2.303 \times \log[\mathrm{H}^+] \tag{2.11}$$

$$E = E_0 - 0.0591 \times \mathrm{pH} \tag{2.12}$$

Carbon dioxide can be reduced to a variety of products (not only CO, as in equations 2.6 and 2.7) depending on catalyst material, applied potential, morphology and reactant concentrations [23, 49, 50]. However, CO is the smallest product (as a molecule) and this route is both straightforward and well understood, making this pathway interesting for process optimization. Moreover the route to CO (and formic acid) is potentially economical viable due to the low cost per electron (e^-) ratio [51]. Nonetheless, the electrochemical reaction to CO and other chemicals has not yet been commercialized, due to a poor thermodynamic efficiency (high overpotential), a low current density efficiency, a low selectivity, slow kinetics and a poor stability [52]. However, research performed in 2011, proved that the combination of two catalysts could eliminate the high overpotential [53]. Additionally, multiple studies demonstrated that electrochemical CO_2 reduction has prospective when using a gas-diffusion electrode (promoting the reaction rate of reactants to products) [54–56]. This gas-diffusion electrode has not been used in this research, since CO_2 reduction is not the main concern of this thesis. The focus of this report is on an electrochemical configuration with a bipolar membrane, which is suitable for electrochemical reactions, including CO_2 reduction.

2.3. Kinetics: overpotential, reaction rate, and ion transport

The previous section mentions that the total potential for a (half) reaction is related to the standard thermodynamic potential, E^0, and can be influenced by the concentrations of reactive species (including H^+ and OH^-, which influence the pH). However, when a reaction is performed at a certain rate, one increases the potential beyond the thermodynamic requirements of this reaction. This additional potential is called the overpotential η.

$$\eta = E - E_{eq} \tag{2.13}$$

Equation 2.13 demonstrates the extent of polarization (measured by the overpotential) between the equilibrium value of the electrode potential (E_{eq}) and the actual potential (E). Within a total cell reaction, every step is driven by a certain overpotential. This is because every step has a certain resistance, which, when composed in a series of resistances, forms the total resistance R (Ω). A part of this resistance is the ohmic drop caused by current flow in the solution iR_s, with i (A) as the current.

$$E = E_{eq} + \eta - iR_s \tag{2.14}$$

In this research the potential over a bipolar membrane (BPM) is measured, thus it is important to compensate for the ohmic drop between the reference electrode (RE) and the sense electrode (SE)[4]. The distance from the tip of the RE to the tip of the SE, is in fact a fraction of iR_s, called iR_u, which is the uncompensated resistance. iR_u can be calculated from experimental data or can be found in theoretical data. The conductivity (L), can be calculated by multiplying the specific conductivity from a solution (κ) with the surface area (A), and then dividing it with the distance between the electrode and reference electrode (l), as shown in equation 2.15. The conductance, L, is given in units of siemens ($S = \Omega^{-1}$), making it inversely proportional to the resistance [45]. For this research all experiments have been corrected for conductivity (ohmic losses), which is further discussed in chapter 3.

$$L = \frac{\kappa A}{l} \tag{2.15}$$

When a current (i) is applied, electrons travel via an electric conductor from the anode to the cathode. In this thesis, electrons travel from the anode to the cathode, since the reduction reaction takes place at the cathode and the oxidation reaction takes place at the anode. The total amount of electrons transferred after an amount of time can be measured as the charge, Q, which is expressed in units of coulombs (C), where 1 C is equivalent to 6.24×10^{18} electrons [45]. The relationship between the measured charge and the amount of formed product for faradaic processes, is given by *Faraday's law* (equation 2.16). This equation demonstrates the direct proportionality between the Faradaic current and the electrolysis rate. In equation 2.16, N is the number of electrolyzed moles, n is the number of electrons consumed in the electrode reaction (*e.g.*, 2 for the reduction of $2\,H^+$ in HER)[5] and F is Faraday's constant.

$$Rate\left(mol/s\right) = \frac{dN}{dt} = \frac{i}{nF} \tag{2.16}$$

The Faraday constant represents the amount of coulombs equivalent to 1 mol of reaction (*i.e.*, consumption of 1 mole of reactant or production of 1 mole of product in a one-electron reaction). The current, i, is the rate of coulombs (or transferred electrons), where a current of 1 ampere (A) is equivalent to 1 C/s. The current is also related to the total potential (E) and total resistance (R) in the electrochemical cell ($i = E/R$). Plotting the current versus potential (i-E or I-V), results in a curve that provides information about the nature of the solution and the electrodes, including the reactions that occur at the interfaces [45]. Since the electrode-electrolyte interface is a heterogeneous reaction medium, the mass transfer rate from the electrode to the electrolyte depends on various surface effects, which is why equation 2.16 is usually described in units of mol/s per unit area, where j is the current density (A/cm^2) and A is the reaction surface area (cm^2).

$$Rate\left(\mathrm{mol\,s^{-1}\,cm^{-2}}\right) = \frac{i}{nFA} = \frac{j}{nF} \tag{2.17}$$

The electrode reaction rate (current) is governed by the rates of processes such as mass transfer (subsection 2.3.1), electron transfer at the electrode surface, chemical reactions (subsection 2.2.1) and other surface reactions (*e.g.*, adsorption and desorption). Note that adsorption/desorption (non-faradaic processes)[6] can occur when no charge crosses the interface, which changes the potential, electrode area and solution composition [45]. The electrode potential strongly affects the kinetics of reactions occurring on the electrode surface [45]. For a one-electron reaction (equation 2.18) this effect is described with the forward and backward rate constants, k_f and k_b, respectively.

$$O + e \underset{k_b}{\overset{k_f}{\rightleftharpoons}} R \tag{2.18}$$

[4] Normally, the potential of the working electrode (WE) is measured by placing a RE close to the WE. However, for this research the BPM voltage is measured, which is why an extra RE is placed in the anolyte on the other side of the membrane. This is the sense electrode (SE).

[5] The hydrogen evolution reaction, $2H^+ + 2e^- \rightarrow H_2$, consumes two mol electrons for the production of one mol H_2.

[6] Faradaic processes include charge transfer across the electrode-electrolyte interface. They are governed by Faraday's law. Nonfaradaic processes can change the solution composition and potential without any charge transfer.

To describe the effect of the potential on the kinetics of reactions can be quite a challenge. Fortunately, there is an approach named the Butler-Volmer model which describes this phenomenon. In equations 2.19-2.21, $f = F/RT$ and α is the transfer coefficient, which can range from zero to unity. k^0 is the standard rate constant. The complete derivation of equation 2.21, known as the current-potential characteristic, can be found in literature [45].

$$k_f = k^0 exp[-\alpha f(E - E^0)] \tag{2.19}$$

$$k_b = k^0 exp[(1-\alpha) f(E - E^0)] \tag{2.20}$$

$$i = FAk^0[C_O(0,t)e^{-\alpha f(E-E^0)} - C_R(0,t)e^{(1-\alpha)f(E-E^0)}] \tag{2.21}$$

Often, equation 2.21 is readjusted to the *current-overpotential* equation (2.22). This equation, has the advantage of working with i_0 rather than k_0, which describes the current in terms of deviation from the equilibrium potential, that is the overpotential (η), rather than the standard thermodynamic potential (E^0) [45]. Note that the first term in equation 2.22, is the cathodic component current at any potential, and the second term gives the anodic contribution [57].

$$i = i_0 \left[\frac{C_O(0,t)}{C_O^*} e^{-\alpha f \eta} - \frac{C_R(0,t)}{C_R^*} e^{(1-\alpha) f \eta} \right] \tag{2.22}$$

2.3.1. Ionic transport: diffusion, migration and convection

Mass transfer of ions in the electrolyte occurs by diffusion, migration and convection. Diffusion and migration result from a gradient in the electrochemical potential $\bar{\mu}$. Convection results from an imbalance of forces on the solution [45]. When these accumulated forces form a gradient, a flux of species (J_j) occurs. This can be described by the *Nernst-Planck equation* (2.23), with a diffusion term ($D_j \nabla C_j$), a migration term ($((z_j F)/(RT)) D_j C_j \nabla \phi$) and a convection term ($C_j v$). D_j is the diffusion coefficient of species j, C_j is the concentration of species j and v is the velocity of the solution.

$$J_j = -D_j \nabla C_j - \frac{z_j F}{RT} D_j C_j \nabla \phi + C_j v \tag{2.23}$$

When the velocity is equal to zero, due to quiescent conditions (no stirring or no density gradient), the equation can be simplified to equation 2.24. This equation represents only the contribution of diffusion and migration to the total flux. The total current in a solution at any location during electrolysis is made up of all these contributions. Since the ions are the charge carriers in the electrolyte, their movements influence the total current.

$$J_j = -D_j \nabla C_j - \frac{z_j F}{RT} D_j C_j \nabla \phi \tag{2.24}$$

For instance, in the bulk solution, concentration gradients are generally small. This means that most of the current is carried by the migration of ions. The mobility of these ionic species (u_j) is defined in the *Einstein-Smoluchowski equation* (2.25) [45]. The diffusion coefficient (D_j) can be rewritten (as equation 2.26) and rearranged (to equation 2.27) to obtain the radius of an ion in a solvent (R_H). k_b is the Boltzmann constant, η is the viscosity of the solution and α is the radius of a perfect sphere. This radius, called the *Stokes radius*, describes the radius of a hard sphere that diffuses at the same rate as the solute. For this research the Stokes radius is an interesting parameter, since it does not only factor in the size of an ion, but also the solvent effects. A small ion can have a large stokes radius, therefore it can be less mobile than a in comparison larger ion.

$$u_j = \frac{|z_j| F D_j}{RT} \tag{2.25}$$

$$D_j = \frac{k_B T}{6\pi\eta\alpha} \tag{2.26}$$

$$R_S = \alpha = \frac{k_B T}{6\pi\eta D_j} \tag{2.27}$$

2.4. Ion exchange membranes

This section introduces an ion exchange membrane, an important segment in an electrochemical configuration. Typically, ion exchange membranes are placed between the catholyte and the anolyte to facilitate the transportation of ions and prevent complete mixing of the electrolytes [58]. The selection of an ion exchange membrane is of great importance, because if the most applicable membrane is chosen, it allows ion transport favoring the desired reaction. Additionally, an ion exchange membrane can potentially balance (with ion cross-over) the formed ions on both sides of the electrochemical cell, resulting in a stable configuration. There are a few different types of ion exchange membranes and this section discusses the relevant ones. Next, the bipolar membrane (the main subject of this thesis) is introduced and its advantages and characteristics are described.

A membrane is used to separate two phases from each other while restricting the transport of specific ions from one side to another. When an electrical field is applied in an electrochemical cell, positively charged ions want to move from the anode (+) to the cathode (-), whereas negatively charged ions want to move from the cathode (-) to the anode (+) [45]. However, an ion exchange membrane has a selectivity towards specific chemical species, thus limiting the transport for other ions [59]. These specific chemical species (that can travel through the membrane) vary per type of membrane and are primarily determined by the molecular size and valence of the species [59]. The rate of transport within a membrane is caused by a driving force, which is commonly a concentration, pressure or potential gradient across the membrane [59]. Therefore, the most common transport mechanisms through a membrane in an electrochemical cell are diffusion and migration, driven by a concentration- or potential gradient, respectively (as given in section 2.3.1) [45, 60]. The potential gradient within a membrane (due to concentration differences between charged ions) affects the selectivity of a membrane, which is called the permselectivity. This selectivity is described by the Donnan equilibrium, and is further described in section 2.4.2 [61]. An ion exchange membrane is not only ion conductive, it is also hydrophilic, allowing the transport of water across the membrane [62].

Anion exchange membrane (AEM): a semipermeable membrane designed to conduct anions (*e.g.*, OH^-). The fixed charge group within an AEM is positive, thus allowing negatively charged ions to cross-over [62–64]. The electric field applied to the system ensures that anions flow from the cathode to the anode (+), while cations travel from the anode to the cathode (-). However, an AEM partially blocks the cations that want to travel towards the cathode (as is shown in subfigure 2.2a). This is unfavorable for the HER, were H^+ ions at the cathode form hydrogen. Contrary, for CO2RR this is favorable, since the HER is an undesired competing reaction. When cations are blocked, while anions travel freely from the cathode to the anode, the cations can flow against the electric field as co-ions, to balance the charge in the system. This however, differs depending on the pH and concentration of the electrolyte. In an alkaline environment, the OH^- ions are the most abundant and therefore the main transported ions. In acidic conditions, the H^+ ions are abundant, and H^+ co-ion cross-over takes place to balance the charge within the system [45, 60]. When utilizing an AEM for CO2RR, side reactions occur rapidly at the cathode and the side products buildup in the catholyte, inhibiting the membrane transport of ions and reducing the efficiency of CO2RR [65–67].

Cation exchange membrane (CEM): an ion exchange membrane, as the name suggests, favoring the transport of cations (*e.g.* H^+) to the cathode (-), since the fixed charge group in the CEM is negative [62–64]. In a CEM, the anions that want to migrate from the cathode to the anode are unable to cross the membrane, as demonstrated in subfigure 2.2b. When the electrolytes are highly alkaline (low concentration H^+), for instance KOH, K^+ becomes the main charge carrier. To balance the system, K^+ ions may cross the CEM to the anolyte (countering the electric field), bringing along OH^- ions to balance the charge [68, 69]. However, in alkaline environments, the main charge carriers are the anions. Thus, when using a CEM, the transport of these ions is blocked, forcing the cations (K^+) towards the cathode. This can cause high polarization losses [70].

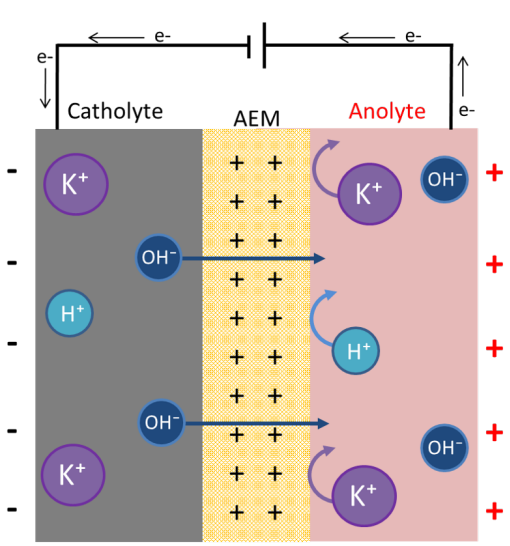

(a) An electrochemical cell with an anion exchange membrane. The catholyte (grey) and the anolyte (red) are both a KOH solution, but only anions can travel through the positively charged AEM. The anions travel from the cathode (-) to the anode (+).

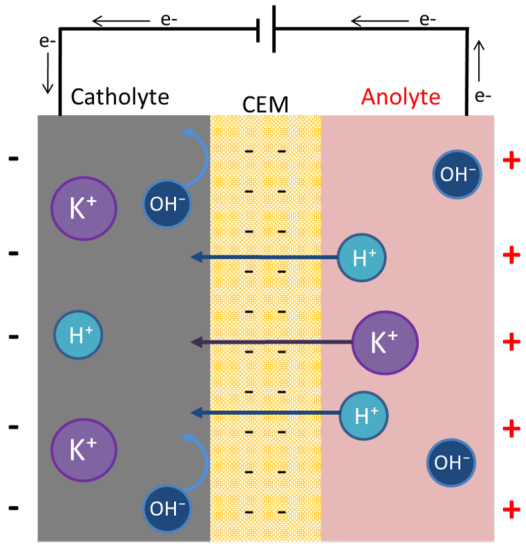

(b) An electrochemical cell with a cation exchange membrane. The catholyte (grey) and the anolyte (red) are both a KOH solution, but only cations can travel through the negatively charged CEM. The cations travel from the anode (+) to the cathode (-).

Figure 2.2: Schematic representations of electrochemical configurations with an AEM (a) and a CEM (b) [2].

2.4.1. Bipolar membrane

This subsection introduces the main subject of this research, the **bipolar membrane (BPM)**. It consists of a negatively charged cation exchange layer (CEL) and a positively charged anion exchange layer (AEL), selective for the transport of only cations or anions, respectively [3, 44, 71, 72]. The BPM is actually a combination of an AEM and a CEM. A schematic representation of a BPM in an electrochemical cell, is given in figure 2.3.

The previous section describes the monopolar membranes and their ion cross-over limitations, such as the buildup of ions that inhibit the membrane and cause high polarization losses [65–67, 70]. Furthermore, it can be convenient to use two electrolytes with different pH values for the catholyte and anolyte. In water electrolysis, the HER has lower overpotentials in acidic environments and the OER operates at high efficiency in alkaline conditions [3, 44, 48, 73]. If a monopolar membrane is utilized for such a configuration, the pH values in both electrolytes will not remain stable, since cations (H^+) or anions (OH^-) travel from one electrolyte to the other (depending on the chosen ion exchange membrane), thus depleting the pH difference between the electrolytes.

A BPM can overcome these constraints, since ideally, both cations and anions cannot travel through the membrane, for the cations are repelled by the anion exchange layer and the anions are repelled by the cation exchange layer [3, 39, 71, 72]. The preferred direction of migration, due to the electrical field have no effect in a BPM, since ions cannot cross over through the BPM. As an effect, the dissociation of water (WDR) into H^+ and OH^- occurs at the interface layer (IL) between the AEL and CEL [3, 71]. The H^+ moves to the cathode and the OH^- travels to the anode, following the direction of the electrical field [34, 36, 37, 71]. The water dissociation reaction is more thoroughly described in the next subsection. Ideally, the pH in both compartments of the electrochemical cell maintains stable, due to the WDR and limited co-ion permeation [43]. This allows the selection of electrolytes with different pH values, which can be more suitable for each half reactions in the electrochemical set-up. Additionally, reduced contamination and improved stability can lower the total cell potential, thus decreasing the costs (especially because more suitable, possibly cheaper catalysts can be selected) [19].

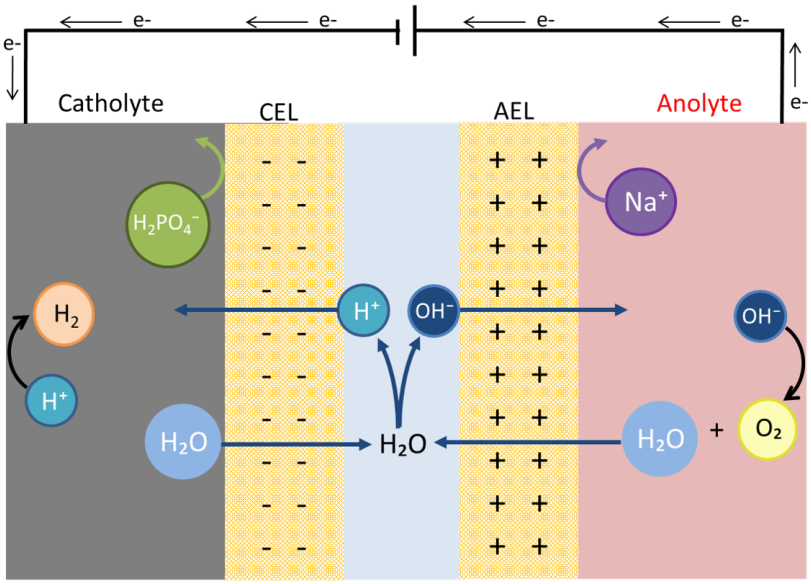

(a) Schematic representation of a BPM with the WDR at the interface layer. The catholyte is an acidic phosphate buffer, thus the HER consumes H^+ and produces hydrogen. The consumed H^+ are replaced by the WDR. The OER in the anolyte (alkaline conditions) consumes OH^- and produces water and oxygen. The consumed OH^- is replaced by water splitting. The pH remains constant on both sides.

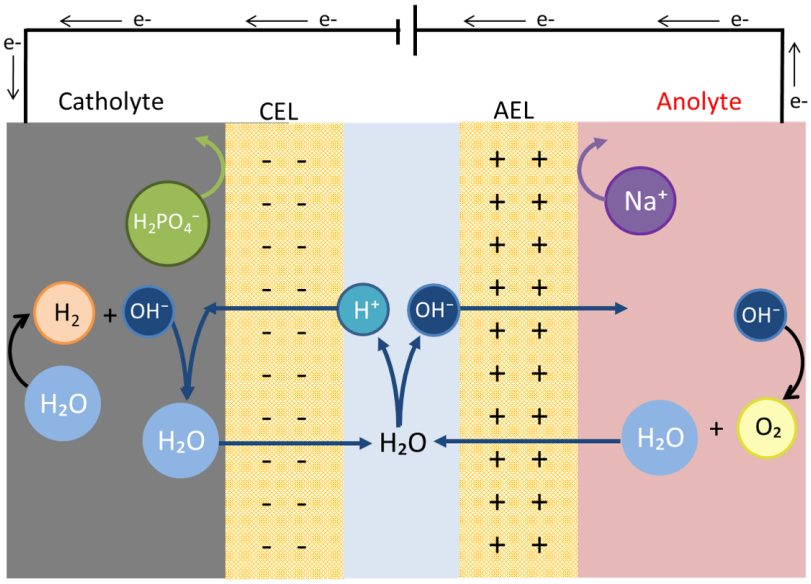

(b) Schematic representation of a BPM with the WDR at the interface layer. The catholyte is a neutral phosphate buffer, thus the HER consumes water and produces hydrogen and OH^-. The consumed water is replaced by the WDR, since the splitted H^+ forms water with the OH^-. The OER in the anolyte (alkaline conditions) consumes OH^- and produces water and oxygen. The consumed OH^- is replaced by water splitting. The pH remains constant on both sides.

Figure 2.3: Schematic representations of an electrochemical configuration with a bipolar membrane (BPM) placed between the catholyte (grey) and anolyte (red) [2]. The BPM consists of a cation exchange layer (CEL) and an anion exchange layer (AEL). Water dissociation (WDR) occurs at the interface layer and H^+ is transported to the catholyte, while OH^- is transported to the anolyte. At the cathode, the HER occurs in acidic conditions (a) or neutral/alkaline conditions (b) and at the anode the OER takes place.

2.4.2. Water dissociation (WDR) and potential change at BPM interface layer

As stated in the previous section, the BPM consists of a cation exchange layer and an anion exchange layer, hence in theory no salt ions should be able to pass through both layers [3]. This results in dissociation of water, as given in equation 2.28, at the interface layer. Upon applying an electric field, the WDR maintains an equal ionic transport through the entire electrochemical cell.

$$H_2O \rightleftharpoons H^+ + OH^- \tag{2.28}$$

When, for instance, hydrogen evolution occurs at an applied potential, protons are consumed in the catholyte, as demonstrated in subfigure 2.3a. Water is then dissociated to supply a hydrogen proton to the catholyte and a hydroxide ion to the anolyte. The hydroxide ion replaces the consumed OH^- for the oxygen evolution reaction at the anode. Ideally, this water dissociation occurs at the same rate as the consumption of protons/anions, hence, conserving the different pH values on either side of the membrane [3]. The reaction pathway for conserving the pH can differ in the anolyte/catholyte depending on the pH, as shown in figure 2.3. However, the water dissociation reaction remains unchanged.

As previously stated, a BPM allows separation of acidic and alkaline solutions in the cathode and anode compartments, respectively. Therefore, it provides optimal pH conditions for HER and OER catalysts [44, 48, 73]. At an extreme pH difference (*i.e.*, a catholyte at approximately pH 0 versus an anolyte at approximately pH 14), the process is well understood. For this scenario, a potential of 0.83 V must be applied to trigger the water dissociation reaction in the BPM [3]. This 0.83 V is actually the thermodynamic potential difference to separate H_2O into 1M H^+ and 1M OH^- [4, 35, 71, 74, 75]. However, when using non extreme pH values (other than 0-14) the effect on the water dissociation in the BPM is not as clear. Non extreme pH values means lower concentrations (<1 M) of H^+ and OH^-, which causes a sudden jump in concentration at the membrane-electrolyte interface [3]. It is assumed that the concentrations in the AEL and CEL are around 1M H^+/OH^-, since the cations and anions balance the immobile charges in the BPM layers. This explains the concentration difference at the membrane-electrolyte interface when not using extreme pH values (*i.e.*, < 1M). As a consequence, a Donnan potential[7] arises at the membrane-electrolyte interfaces [3]. Figure 2.4 shows how the concentration gradient of H^+ influences the potential in the catholyte-CEL interface, CEL-AEL interface and AEL-anolyte interface. The (thermodynamic) voltage over the BPM, ϕ_{BPM}, must be equal to equation 2.29, which is similar to the rearranged Nernst equation for potential change against pH difference (equation 2.2.1 in section 2.2).

$$\phi_{BPM} = \Delta\phi_1 + \Delta\phi_2 + \Delta\phi_3 = \frac{RT}{zF}\ln\left(\frac{[H_{an}{}^+]}{[H_{cat}{}^+]}\right) = \frac{RT}{zF}\frac{1}{\log(e)}(pH_{an} - pH_{cat}) = 0.0591\Delta pH \tag{2.29}$$

However, research has proven that this ideal scenario does not always hold true. Vermaas *et al.* performed a detailed analysis of voltage-current relations for a BPM under different pH values, concentrations and flow rates [3]. Furthermore, it demonstrated that co-ions (ion in the electrolytes other than H^+ and OH^-) do pass through the BPM. This *co-ion permeation* influences the BPM voltage, especially at low current density rates when diffusion plays a rather large role. The next subsection continues on co-ion permeation.

2.4.3. Ion cross-over through the BPM

An ideal bipolar membrane dissociates the same amount of water molecules as the amount of consumed H^+ and OH^- in the catholyte and anolyte. However, membranes are never perfectly selective, meaning that a small fraction of other ions (co-ions) that are present in the electrolytes passes through the BPM [3]. When these ions cross over they influence the system's voltage and the rate of the water dissociation at the BPM interface, since the current is carried by these co-ions.

Figure 2.5 demonstrates how different ions are affected by diffusion and migration. In an open circuit (current density is 0 mA/cm^2) migration does not play a role, since there is no electric field applied on the system. Still, ion cross-over is observed and can only be related to diffusion. There is a large concentration

[7] A Donnan potential is a potential difference that arises from an equilibrium balance of selective charge exchange across an interface [45].

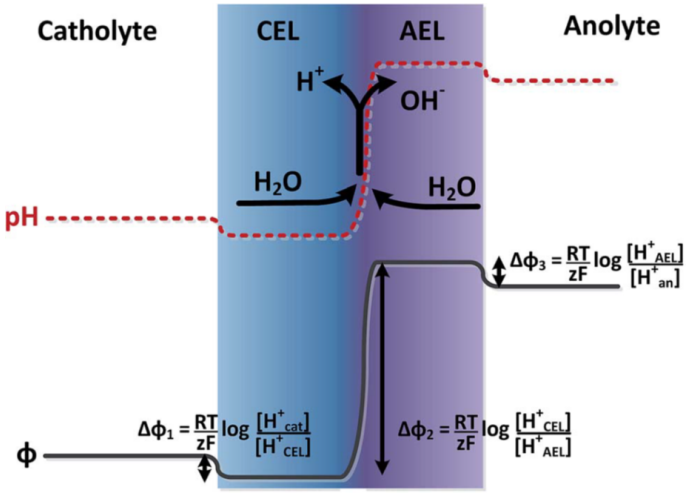

Figure 2.4: Potential (ϕ) and pH gradients over a cross-section of a BPM, consisting of a cation exchange layer (CEL) and an anion exchange layer (AEL). The Donnan potentials at the interfaces arise from sudden H^+ concentrations changes. From source: [3].

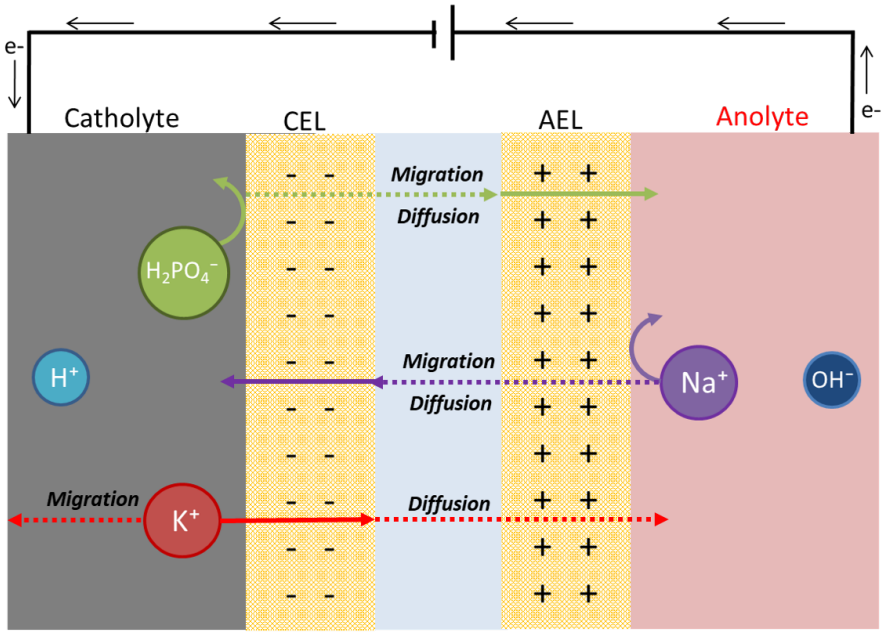

Figure 2.5: Schematic representation of electrochemical cell with the BPM between the catholyte and the anolyte. The catholyte is a phosphate buffer and the anolyte is a NaOH solution. The figure shows how different ions (*e.g.*, charge, location in set-up) are influenced by diffusion and migration forces. At low current densities, diffusion is important, while at high current densities, migration has a larger impact [2, 3].

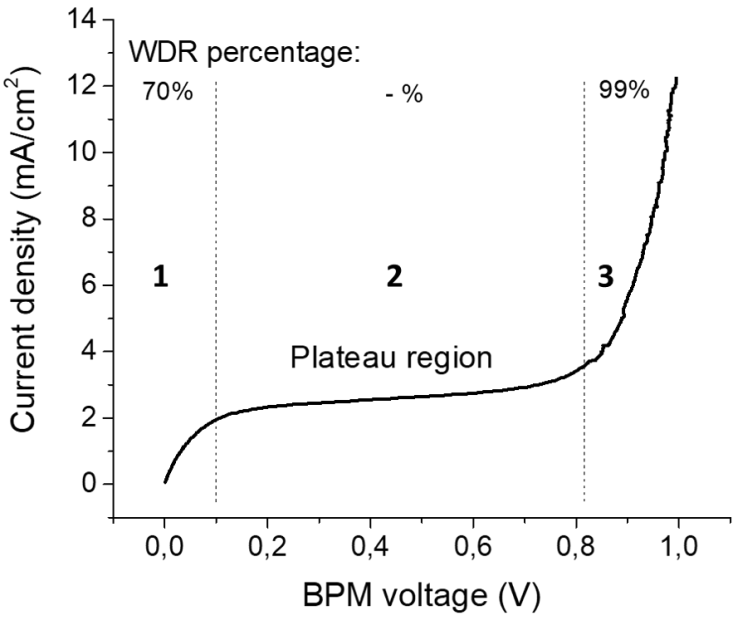

Figure 2.6: Characterization of the BPM *I-V* curve in 3 regimes. Regime 1 shows a low BPM potential for low current densities, due to relatively high co-ion cross-over and <%70 charge carried by WDR. Regime 2 demonstrates the plateau current density, where BPM potential sharply increases for higher current densities. Regime 3 exhibits an exponential increase in current density (carried charge >99% WDR) at 0.8 V, the thermodynamic requirement for WDR. From source: [4].

gradient for species in the system. The catholyte in figure 2.5, for instance, contains a phosphate buffer. The concentration of phosphate ions ($H_2PO_4^-$) in the anolyte is practically zero, therefore some phosphate ions, due to a large concentration gradient, can diffuse into the anolyte through the negative (repelling) CEL [45]. When the current density is increased, this diffusion flux remains. However, the electric field also forces the negatively charged phosphate ions towards the anode (+). Now both diffusion and migration contribute to the flux and more phosphate ions cross over into the anolyte. At high current densities it is known that the water dissociation reaction fluxes (H^+ to the cathode and OH^- to the anode) dominate the mass transport within the BPM [3, 4, 71]. These migration fluxes force co-ions out of the cation exchange and anion exchange layer, thus lowering co-ion permeation [3]. In the anolyte co-ions (*e.g.*, Na^+ in figure 2.5) undergo the same forces, except in the opposite direction from the anolyte towards the cathode. Some co-ions (such as K^+ in the catholyte) are first drawn towards the anolyte (due to a concentration gradient) at low current densities, while at high current densities they migrate towards the cathode, as can be seen in figure 2.5. In this case, negligible cross-over exists at high current densities.

Co-ion cross-over influences the WDR efficiency, since every co-ion carries a charge that balances the imbalance created by the HER and the OER in the catholyte and anolyte, respectively [19, 44, 72]. Ideally this imbalance is restored by the H^+ and OH^- from the water dissociation, but when a co-ion crosses over, the balance is restored and water is not split. In the early research regarding bipolar membranes, it was hypothesized that at low current densities all charge is carried by co-ions, *i.e.*, that no water dissociation occurs below a certain limiting current density [3, 4, 71, 74, 76]. This appears to be the case for monopolar membranes, yet a BPM reveals a different behaviour at low current densities. Figure 2.6 displays that the *I-V* curve of the BPM can be segregated in three regimes:

(1) At low current densities the membrane potential is close to or lower than the thermodynamic potential for water dissociation, which is why relatively more charge is carried by co-ions. Research has indicated that for some electrolytes in a BPM configuration at low current densities, up to 10% – 30% of the charge is carried by ion cross-over, as is demonstrated in figure 2.6 [38, 40]. This co-ion permeation decreases the BPM potential even further, since a larger potential is required for the WDR than for co-ion cross-over [3, 71].

(2) In the second regime a plateau is observed with a sharp increase of voltage when the current density increases. The origin of this plateau is not the result of solely monopolar membrane or bipolar membrane polarization, on account of water dissociation being the main charge carrier in regime 1 [4, 77, 78]. Therefore, the plateau is defined as a *plateau current density* and not the term 'limiting current density' [3].

(3) Finally, the third regime exhibits an exponential increase in current density close to 0.8 V, as is described in the Butler Volmer equation 2.21 for an electron transfer reaction of WDR. This value resembles the water dissociation potential at extreme pH difference ($14 \times 0.0591 = 0.8274$ V). At this potential nearly all the charge is carried by the WDR (> 99%), although ion cross-over still exists. The relative contribution of ion cross-over is merely smaller [38].

It is important to mention that not all these regimes are present in every BPM *I-V* curve. It depends on the pH difference, the electrolyte concentration and the ionic radius for the plateau current density to be visible. However, regime 3 is observed for all curves at high current densities. The *I-V* curves for different ΔpH obtained by Vermaas *et al.* can be consulted in appendix A [3]. The three regimes that have been discussed can actually be followed by a fourth regime, which is when the BPM potential starts to further increase rapidly at high current densities (after regime 3). The water dissociates at such a high rate, that the water from the electrolytes cannot be transported at sufficient diffusion rate to the interface layer due to diffusion limitations. This increases the resistance in the membrane and elevates the BPM potential. It is known, that the electrolyte concentration increases the height of the plateau in regime 2 and that the flow rate on the other hand has a slight effect on the height of the plateau [3]. Thus, there is a relationship between the observed plateau and the diffusion boundary layer. However, observing that the plateau current density in regime 2 cannot be explained from a diffusion boundary aspect only (due to current density limitations), it is presumed that the plateau is caused by the ion permeation contribution [3]. The effect of ion cross-over on the electrochemical response of a BPM is known, however, the effect of ion type (mobility, ion size and pK_a[8] on co-ion permeation requires further research [3, 19]. This thesis aims to understand this effect and therefore different electrolytes will be tested in an electrochemical configuration with a BPM.

[8]The pK_a is the logarithmic constant of the k_a, the acid dissociation constant, which is a quantitative measure of the strength of an acid in solution. During this research different electrolytes with different pK_a values are tested. Chapter 3 discusses the relationship between pH and pK_a.

3

Method and design for experimental set-up of the electrochemical cell

This chapter addresses the experimental set-up and method of this research. First, it discusses the main approach for this thesis. Second, the experimental set-up and equipment are given, after which the used chemicals and solutions are introduced. Third, the experimental method is described in detail. The chapter ends with a short explanation of the analytical methods used to analyze the experimental samples.

3.1. Approach

The main objective of this thesis is to study the parameters that affect ion cross-over through a bipolar membrane (BPM) in an electrochemical configuration. The production of hydrogen, through the reduction of water, is not the main concern. Thus, hydrogen is not measured during the experiments and the selectivity or activity towards products is not analyzed.

Therefore, to simplify the set-up, a flow-cell structure (with two electrolytes separated by a BPM) is chosen. The conventional way to perform electroanalytic research is by utilizing a H-cell[1]. However, recent studies have indicated that the flow-cell has major benefits compared to the conventional H-cell, especially when high current densities are applied, as in the experiments reported in this thesis [28, 51, 80, 81]. Section 3.2 discusses the specific flow-cells used in this research.

To observe the effect of co-ion permeation, different electrolyte solutions are used in the catholyte, while operating with the same anolyte (0.5M NaOH) for all experiments. This guarantees that the differences observed are caused by the interaction with the catholyte. The catholyte solutions differ in chemical contents (*e.g.*, ion type and ion radius) and in pH (and pK_a) values, but do not differ in concentration (0.5M). The pH of the bulk is measured *in situ* to ensure that the system is stable. Slight pH changes can be related theoretically to ion cross-over and to the concentration ratio (A^-/HA), as given in equation 3.3 in subsection 3.3.1. The flow rate (0.07 $cm^3\,s^{-1}$) remains constant during all experiments.

A current density range (between 0 - 150 $mA\,cm^{-2}$) is applied to obtain *I-V* curves for analysis, and to associate current density to ion cross-over. After an experiment, the electrolyte samples (both catholyte and anolyte) are examined by analytical measurement methods to observe the quantity of ion cross-over.

After the characterization of the BPM with multiple catholyte solutions, an up-scaling experiment is performed. In this experiment a larger flow-cell is used that has a BPM surface area of 100 cm^2 instead of 10 cm^2 used in the previous described experiments. The results obtained in this experiment can be related to the characterization experiments performed previously.

[1]The H-cell is a double compartment cell that consists of two electrolytes separated by an ion exchange membrane. There is no flow in this set-up, thus magnetic stirrers are used to prevent diffusion resistances in the electrolytes [79].

Table 3.1: The difference in BPM surface area and point of interest for two different approaches in this research.

	BPM surface area	**Point of interest**
Approach 1	10 cm^2	Characterization BPM and ion cross-over
Approach 2	100 cm^2	Up-scaling

3.2. Experimental set-up and equipment

All experiments were performed in commercial electrochemical cells provided by ElectroCell. The characterization experiments (approach 1) were carried out in a Micro Flow Cell® and the up-scaling experiments (approach 2) were performed in an Electro MP Cell® [8]. The specifications and technical data for these set-ups can be found in appendix B. This section describes the experimental set-up for the Micro Flow Cell (Approach 1), however, the Electro MP Cell (approach 2) has a similar set-up regardless of the size differences. Figure 3.1 demonstrates the required components for the formation of the flow-cell for approach 1.

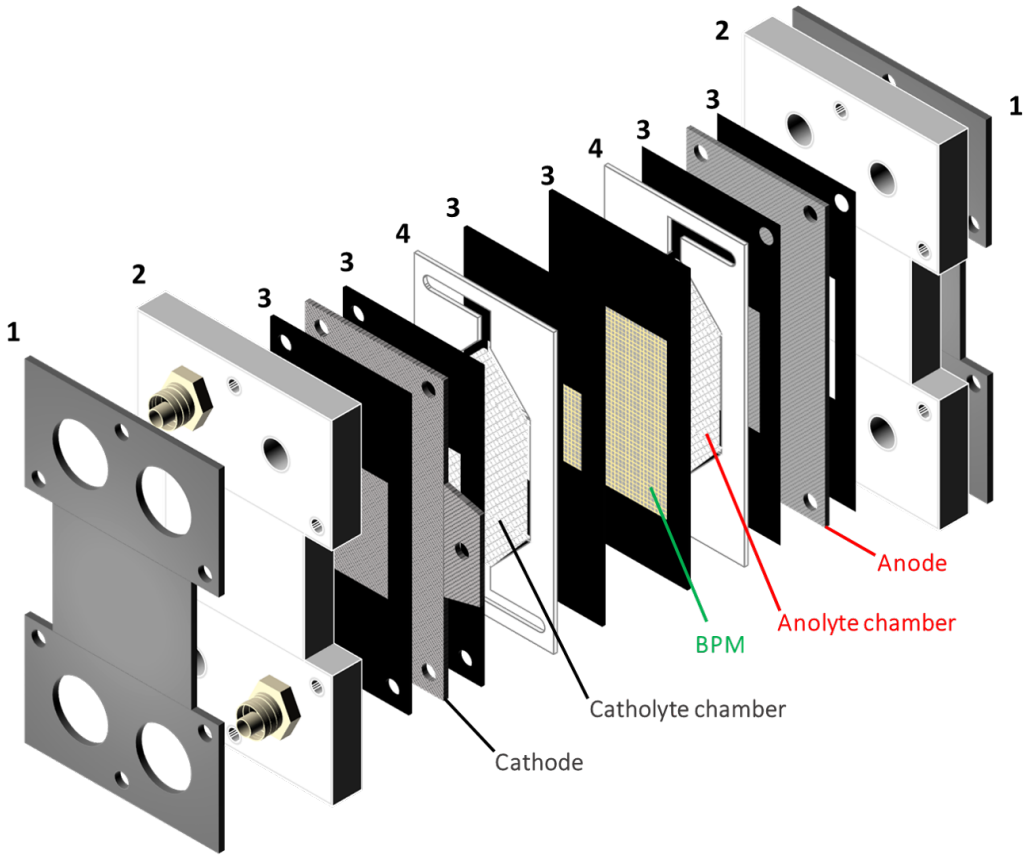

Figure 3.1: Schematic overview of the Micro Flow Cell used for characterization of the BPM. The flow-cell consists of multiple layers that can be held together by six bolts. From left to right: stainless steel endplates (1), PTFE endframes (2), rubber gaskets (3), the platinum cathode (or anode), PTFE flow frames including a PVDF turublence mesh that form the catholyte- and anolyte chamber (4) and a Fumasep BPM [5] between two rubber layers.

In this research two platinum electrodes were used for the cathode and anode. It is known that in alkaline conditions (pH 14) the oxygen revolution reaction (OER) undergoes stable operation with a nickel electrode (as the anode) [19]. However, initial testing proved that the nickel was in fact unstable for alkaline concentrations of 0.5 M (pH 13.7), since dissolved nickel particles were encountered in the anolyte. To ensure stability (and no nickel particles in the samples), a platinum electrode was used for the anode instead.

For experiments a Fumasep BPM® was utilized [5]. The Fumasep BPM technical specifications can be

found in appendix B. Before testing a current density range for a specific electrolyte a new piece of BPM was cut (slightly bigger than the 10 cm^2 surface area in the flow-cell to prevent ruptures and leakage). The piece of membrane was then soaked for about 20 minutes in a 1M NaCl solution before placing it between the two rubber layers in the middle of the flow-cell. The polytetrafluoroethylene (PTFE) flow frames (4 in figure 3.1) have polyvinylidene fluoride (PVDF) turbulence meshes inserted within them to create equal flow in the flow chambers and limit the formation of stagnant regions during flow. PTFE and PVDF are non-reactive thermoplastics that provide structure and mechanical strength to the flow-cell set-up.

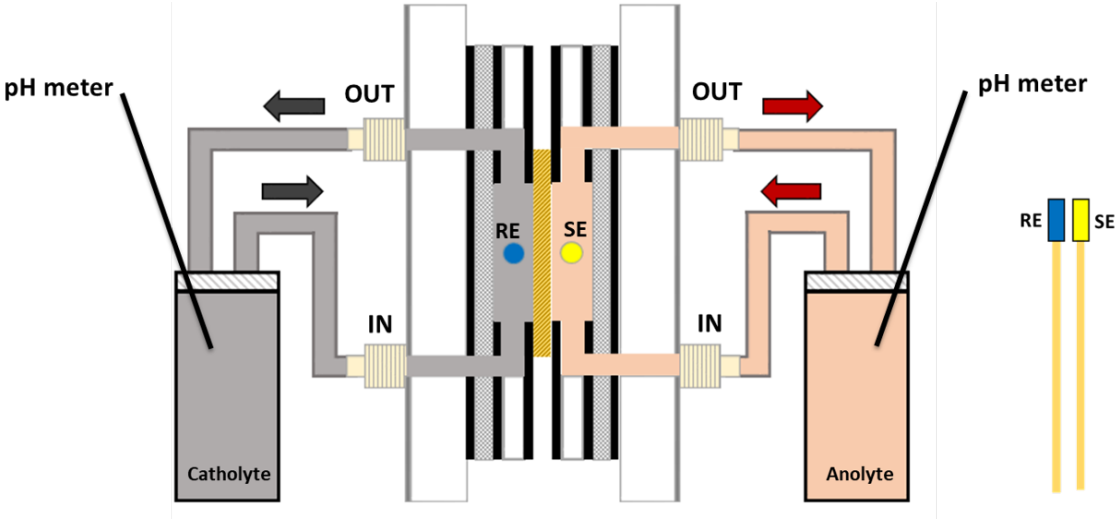

Figure 3.2: Schematic representation of the flow-cell set-up cross section. The catholyte (grey) and anolyte (red) have a flow direction equal to the arrows. The voltage over the BPM is measured by a reference electrode (RE) and a sense electrode (SE) that are close to the BPM in the catholyte chamber and anolyte chamber, respectively. Both electrolytes are measured *in situ* with a pH meter.

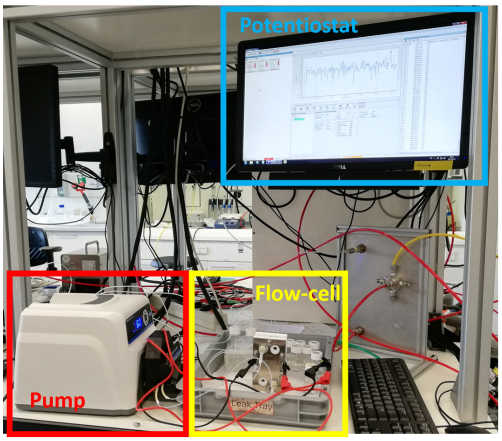

(a) Micro Flow Cell set-up [8].

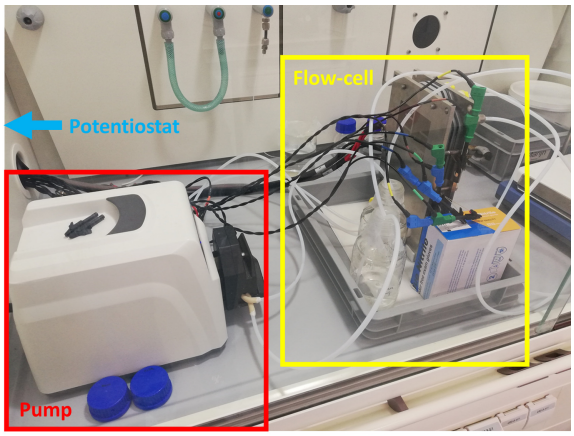

(b) Electro MP Cell set-up [8].

Figure 3.3: Set-up for small flow-cell (a) and big flow-cell (b) with a BPM surface area of 10 cm^2 and 100 cm^2, respectively. The flow cells (yellow boxes) are connected to a pump (red box) with tubes. The flow cell is also connected with electric cables to a potentiostat, which is connected to a computer (blue box) for data analysis. The small flow-cell is connected to a PARSTAT MC potentiostat® [6] and the big flow-cell to a EnergyLab XM® potentiostat [7].

Before an experiment, the prepared electrolytes are deposited in 20 mL vials that are connected to the flow-cell with tubes, as can be seen in figure 3.2. The tubes contain a rubber section that can be placed in a pumping device. During experiments the pH was measured in the catholyte with a Hanna Instruments® 5222 pH meter [82]. Ideally, the bulk pH of both the catholyte and anolyte would be measured *in situ* (as can be seen in figure 3.2). Unfortunately, only one pH meter was available for these experiments. Since the catholyte composition is of most interest for this thesis, it was decided to measure only the catholyte pH.

The flow-cell is connected to a PARSTAT MC potentiostat galvanostat[2], that can apply a current over the electrodes and measure the potential over the BPM. Figure 3.3 demonstrates this set-up for both approach 1 (a) and approach 2 (b).

3.3. Chemicals and solutions

As mentioned previously, this research aims to characterize the behaviour of ion cross-over though a BPM. To investigate this, multiple catholyte buffer solutions have been chosen in a specific pK_a range. More information on the relation between pK_a and pH can be found in the next subsection. Since the effect of extreme pH values has already been observed [3], the chosen pK_a groups are 2, 7, 9 and 10. The anolyte is a 0.5M NaOH solution for all experiments.

Goldberg *et al.* performed an analysis of different buffers and their thermodynamic qualities [9]. They rated every buffer with a triple letter status (*e.g.*, AAA status for reliable pK_a values), which was taken into account when choosing the buffers. All of the chosen buffers have at least an AAB status (but most have triple A status), which also explains why the specific pK_a groups (2, 7, 9 and 10) were chosen, for there were not enough high rated buffers at other values (*e.g.*, pK_a 4). This rating system ensures us that all theoretical thermodynamic pK_a values of the chosen buffers are correct and are not influenced drastically by changes in the system. Every catholyte solution has a 0.5 molarity (mol/L) and has been, if necessary, modified to a pH environment equal (or close to) its pK_a value. The chosen buffers can be found in table 3.2. A phosphate buffer is used twice at pK_a values 2 and 7, which is why they are mentioned as $phosphate_2$ and $phosphate_7$, respectively. More information on the prepared solutions, such as chemical purity and/or pH modifications can be found in appendix C.

Table 3.2: Catholyte buffer solutions tested in experimental set-up. All pK_a values are obtained from Goldberg *et al.* [9].

Group	Buffer solution	Chemical formula	pK_a
2	Tricine	$C_6H_{13}NO_5$	2.023
2	$Phosphate_2$	H_3PO_4 / H_2KPO_4	2.148
2	Glycine	$C_2H_5NO_2$	2.351
7	MOPS	$C_7H_{15}NO_4S$	7.184
7	BES	$C_6H_{15}NO_5S$	7.187
7	$Phosphate_7$	H_2KPO_4 / HK_2PO_4	7.198
9	AMPSO	$C_7H_{15}NO_5S$	9.138
9	Boric acid	H_3BO_3	9.237
10	Potassium bicarbonate	$KHCO_3$	10.329
10	CAPS	$C_9H_{19}NO_3S$	10.499

3.3.1. pKa, pH and titration

The chemical solutions in table 3.2 are chosen due to their specific pK_a values. This section explains briefly what the relationship is between pH and pK_a, and why this is relevant for this thesis. Additionally, titration (common analytical method) is introduced and its measurements for every electrolyte solution are given.

The pK_a is the logarithmic constant of the K_a, the *acid dissociation constant*, which is a quantitative measure of the strength of an acid in solution. The chemical equation 3.1 introduces HA, a generic acid that dissociates into A^-, the conjugate base of the acid and a proton, H^+. These species are in equilibrium when all concentrations remain constant (even though the separate reactions are occurring at a very fast rate) [83].

[2]A potentiostat is an electronic device that can be utilized for electroanalytical experiments. The PARSTAT MC can deliver high compliance voltage and wide dynamic current range, to cover a range of applications [6].

$$HA \rightleftharpoons A^- + H^+ \tag{3.1}$$

$$K_a = \frac{[A^-][H^+]}{[HA]} \tag{3.2}$$

$$pK_a = -\log_{10}(K_a) = pH - \log_{10}\left(\frac{[A^-]}{[HA]}\right) \tag{3.3}$$

Weaker acids have a more positive value for the pK_a, which leads to a smaller extent of dissociation at any given pH. Equation 3.3 shows how to calculate the pK_a for a weak acid and its conjugate base. The outcome of equation 3.3 (also known as the Henderson-Hasselbalch equation), can provide the following conclusions: **(1)** when pH=pK_a the concentration of HA is equal to A^-, **(2)** the buffer region extends over the approximate range pK_a ±2 and **(3)** if the pH is known, the concentration ratio can be calculated. This ratio is independent of the analytical concentration of the acid. As mentioned in the chapter 2, it is known that pH has an effect on the BPM voltage and on ion cross-over [3, 4, 72]. This effect, however, can be excluded if one experiments with a pH value close to the pK_a value of their solution. In this case, the concentration of HA is equal to A^-, which means that the concentration ratio $A^-/HA \approx 1$. The effect of the pH on the concentration ratio of a buffer is given in subfigure 3.4b. This Bjerrum plot shows the pK_a values of a carbonate solution and how the concentration ratio changes when the pH increases/decreases around these pK_a values. This plot might be for carbonate, but similar plots can be found for other buffers (*e.g.*, phosphate, glycine etc.).

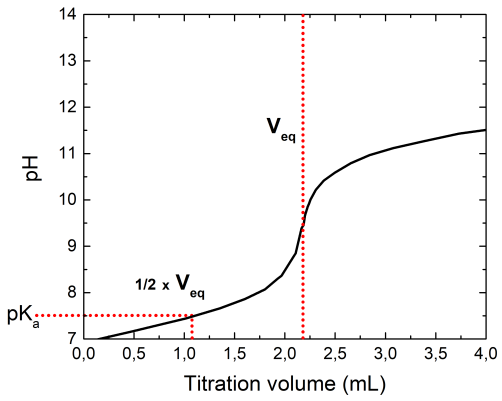

(a) A titration curve obtained from titrating a 0.5M phosphate$_7$ buffer with 1M KOH. The titration volume required to reach the equivalence point is given by V_{eq}. At half this volume ($\frac{1}{2} \times V_{eq}$) the species are in equilibrium which gives the pK_a value of the 0.5M phosphate$_7$ buffer.

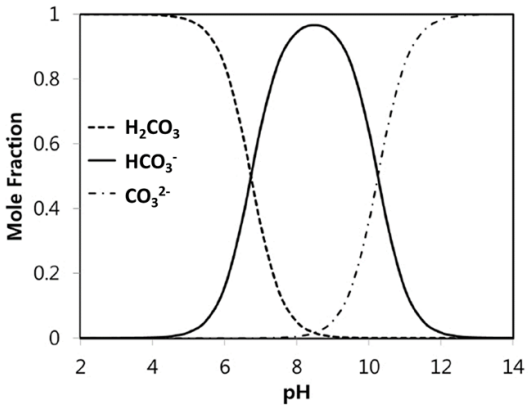

(b) Bjerrum plot showing the pH dependence of carbonic acid (H_2CO_3), bicarbonate (HCO_3^-) and carbonate (CO_3^{2-}). As the pH shifts, the concentration ratio of these components changes. The pK_a values for carbonate are 6.351 and 10.329, as can be seen in the plot [2, 9, 84].

Figure 3.4: A titration curve (a) and a bjerrum plot (b).

The pK_a of an electrolyte can be measured with titration. Titration is a common laboratory method of quantitative chemical analysis that is used to determine the concentration (and/or pK_a) of an acidic or alkaline solution. Titration is performed by adding small drops of a strong acid or alkaline solution into the sample of interest. When the buffer capacity of this sample is depleted, the equivalence point (chemically equivalent quantities of bases and acids have been mixed) is reached. Next, the pH value is measured at half this volume as being equal to the pK_a, as shown in figure 3.4a. It is important to measure the pK_a with titration for every solution, since the temperature and the molarity influence the K_a, meaning that theoretical values might differ from the values of the prepared samples.

Initially, titration was seen as a method to observe ion cross-over. However, ion cross-over occurs in such small quantities that it could not accurately be observed with titration measurements. Hence, only inductive coupled plasma- optical emission spectrometry (ICP-OES) and nuclear magnetic resonance (NMR) spectroscopy (subsections 3.5.1 and 3.5.2) were utilized for ion cross-over. Nonetheless, the titration results can indicate the pK_a value of the solution. For this research a Metrohm 848 Titrino plus® was used [85].

Table 3.3 shows the theoretical pK_a values and the obtained pK_a values. Nearly all solutions were titrated multiple times, and an average pK_a value was taken.

Table 3.3: Theoretical pK_a values versus titration pK_a values for all catholyte solutions.

Catholyte solution	**Theoretical pK_a [9]**	**Titration pK_a**
Tricine	2.023	2.4
$phosphate_2$	2.148	2.5
Glycine	2.351	2.7
MOPS	7.184	7.0
BES	7.187	7.1
$phosphate_7$	7.198	7.5
AMPSO	9.138	8.8
Boric acid	9.237	8.2
Potassium bicarbonate	10.329	9.7
CAPS	10.499	10.2

3.4. Experiment sequence

This section describes the experiment sequence for one unspecified buffer solution. This sequence has been performed precisely for all buffer solutions (table 3.2), to ensure similar conditions for all experiments.

First, preparations are made before starting the experiment. The desired catholyte (0.5M) and anolyte (0.5M NaOH) are prepared and a piece of the BPM is cut to fit in the electrochemical configuration, after which it is soaked in a 1M NaCl solution (the preferred storage solution as mentioned by the manufacturer [5]) for roughly 20 minutes. The BPM is then carefully placed between the two rubber layers with the cation exchange layer (CEL) directed towards the cathode and the anion exchange layer (AEL) directed towards the anode. This is vastly important, because the interim layer may degrade (blistering), and the monolayers may delaminate, when the membrane has been installed reversed [5].

With the membrane in place, the flow-cell can be assembled as shown in figure 3.1. The reference electrode and sense electrode are installed on both sides of the BPM by placing them through a small drilled hole in both the PTFE flow frames (figure 3.1). It is essential to place the electrodes as close to one another as possible with the membrane in between, to allow an accurate measurement of the potential across the BPM and minimizing the ohmic losses of the electrolytes. Additionally, the electrodes should not be pushed into the flow chamber entirely, since gas bubbles formed during experiments affect the measured potential in the form of noise. With everything in place, the cell can be built and the bolts can be tightened with a ratchet wrench with a momentum of 4 N × m, until the ratchet wrench clicks. This is to prevent the BPM from rupturing. The tightening of the bolts occurs gradually by dividing the load equally across all six bolts to prevent shear on the PTFE blocks.

Thereupon, the flow-cell is placed in a leak tray and all the tubing[3] is attached to the flow cell and the rubber tubing section is placed in the pump. First a leak test is performed with distilled water in both electrolyte compartments. The flow for all experiments, including the leak test and rinsing, is 0.07 $cm^3\,s^{-1}$. If the leak test fails, the flow-cell is reassembled.

Thereafter, the electrical wires from the potentiostat can be attached to the electrodes and reference electrodes. In some experiments multiple potentiostat channels were used, which allows the potentiostat to not just measure the BPM voltage, but also the total cell voltage and the cathode and anode voltage. However, the BPM potential is most important for this thesis, thus one channel is essential. The set-up is now ready for an experiment, but first the BPM, flow chambers and tubes must be rinsed to ensure that all impurities are out of the system and that only the tested solutions are present in the system.

Before the first experiment can be run, a long rinsing scan is performed to eliminate all the left over Na^+ ions and Cl^- ions from the storage solution out of the BPM. The water (for the leak test) is replaced with new

[3] The tubing needs to be fastened correctly to the in- and outlets of the flow-cell, as explained in figure 3.2. The tubing is self-made and the transitions are covered with epoxy adhesive to prevent leakage.

10 mL electrolyte solutions for both the catholyte and anolyte. Rinsing program 1 is a galvodynamic scan which starts at a current density of 150 mA/cm^2 and slowly decreases to -10 mA/cm^2 with a scan rate of 0.1 mA/cm^2/s. The rising samples are then replaced with fresh 10 mL samples for rinsing program 2. This quick program increases the current density from 0 to 150 mA/cm^2, with a scan rate of 1 mA/cm^2/s. Rinsing program 2 is done in between experiments to deplete[4] the membrane of leftover ions from the electrolyte solutions, while rinsing program 1 is only necessary before the first experiment, because of the storage solution ions in the BPM. Table 3.4 summarizes the galvodynamic programs.

Table 3.4: Galvodynamic programs for rinsing and experiments performed by the PARSTAT MC potentiostat [6].

Method	Galvodynamic program	Scan rate	Time (s)	Electrolyte volume (mL)
Rinsing 1	150 to -10 mA/cm^2	0.1 mA/cm^2/s	1600	10
Rinsing 2	0 to 150 mA/cm^2	1.0 mA/cm^2/s	150	10
Experiment	Constant current	-	2700	20

During initial test experiments, the effect of rinsing has been observed. This was done to conclude how many rinsing rounds are necessary to 'clean' the BPM before a new experiment is started. After an experiment, rinsing 2 was done twice with new samples. Thereupon, the samples were collected and sent for ICP-OES analysis, which is explained in the next section. The ICP-OES results in table 3.5 display the concentration of catholyte ions in the anolyte solution and vice versa. If these concentrations are high, it means that these ions were still present in the BPM, thus low concentrations are preferred. Table 3.5 demonstrates that after the first rinsing round the ion concentration decreases to negligible levels, since the concentration in the opposite electrolyte is 500 mmol/L. These concentrations have also been found in reference samples that have not been used for any experiments, concluding that one rinsing round in between experiments is adequate. Additionally, the concentration does not decrease further after an extra rinsing round, thus extra rinsing rounds are not necessary.

Table 3.5: ICP-OES results after rinsing 2 for the catholyte (0.5M phosphate$_2$) and anolyte (0.5M NaOH) samples.

Rinsing round	Na^+ in catholyte (mmol/L)	$H_2PO_4^-$ in anolyte (mmol/L)
1	1.3	0.6
2	1.3	0.6

Now that the rinsing is completed, the rinsing samples are replaced with new samples (20 mL) and an experiment can be performed. For every catholyte a range of current densities (0 – 150 mA/cm^2) is tested. This is done by applying a constant current density for 45 minutes at 0, 0.5, 1, 2, 4, 8, 12.5, 25, 50, 100 and 150 mA/cm^2. For every experiment one of these current densities is randomly chosen until they are all tested. This random picking is done to prevent standard sequences for each electrolyte. This must be prevented, since the aging and the state of the BPM play an important role in ion cross-over. When an experiment is run, the pH is measured *in situ* and the BPM voltage (displayed on the potentiostat computer) is checked regularly. The pH and BPM voltage should remain fairly constant and if this is not the case there could be major leakage, a BPM rupture or other issues influencing the system. If the experiments are performed successfully, the 20 mL samples for all current density values are collected and analyzed to observe ion cross-over. Section 3.5 describes the analytical methods.

This section describes a step-to-step manual for current density range experiments with the 10 cm^2 surface area Micro Flow Cell. In addition, an up-scaling experiment has been performed. Even though the approach is fairly similar, some differences are worth mentioning and therefore the next subsection describes the up-scaling experiment.

3.4.1. Up-scaling the BPM surface area

Up-scaling the electrochemical configuration is an important aim for this research, since it simulates conditions that are expected in industrial applications. The BPM surface area is increased from 10 cm^2 to

[4]Rinsing program 2 increases the current density, which enables the water dissociation reaction to push out leftover ions. More information on the migration of ions at high current densities can be found in the chapter 2.

100 cm^2 by switching to an Electro MP Cell (figure 3.3b). The configuration and cross-section is similar to the Mirco Flow Cell, as demonstrated in figures 3.1 and 3.2. However, the dimensions are ten times larger. The technical specifications can be found in appendix B.

The assembling of the large flow-cell is similar to the 10 cm^2 flow-cell, except for a few differences. First, the anode is a nickel electrode and the cathode is a platinum electrode. For the large set-up, the choice was limited to these two electrodes. Fortunately, no (noticeable) nickel dissolved into the anolyte during experiments. Second, the membrane sheet (with the correct dimensions) was prepared by the manufacturer. Third, the bolts were tightened with a momentum of 7 N × m.

The electrolyte volume was determined by performing a leak test with measuring cylinders. The chambers in the flow-cell have a volume of 180 mL, therefore 220 mL was chosen to maintain the flow if leakage occurs. To achieve the same current density values as in previous experiments, the current needs to be increased ten times, since the scale of this operation is ten times larger compared to the previous flow-cell. For a current density of 10 mA/cm^2, the potentiostat needs to apply 1 A, compared to the 0.1 A in the smaller flow-cell. For the chosen current density range (0 - 150 mA/cm^2), currents over 10 A are required. To produce such a current, a Solartron® power booster is connected to the EnergyLab XM potentiostat [86].

Initial testing concluded that the system could not cope with currents above 3 A, since the total cell voltage exceeded the maximum applicable voltage of the potentiostat. Therefore the current density range had to be adjusted to 0, 0.5, 1, 2, 4, 8, 12.5 and 25 mA/cm^2. The rinsing in between experiments was executed with a 500 mL rinsing solution (one for every electrolyte), that can be recycled for every rinsing round. Proper rinsing is less relevant due to the larger volumes in this set-up, thus a contamination has less impact. New solutions were used for every current density experiment. The pH in both the catholyte and anolyte was measured before and after the experiment and 20 mL samples were taken after an experiment for analysis. Table 3.6 gives the galvodynamic programs that were utilized.

Table 3.6: Galvodynamic programs for rinsing and experiments performed in an Electro MP Cell by the EnergyLab XM potentiostat [7].

Method	**Galvodynamic program**	**Scan rate**	**Time (s)**	**Electrolyte volume (mL)**
Rinsing	0 - 25 mA/cm^2	1 $mA/cm^2/s$	25	500
Experiment	Constant current	-	2700	220

3.4.2. Co-ion permeation

In chapter 2, mass transfer of ions through the BPM in the form of migration and diffusion is described. The obtained data during and after experiments can be utilized to theoretically calculate this ion cross-over and the effect it has in both electrolytes. An interesting parameter is co-ion permeation, which is the percentage of co-ions (not H^+ or OH^-), that cross over through the membrane instead of H^+ or OH^- formed by the WDR. Co-ion permeation is calculated for both the catholyte (equation 3.4) and the anolyte (equation 3.5).

$$\text{Co-ion permeation catholyte (\%)} = \frac{\text{Ion cross-over from anolyte to catholyte (mol)}}{\text{H}^+ \text{ produced in WDR (mol)}} \times 100\,\% \tag{3.4}$$

$$\text{Co-ion permeation anolyte (\%)} = \frac{\text{Ion cross-over from catholyte to anolyte (mol)}}{\text{OH}^- \text{ produced in WDR (mol)}} \times 100\,\% \tag{3.5}$$

The ion cross-over (mol) from anolyte to catholyte (or vice versa) is obtained from ICP-OES or NMR results. The concentration (g/L) of the anolyte ion (Na^+) is measured in the catholyte samples for every current density experiment. Divide this concentration with the molar weight of Na^+ (g/mol) and multiply it with the electrolyte volume (L), and the total one-directional cross-over (mol) from the anolyte to the catholyte can be calculated. This value is divided by the theoretical value for consumed reactant in the electrolyte. In the catholyte, for instance, the hydrogen evolution reaction (HER) consumes protons to form hydrogen gas (H_2). The consumed protons (mol) can be calculated with Faraday's law (equation 2.16 in chapter 2) for every chosen current density. Ideally, the amount of protons consumed in the HER is replaced by the water

dissociation reaction. Thus, equations 3.4 and 3.5 actually describe the percentage of ions that permeate the membrane, instead of a H^+ or OH^- formed by the WDR.

3.5. Analytical methods

This section describes the used analytical methods to measure the extend of ion cross-over in the collected samples. Most samples were investigated with ICP-OES, however, some could not be measured with this technique, thus NMR spectroscopy was used instead. The pH values, that were measured during experiments, can be correlated to the pK_a values measured with titration. In addition, the conductivity was measured for every solution, since this influences the measured BPM voltage. Hence, a conductivity correction was performed for all experiments.

3.5.1. ICP-OES

Inductive coupled plasma- optical emission spectrometry (ICP-OES) is a robust technique that measures the composition and concentration of elements in a solution. The sample of interest is pumped into the ICP-OES, where it evaporates into an aerosol [87]. The aerosol then travels with an argon gas stream into an argon plasma[5]. The electrons are then accelerated with an alternate magnetic field, thus colliding with the argon atoms and electron ionization occurs. Due to the thermic energy taken up by the electrons, each element emits a characteristic spectrum in the ultraviolet and visible region. The light intensity at one of the characteristic wavelengths is proportional to the concentration of that element in the sample [87–89].

ICP-OES measurements were performed by Baukje Terpstra, Department Radiation, Science & Technology (RST), Section Applied Radiation and Isotopes (ARI). All samples were diluted in 8% HNO_3 (100 times). The samples were analyzed with the PerkinElmer Optima 5300 ICP-OES [90].

3.5.2. Quantitative NMR spectroscopy

Nuclear magnetic resonance (NMR) spectroscopy is a spectroscopic technique to observe local magnetic fields around atomic nuclei. It enables a unique and, in principle, quantitative determination of the relative amount of molecular groups, thus offering a tool to quantify entire molecular structures even in mixtures [91]. In this thesis, NMR was used for the glycine and tricine cross-over measurements, since these molecules cannot be identified by ICP-OES.

NMR measurements were performed by Martin Kolen, Materials for Energy Conversion and Storage (MECS), Applied Sciences, TU Delft. The measurement data be found in appendix D.

3.5.3. pH

The pH is measured *in situ* for all experiments with a Hanna Instruments® 5222 pH meter. This is done, not only to check if the system remains stable, but also to relate a change in pH to ion cross-over. Equation 3.6 gives the relation between pH and the concentration of H^+. Thus, the concentration of H^+ can be calculated at the beginning of an experiment ($[H^+]_{in}$) and at the end ($[H^+]_{out}$). The total change in H^+ concentration can be calculated with equation 3.9.

$$pH = -\log_{10}[H^+] \tag{3.6}$$

$$[H^+]_{in} = 10^{-pH_{in}} \tag{3.7}$$

$$[H^+]_{out} = 10^{-pH_{out}} \tag{3.8}$$

$$\Delta[H^+] = ([H^+]_{out} - [H^+]_{in}) \times V_{electrolyte} \tag{3.9}$$

The pK_a of every solution is also known. Thus, combining the pK_a value with the calculated H^+ concentrations (in and out), the concentration ratio at the beginning of the experiment (equation 3.11) and at the end of the experiment (equation 3.12) is calculated.

[5]Plasma is the forth state of matter, next to the solid, liquid and gaseous state [87].

$$K_a = 10^{-pK_a} = \frac{[A^-][H^+]}{[HA]} \tag{3.10}$$

$$\frac{K_a}{[H^+]_{in}} = \frac{[A^-]_{in}}{[HA]_{in}} \tag{3.11}$$

$$\frac{K_a}{[H^+]_{out}} = \frac{[A^-]_{out}}{[HA]_{out}} \tag{3.12}$$

Thereupon, X_{in} and X_{out} (mol) are calculated. These values present the concentration of catholyte X at the beginning and the end of an experiment. The total change in X is calculated with equation 3.15. Thereafter, the total ion cross-over (from ICP-OES/NMR results) is divided by the sum of $\Delta[H^+]$ and ΔX, as given in equation 3.16. Theoretically the answer to this equation should be equal to one, since the total ion cross-over includes the Na^+ from the anolyte to the catholyte (= $\Delta[H^+]$) and the anion cross-over from catholyte to anolyte (= ΔX). More information on ion cross-over is given in chapter 2.

$$X_{in} = \frac{0.5 \times \frac{K_a}{[H^+]_{in}}}{1 + \frac{K_a}{[H^+]_{in}}} \tag{3.13}$$

$$X_{out} = \frac{0.5 \times \frac{K_a}{[H^+]_{out}}}{1 + \frac{K_a}{[H^+]_{out}}} \tag{3.14}$$

$$\Delta X = (X_{out} - X_{in}) \times V_{electrolyte} \tag{3.15}$$

$$\frac{\text{Total ion cross-over}}{\Delta[H^+] + \Delta X} \approx 1 \tag{3.16}$$

3.5.4. Conductivity

Table 3.7: Measured specific conductance (κ_{real}) versus theoretical specific conductance (κ_{theory}) for all 0.5M electrolytes.

Catholyte	κ_{real} **(mS/cm)**	κ_{theory} **(mS/cm)**
Tricine	21.6	-
$Phosphate_2$	26.0	19.5 [92]
Glycine	26.4	-
MOPS	11.5	-
BES	14.7	-
$Phosphate_7$	52.3	34.8 [93]
AMPSO	13.0	-
Boric acid	16.5	25.67 [94]
Potassium bicarbonate	70.8	38.8 [93]
CAPS	10.8	-
Anolyte	κ_{real} **(mS/cm)**	κ_{theory} **(mS/cm)**
Sodium hydroxide	100.0	98.6 [92]

Every catholyte has a different ionic conductivity value, because of its chemical composition. This electrolytic conductivity (as explained in chapter 2, section 2.2) affects the measured voltage during galvodynamic experiments. The reference electrode (RE) and sense electrode (SE) are close to the CEL and AEL, respectively. However, the voltage over the BPM that they measure includes the small distance through both electrolytes, with the respective ohmic losses. These ohmic losses need to be accounted for, since they differ for every solution. Therefore, the specific conductance was measured with a conductivity meter for

every solution. Table 3.7 demonstrates the measured values and the theoretical values for all catholytes and the anolytic NaOH solution.

Most catholytes are modified with KOH/HBr to increase/decrease the pH towards its pK_a value. The theoretical conductance for these solutions can either not be found in literature, or can only be found for a pure 0.5M solution, which does not take these modifications (appendix C) into account. Only the phosphate buffers and sodium hydroxide can be compared to their theoretical values. $Phosphate_2$ has a higher measured specific conductivity than its theoretical value. However, $phosphate_2$ consist of 0.25M H_3PO_4 and 0.25M H_2KPO_4, while the theoretical value is for 0.5M H_3PO_4 only. K^+ increases the specific conductance, as can be seen for $phosphate_7$, which contains more potassium. The theoretical value of the specific conductivity for $phosphate_7$ is for 0.5M H_2PO_4 only.

The ohmic loss between the reference electrode and the sense electrode is calculated with equation 2.15 in section 2.3. The conductivity (L) is the specific conductance for a solution (κ) times the surface area (A) divided by l, the distance between the RE and SE [45]. The specific conductance for every electrolyte is known (table 3.7) and the surface area is 10 cm^2 for experiments in the Micro Flow Cell (and 100 cm^2 for the Electro MP Cell). Therefore, only the distance between the electrodes must be measured and all experiments can be corrected for conductivity losses. The technical data (figure B.1, appendix B) for the Micro Flow Cell mentions that the standard electrode gap is **4 mm**.

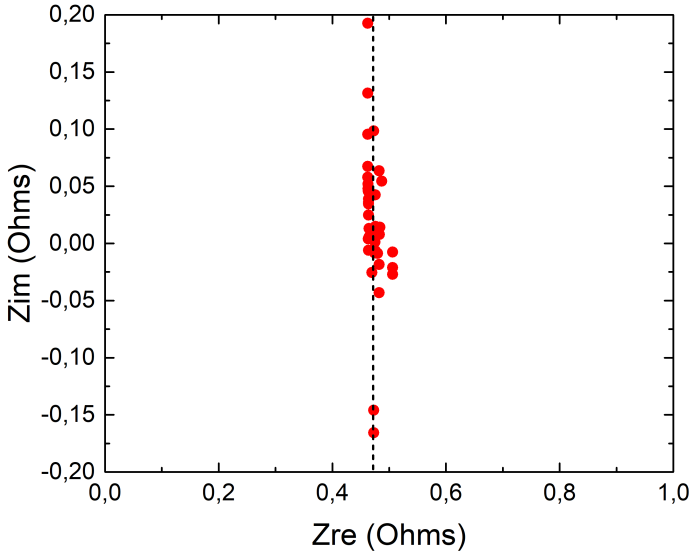

Figure 3.5: Graph showing an electrochemical impedance spectroscopy (EIS) measurement taken from 10000 Hz to 1 Hz. The ohmic loss between the reference electrode and the sense electrode in the electrochemical cell without a bipolar membrane and 0.5M NaOH electrolyte in both the catholyte and anolyte are calculated. The imaginary impedance (Zim) and the real impedance (Zre) are plotted on the y-axis and x-axis, respectively. The Zre shows a straight line around 0.48 Ohms, which is the ohmic loss between the RE and SE in a 0.5M NaOH solution.

For comparison, an electrochemical impedance spectroscopy (EIS) measurement is performed, to measure the ohmic losses in the electrochemical cell with no bipolar membrane and a 0.5M NaOH solution in the catholyte and anolyte. Figure 3.5 demonstrates that the ohmic loss between the RE and SE is approximately 0.480 Ω, which is 2.083 S. With this value the distance between the electrodes (l) is calculated, with κ_{NaOH} is 100.0 mS/cm. This results in a distance (l) of **4.8 mm**, which seems reasonably compared to the given standard electrode gap [8]. In this experiment, no BPM was placed in between the catholyte and anolyte. Therefore, the thickness of the BPM, which is 130-160 microns (0.13-0.16 mm), is accounted for in further conductivity corrections [5]. The final distance between the RE and the BPM (and the distance between the BPM and SE) is **2.33 mm**, since the BPM is in the middle. Table 3.8 summarizes the calculated distances.

The conductivity for the distance BPM-SE (in the anolyte) is equal for all performed experiments, for a 0.5M

Table 3.8: Distances between the reference electrode (RE), the sense electrode (SE) and the BPM. Distance l was measured with EIS and the BPM thickness is given in the Fumasep technical data [5].

Distance RE-SE (l)	**BPM thickness**	**Distance RE-BPM and BPM-SE**
4.80 mm	0.13-0.16 mm	2.33 mm

NaOH solution is always utilized. The conductivity for the distance RE-BPM (in the catholyte) changes for the different catholytes (specific conductivities can be found in table 3.7). For every experiment (and every current density) the BPM voltage can be corrected for these ohmic losses. The conductivity is actually the inverse of resistance (R=1/L) and the total 'ohmic loss' resistance is the sum of the resistance between the RE and the BPM (in the catholyte) and the resistance between the BPM and the SE (in the anolyte), which is true for resistances in series, as shown in equation 3.17 [45].

$$R_{ohmic} = R_{catholyte} + R_{anolyte} \tag{3.17}$$

R_{ohmic} contains all the resistances that cause ohmic losses between the reference electrode and the sense electrode, without the BPM resistance. Therefore, when every current density step in every experiment is corrected for conductivity, only the true BPM potential remains. This is done by calculating the overpotential that is related to ohmic losses (equation 3.18) and by subtracting this overpotential from the measured potential (equation 3.19). I is the applied current and varies for every current density step.

$$E_{ohmic} = I \times R_{ohmic} \tag{3.18}$$

$$E_{BPM} = E_{measured} - E_{ohmic} \tag{3.19}$$

Figure 3.6 demonstrates the shift in potential for a corrected experiment. The resistance produces more overpotential for higher currents, which is why the potential correction increases for higher current densities.

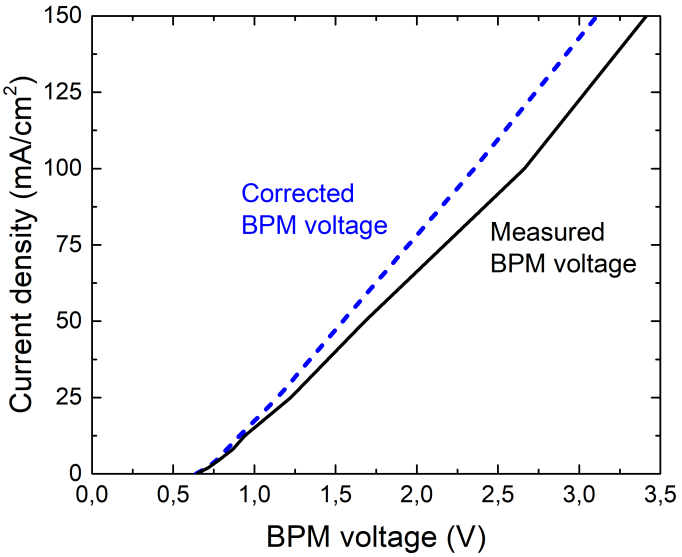

Figure 3.6: Graph demonstrating an I-V curve for the current density versus the BPM potential. The catholyte is 0.5M phosphate$_2$ and the anolyte is 0.5M NaOH. The black line indicates the measured BPM voltage, as measured by the potentiostat, and the blue dashed line demonstrates the BPM voltage that is corrected for conductivity losses.

4

Results

This chapter presents the experimental results obtained during this thesis. First, the error and reproducibility of the results are given. Next, the results of the different pK_a groups are presented and compared, in sections 4.2-4.5. Thereupon, this chapter continues to focus on similarities and particularities encountered in all experiments, in section 4.6. Finally, it proceeds with the results of some additional experiments that have been performed. A summary of the chapter can be found in section 4.8.

Co-ion cross-over is discussed frequently in this chapter, thus it is important to mention that Na^+ cross-over is always from the anolyte to the catholyte and is represented in black, since the Na^+ ions cross over into the catholyte (black), due to the applied electrical field and/or a concentration gradient. This holds true for the ion cross-over from the anolyte to the catholyte since a **0.5M NaOH** anolyte has been used for all experiments. The cross-over from the catholyte to the anolyte depends on the catholyte solution used, but is always represented in red (the colour of the anolyte). The catholyte ions that are observed for cross-over are always negatively charged (or uncharged), except for glycine and tricine, which is described in section 4.2. Chapter 2 provides more detailed information on ion cross-over.

4.1. Error and reproducibility of results

The reproducibility of results is emphasized throughout this chapter. Therefore, it is chosen to begin with this section. During experiments, it was encountered that the state of the bipolar membrane has a significant effect on the electrochemical system, especially on ion cross-over. Consequently, multiple experiments were repeated to observe this effect.

The first experiments that were performed for this project were with the electrolytes from the pK_a 2 group (glycine, tricine and $phosphate_2$). For convenience, it was chosen to repeat these experiments, since their results and behaviour are well understood. Glycine and tricine were performed twice, and the $phosphate_2$[1] buffer three times. For a description of the experimental procedure chapter 3 can be consulted.

Figure 4.1a demonstrates the I-V curve for $phosphate_2$, which has been repeated three times. The utilized bipolar membranes differ in storage time and batch, since the first experiments were performed in November 2018, while the last experiments were performed in May 2019, with a new batch that was stored for a longer time. The age and state of the BPM influences the BPM voltage and ion cross-over. It is demonstrated in subfigure 4.1b that the older 2019 BPM has a lower BPM voltage, which indicates more co-ion permeation [3, 72]. This is indeed confirmed by figure 4.2, which shows that more phosphate ions and Na^+ ions crossed over through the BPM for the 2019 BPM. Subfigure 4.2a shows only the phosphate cross-over and not the glycine and tricine cross-over, since for the 2018 experiments the ion cross-over for glycine and tricine was not measured. The co-ion permeation and absolute ion cross-over graphs for the average Na^+ cross-over, with standard deviation for both glycine and tricine can be found in appendix E.

[1] The phosphate buffer is used twice, for it has a pK_a value at 2 and 7. Therefore phosphate is mentioned as $phosphate_2$ and $phosphate_7$.

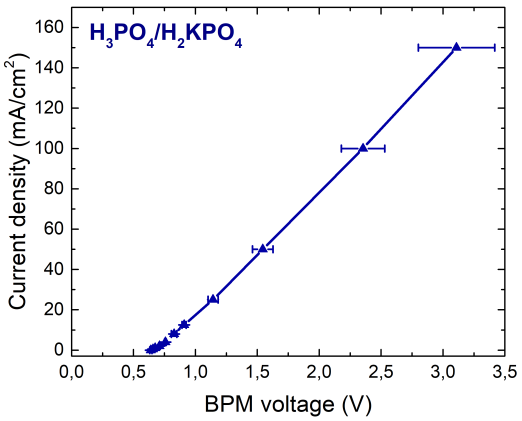

(a) Graph displaying an I-V curve for a current density range of 0 - 150 mA/cm^2 versus the BPM voltage (V). The catholyte is a 0.5M phosphate$_2$ buffer and the anolyte is a 0.5M NaOH buffer. All current density measurements (45 minutes) were performed in triplicate and the standard deviation of these results is indicated by an error bar.

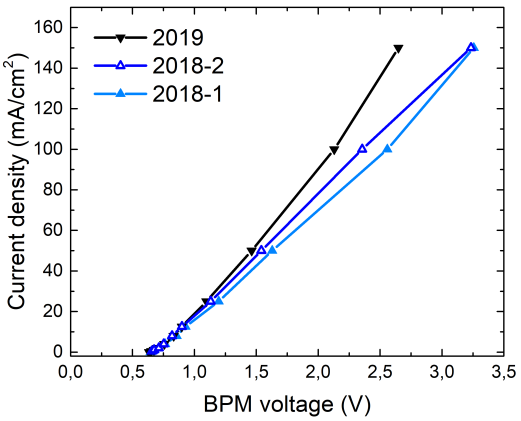

(b) Graph displaying an I-V curve for a current density range of 0 - 150 mA/cm^2 versus the BPM voltage (V). The catholyte is a 0.5M phosphate$_2$ buffer and the anolyte is a 0.5M NaOH buffer. The light blue line is the first experiment performed in 2018, the dark blue line the second in 2018 and the black line is an experiment performed in 2019.

Figure 4.1: I-V curves for 0.5M phosphate$_2$ in the catholyte and 0.5M NaOH in the anolyte.

The error margin for the BPM voltage for all phosphate$_2$ experiments is reasonable, indicating that the age of the BPM influences the BPM voltage only slightly. The I-V curves with error margin for glycine and tricine can be found in appendix E. All I-V curves show an increased error for higher current densities, which is fair since higher current densities create more gas bubbles (form noise in your measurement), which affect the average measured potential. Additionally, differences in the set-up, for instance the age of the BPM, have a larger impact on the BPM voltage for higher current densities.

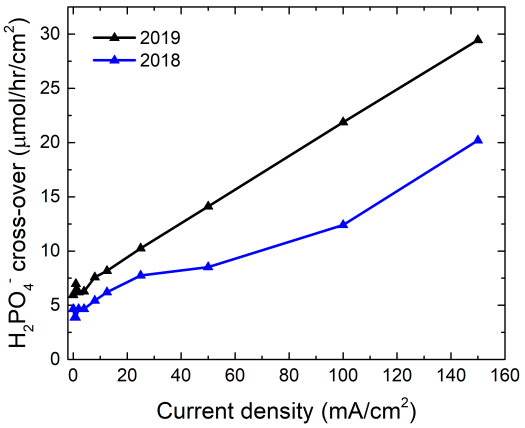

(a) Graph displaying the $H_2PO_4^-$ cross-over (µmol/hr/cm^2) from catholyte to the anolyte versus the current density (mA/cm^2) for a BPM in 2018 (blue line) and 2019 (black line).

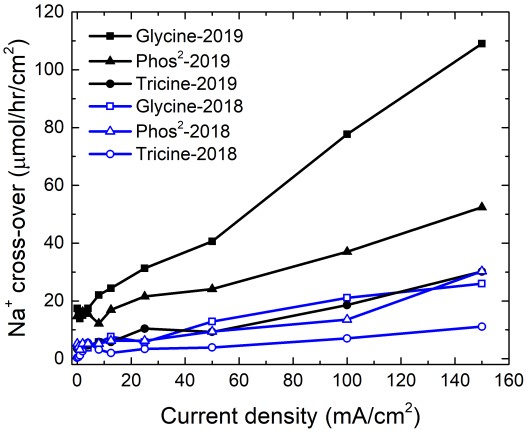

(b) Graph displaying the Na^+ cross-over (µmol/hr/cm^2) from the anolyte to the catholyte versus the current density (mA/cm^2) for a BPM in 2018 (blue lines) and 2019 (black lines) for glycine, phosphate$_2$ and tricine.

Figure 4.2: Graphs displaying the effect of the age of the BPM on ion cross-over.

Co-ion cross-over appears to be strongly influenced by the age of the membrane. Figure 4.2 indicates that cross-over of ions increases significantly for an older membrane. Particularly, Na^+ ions cross-over is 2-5 times larger than the 2018 BPM experiments for glycine, phosphate$_2$ and tricine, even though the sequence between the catholytes remains intact. Vermaas *et al.* proved that the Fumasep BPM used in this thesis indeed has a

higher selectivity towards cations than anions, thus explaining the relatively higher ion cross-over of Na^+ ions [3]. In addition, Na^+ has a smaller stokes radius than $H_2PO_4^-$, 1.84 Å and 2.56 Å, respectively [3, 95]. Therefore, if the BPM is indeed more permeable with time, smaller and more mobile ions (*e.g,* Na^+) travel through the membrane with less resistance, thus the increase in ion cross-over is relatively larger for smaller ions. The state and age of the BPM has to be taken into account when analysing results. The next sections discuss the results for the different pK_a groups.

4.2. pKa 2: glycine, tricine and phosphate

This section discusses the results for the pK_a 2 group (glycine, tricine and phosphate$_2$). I-V curves and co-ion permeation graphs are shown instead of the error margin and reproducibility graphs, which are found in the previous section. The remaining pK_a groups are discussed similarly in the following sections.

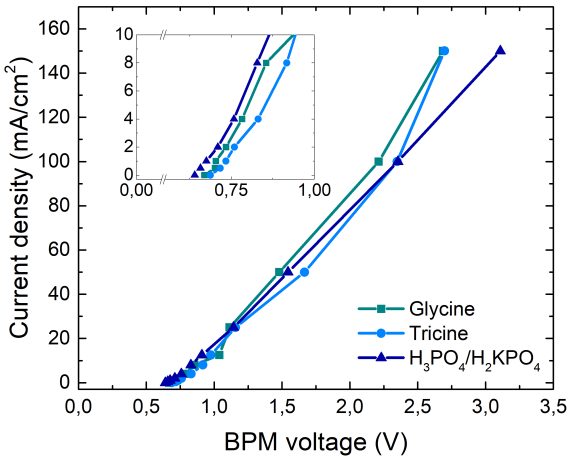

Figure 4.3: I-V curve for a current density range of 0 - 150 mA/cm^2 versus the BPM voltage (V). The catholytes are 0.5M glycine, tricine and phosphate$_2$ and the anolyte is a 0.5M NaOH buffer. The data points in the I-V curve are the average data of the 2018/2019 experiments for the three catholytes. The inset displays the lower current density region (0 - 10 mA/cm^2). The I-V curves are corrected for iR losses.

Figure 4.3 demonstrates the I-V curve for all catholytes in the pK_a 2 group. The I-V curves have a similar trend for all three catholytes and from 0 mA/cm^2, the results show a voltage close to the theoretical BPM voltage value of 0.69 V (ΔpH × 0.0591), for this specific pH difference [3, 58, 61]. Glycine shows a slightly lower BPM potential than phosphate and tricine, which can be be related to an increase in ion cross-over. Figure 4.4 indeed confirms this.

The applied electrical field during experiments causes the cathode to exert a negative charge (-) and the anode a positive one (+). Thus it is expected that cations are transported towards the cathode and anions towards the anode [45]. For higher current densities this migration force is larger, and an increase in ion cross-over takes place. This can be seen in subfigure 4.4c, since the absolute ion cross-over (µmol/hr/cm^2) for $H_2PO_4^-$ and Na^+ increases for higher current densities. However, this trend is not observed for glycine (subfigure 4.4a) and tricine (subfigure 4.4b). Glycine cross-over shows a downward trend for higher current densities, reaching a minimum value around 50 mA/cm^2, and tricine exhibits limited, but constant, cross-over (decreases slightly). The Na^+ cross-over does show expected behaviour for glycine and tricine, since it increases for higher current densities.

The trends for ion cross-over of glycine and tricine can be understood, due to the fact that their pK_a equilibrium reaction differs from the standard reaction for a weak acid (equation 3.1 in section 3.3.1). Glycine and tricine behave according to equation 4.1, where glycine/tricine takes up two protons, thus becoming positively charged, or giving up one proton and becoming uncharged (with one positive side and one negative side) [9].

$$H_2A^+ \rightleftharpoons H^+ + HA^{+/-} \tag{4.1}$$

This means that for low current densities there is a relatively high cross-over of glycine (and tricine), since they can be uncharged and thus diffuse through the membrane, because of a concentration gradient. Moreover, the glycine/tricine samples were modified with a small amount of 1M HBr (0.14M for glycine and 0.08M for tricine) to reach the required acidity for this specific pK_a group. The Br^- ions neutralise the cations in the catholyte, thus more molecules may be uncharged. Tricine shows a much lower diffusional cross-over, since it is a larger molecule with more than twice the molecular weight of glycine, thus it cannot penetrate the membrane as easily. Both molecules show a downward trend for higher current densities, since the electrical field does not influence the uncharged ions, but forces the positively charged ions towards the cathode and away from the BPM. At higher current densities, the WDR dominates the migration in the BPM, forcing other ions (*e.g.*, the uncharged glycine/tricine molecules) out of the exchange layers and into the electrolytes, thus lowering ion cross-over [3, 4, 71]. This demonstrates how ion cross-over can be influenced by the charge of the ion, which is further discussed in additional experiments, in section 4.7.

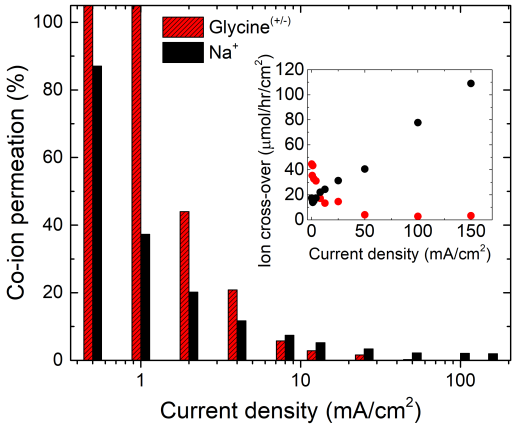

(a) Co-ion permeation (%) versus the current density. Glycine (red) crosses over from the catholyte to the anolyte and the Na^+ (black) travels from the anolyte to the catholyte. The inset shows the absolute ion cross-over for both species versus current density. The data in this graph is from the 2019 experiments.

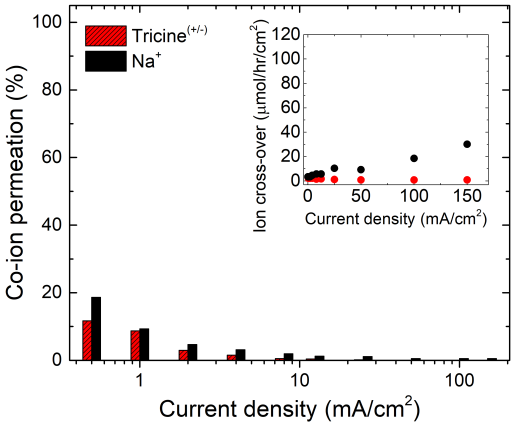

(b) Co-ion permeation (%) versus the current density. Tricine (red) crosses over from the catholyte to the anolyte and the Na^+ (black) travels from the anolyte to the catholyte. The inset shows the absolute ion cross-over for both species versus current density. The data in this graph is from the 2019 experiments.

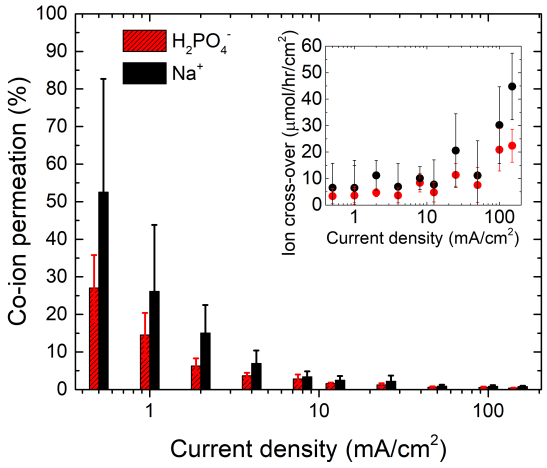

(c) Co-ion permeation (%) versus the current density. The phosphate ions (red) cross over from the catholyte to the anolyte and the Na^+ (black) travels from the anolyte to the catholyte. Phosphate is indicated as $H_2PO_4{}^-$, but can be H_3PO_4 as well. The inset shows the absolute ion cross-over for both species versus current density. The measurement for every current density is performed twice (in 2018 and 2019) and the standard deviation is indicated by the error bars.

Figure 4.4: Co-ion permeation versus current density graphs for glycine (a), tricine (b) and phosphate$_2$ (c).

The trend for co-ion permeation (%) for glycine, tricine and phosphate is as expected, namely that for low current densities the co-ion permeation is relatively large. Even though the absolute cross-over for

phosphate and Na^+ increases with higher current density, the contribution to co-ion permeation decreases. The theoretical amount of consumed H^+/OH^- is much larger for higher current densities than the observed co-ion permeation through the BPM. At higher current densities the WDR operates at >99%, which is demonstrated in figure 4.4 [3–5, 71]. For low current densities, diffusion due to a concentration gradient forces co-ions through the membrane. This diffusional cross-over is relatively large compared to the ion consumption in the electrolytes, for a low current density means low charge transportation and a low reaction rate [45]. Therefore, co-ion permeation carries the charge through the membrane and thus limits the WDR. Literature mentions 10 - 30% co-ion permeation for low current densities, which is similar to the co-ion permeation for tricine [3, 38, 40]. The phosphate and glycine results, in subfigures 4.4a and 4.4c, however, exhibit much higher co-ion permeation for low current densities, up to 100%.

4.3. pKa 7: MOPS, BES and phosphate

This section describes the results for the pK_a 7 group. For this group, experiments were performed with MOPS, BES and phosphate$_7$. Figure 4.5 demonstrates the I-V curve for the pK_a 7 catholytes. For this pH difference (pH 7 *vs.* 13.7), a current density plateau is expected, as can be seen in appendix A [3]. The plateau does seem to exist, although it lies lower, between 0 and 0.5 mA/cm^2, than literature mentions [3, 4]. This observation is further discussed in subsection 4.6.3.

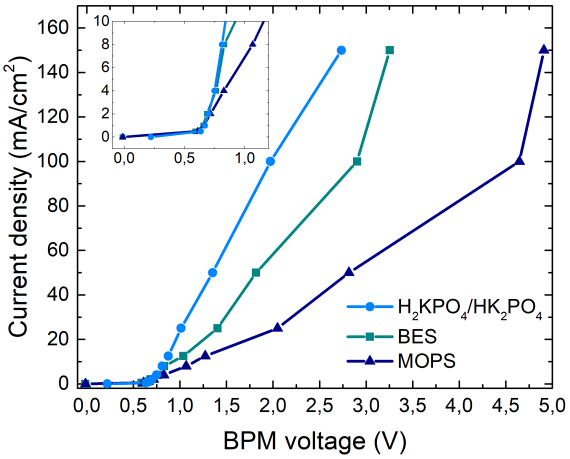

Figure 4.5: I-V curve for a current density range of 0 - 150 mA/cm^2 versus the BPM voltage (V). The catholytes are 0.5M BES, MOPS and phosphate$_7$ and the anolyte is a 0.5M NaOH buffer. The inset displays the lower current density region (0 - 10 mA/cm^2). The I-V curves are corrected for iR losses.

It is observed that BES and MOPS have a high overpotential compared to the phosphate$_7$ buffer. BES and MOPS are large molecules with a molecular weight (MW) of 213 and 209 g/mol, respectively. Therefore, a hypothesis is that these large molecules, which can form negatively charged ions, are forced towards the cation exchange layer (CEL) because of the electrical field and concentration gradient, where they create a diffusion boundary layer [3, 45]. This assumed diffusion boundary layer delays the ion transport, thus increasing the resistance at the catholyte-CEL interface, thereby increasing the overall BPM voltage. The MOPS and BES ions have a low mobility and do not simply cross over through the membrane, as can be seen from the low absolute ion cross-over at low and high current densities in subfigures 4.6a and 4.6b.

The BPM voltage for BES, however, is significantly lower than for MOPS. This is related to the Na^+ permeation, which is much higher for BES, thus carrying charge across the membrane and limiting WDR and lowering BPM potential. During the BES experiment, the BPM experienced leakage issues (the values at which this leakage occurred are not represented in subfigure 4.6a), leading to a remarkable increase in Na^+ permeation. After discovering the leakage, the membrane was replaced. However, a relatively high Na^+ cross-over remained. Section 4.1 mentioned that the state of the BPM plays a significant role in co-ion permeation, especially for Na^+, since this is a small, highly mobile cation. The ion cross-over for BES is nearly equal to MOPS, thus it is assumed that the state of the BPM may have influenced the Na^+ cross-over.

Another interesting observation is the low absolute ion cross-over for phosphate$_7$, at low current densities. Phosphate has three pK_a values (2.148, 7.198 and 12.35), and for each pK_a value the ratio of formation of ions is different, as explained in section 3.3.1. Phosphate at pH 7 is either $H_2PO_4^-$ or HPO_4^{2-}, both negatively charged, while at pH 2 phosphate is H_3PO_4 or $H_2PO_4^-$ [9]. This causes a significant difference at low current densities for phosphate$_7$, since theoretically both ion formations cannot penetrate the cation exchange layer, while H_3PO_4 for phosphate$_2$ is uncharged and can permeate the membrane easily. Additionally, 2- is repelled stronger from the cation exchange layer than 1-, thus decreasing the degree of cross-over. Diffusion due to a concentration gradient has nearly no impact on the ion cross-over for phosphate$_7$, as is demonstrated in subfigure 4.6c. At higher current densities the migration force affects the ion cross-over, and more ion permeation occurs. The negatively charged ions are forced towards the positively charged anode (+) and permeate the CEL. However, it is assumed that even at higher current densities the HPO_4^{2-} ions experience less cross-over compared to the $H_2PO_4^-$ ions, due to their charge difference and a larger stokes radius (2.56 Å and 3.23 Å, respectively) [3, 95].

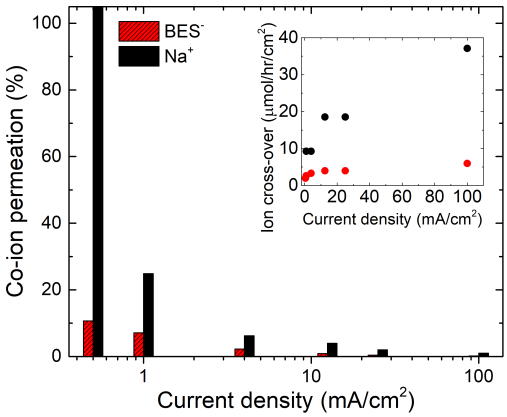

(a) Co-ion permeation (%) versus the current density for BES (red) and Na^+ ions (black). The inset shows the absolute ion cross-over for both species versus current density. The values for 0, 2, 8 and 50 mA/cm^2 have been left out of the graph, due to membrane leakage issues.

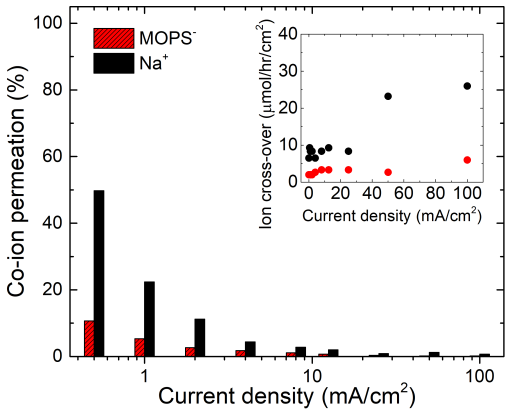

(b) Co-ion permeation (%) versus the current density for MOPS (red) and Na^+ ions (black). The inset shows the absolute ion cross-over for both species versus current density.

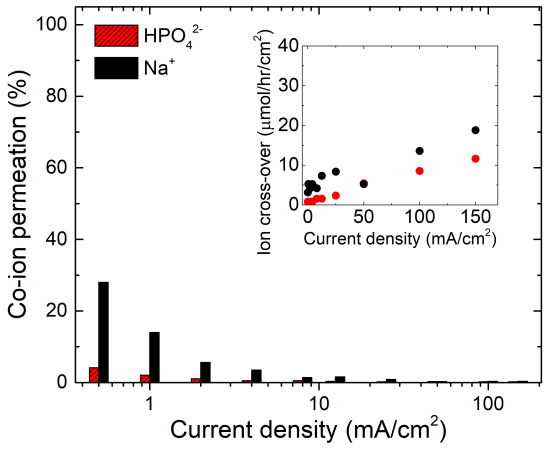

(c) Co-ion permeation (%) versus the current density for phosphate ions (red) and Na^+ ions (black). Phosphate is indicated as HPO_4^{2-}, but can be $H_2PO_4^-$ as well. The inset shows the absolute ion cross-over for both species versus current density.

Figure 4.6: Co-ion permeation versus current density graphs for BES (a), MOPS (b) and phosphate (c).

4.4. pKa 9: AMPSO and boric acid

This section describes the results for the pK_a 9 group. For this group, experiments were done with AMPSO and boric acid (H_3BO_3). Figure 4.7 provides the I-V curve, that demonstrates a high overpotential for both AMPSO and boric acid at higher current densities. Boric acid shows peculiar behaviour, since it has a higher overpotential at higher current densities than AMPSO, but a lower BPM potential in the low current density region. AMPSO is a large molecule (227 g/mol) and demonstrates similar trends as the other large molecules (BES and MOPS in section 4.3), with a high BPM potential for high current densities and nearly no absolute ion cross-over, as is shown in subfigure 4.8b.

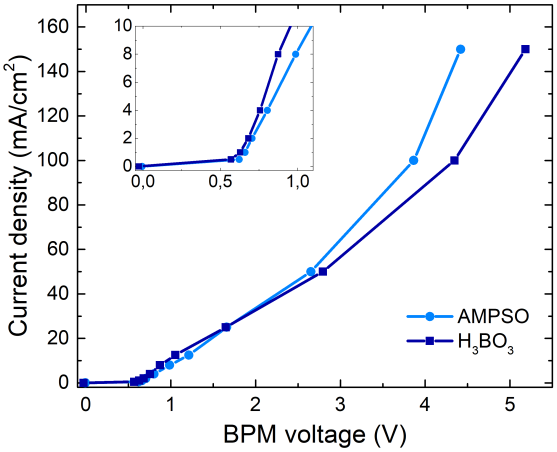

Figure 4.7: I-V curve for a current density range of 0 - 150 mA/cm^2 versus the BPM voltage (V). The catholytes are 0.5M H_3BO_3 and AMPSO and the anolyte is a 0.5M NaOH buffer. The inset displays the lower current density region (0 - 10 mA/cm^2). The I-V curves are corrected for iR losses.

Subfigure 4.8a demonstrates similar trends in the absolute boric acid cross-over as were observed in the I-V curve for boric acid. There is a nearly exponential increase in boric acid cross-over in the low current density region, up to 20 mA/cm^2. After which, it stabilizes and follows the expected trend for anions at higher current densities, namely a moderate linear increase. The relative lower BPM potential compared to AMPSO, in the low current density region, is justified by the high ion cross-over at low current densities.

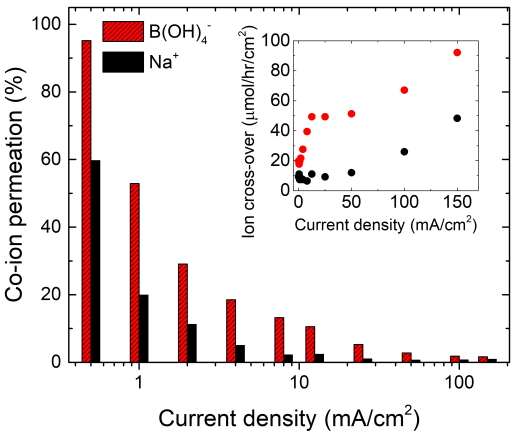

(a) Co-ion permeation (%) versus the current density for $B(OH)_4^-$ ions (red) and Na^+ ions (black). The inset shows the absolute ion cross-over for both species versus current density.

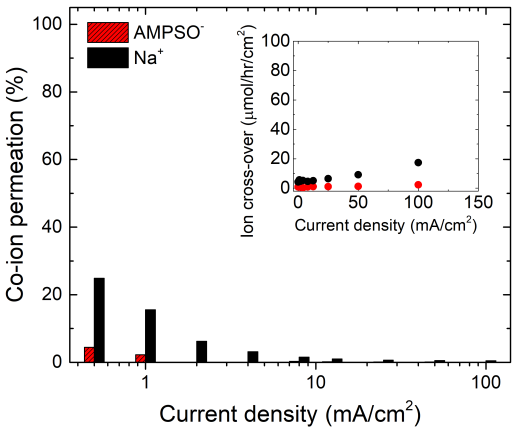

(b) Co-ion permeation (%) versus the current density for AMPSO (red) and Na^+ ions (black). The inset shows the absolute ion cross-over for both species versus current density.

Figure 4.8: Co-ion permeation versus current density graphs for boric acid (a) and AMPSO (b).

Boric acid actually differs from the typical 'weak acids', as it reacts differently in water. It does not donate a

proton, but takes an OH^- from a water molecule instead, leaving a proton behind (equation 4.2). Therefore, some conclude that the acidity of boric acid is exclusively due to the abstraction of OH^- from water [96–98]. Uncharged boric acid has a stokes radius of only 1.55 Å. This is even smaller than Na^+, which has a stokes radius of 1.84 Å, and a hydrated radius of 3.58 Å [95, 99, 100]. Thus, giving an explanation for the high boric acid cross-over, which is even higher than Na^+ for all current densities.

$$B(OH)_3 + H_2O \rightleftharpoons B(OH)_4{}^- + H^+ \tag{4.2}$$

The high diffusional cross-over for boric acid can be related to the small stokes radius, since the uncharged molecule can permeate the membrane relatively effortlessly [99]. The negatively charged $B(OH)_4{}^-$ might be repelled by the CEL at 0 mA/cm^2, yet as soon as the current density is increased in the low current density region, the ion cross-over increases exponentially. Thus implying that the small migration force from the electrical field is enough to force the small $B(OH)_4{}^-$ ions through the membrane into the anolyte. However, at higher current densities (20 - 150 mA/cm^2), the boric acid cross-over appears to follow the same trend as the Na^+ ions. At higher current densities the WDR determines the mass transfer within the membrane, thus the boric acid cross-over is possibly attenuated by the migration of the H^+ to the catholyte [3, 72]. Since the migration force increases with higher current density, the ion cross-over for boric acid still increases moderately, but not as sharp as in the low current density region.

4.5. pKa 10: CAPS and carbonate

This section describes the results for the pK_a 10 group. Experiments were performed with CAPS and carbonate ($KHCO_3$). Figure 4.9 gives the I-V curve for CAPS and carbonate. CAPS (221 g/mol) demonstrates large molecule behaviour (*e.g.*, MOPS, BES and AMPSO), since the I-V curve shows a high overpotential at high current densities. Subfigure 4.10b confirms this, since the ion cross-over for CAPS is low. The experiments for 100 and 150 mA/cm^2 were stopped by the potentiostat, for the total cell voltage exceeded the maximum applicable voltage of the potentiostat.

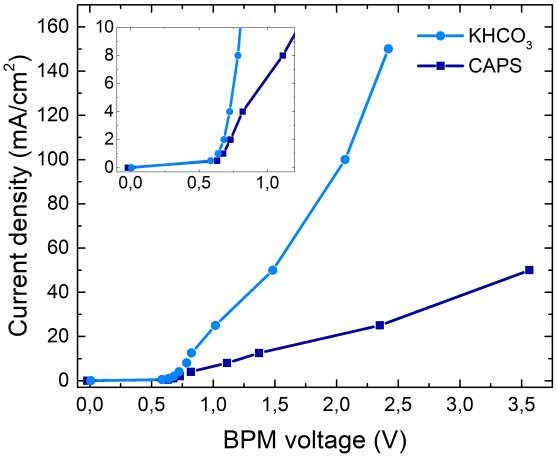

Figure 4.9: I-V curve for a current density range of 0 - 150 mA/cm^2 versus the BPM voltage (V). The catholytes are 0.5M $KHCO_3$ and CAPS and the anolyte is a 0.5M NaOH buffer. The inset displays the lower current density region (0 - 10 mA/cm^2). The CAPS data stops after a current density of 50 mA/cm^2, as the maximum applicable voltage of the potentiostat was exceeded at higher current densities. The I-V curves are corrected for iR losses.

Carbonate demonstrates typical small ion behaviour. The BPM voltage remains relatively low for high current densities, which must be a result of ion cross-over. Unfortunately, the ICP-OES results only present the K^+ cross-over, which does not provide any information on the cross-over of $HCO_3{}^-$ and $CO_3{}^{2-}$. The thermodynamic radii of $HCO_3{}^-$ and $CO_3{}^{2-}$ are 1.56 Å and 1.78 Å, respectively, thus it is assumed that cross-over is relatively high [101, 102]. This, in combination with the high Na^+ cross-over, explains the low BPM voltage. A potassium ion has a small stokes radius of 1.34 Å, thus high ion cross-over is expected [3, 103]. However, the K^+ ions are present in the catholyte, therefore they are forced towards the cathode as

soon as an electric field is applied. Negligible K^+ cross-over takes place for all current densities, as is demonstrated in subfigure 4.10a. At open circuit (0 mA/cm^2), cross-over increases slightly due to the concentration gradient over the BPM, yet K^+ is positively charged and therefore repelled by the anion exchange layer at the anolyte side of the electrochemical set-up. The cross-over of potassium ions is observed for all buffer solutions that have been modified with 1M KOH (appendix C). Nonetheless, the K^+ cross-over is extremely low in all cases and is therefore negligible.

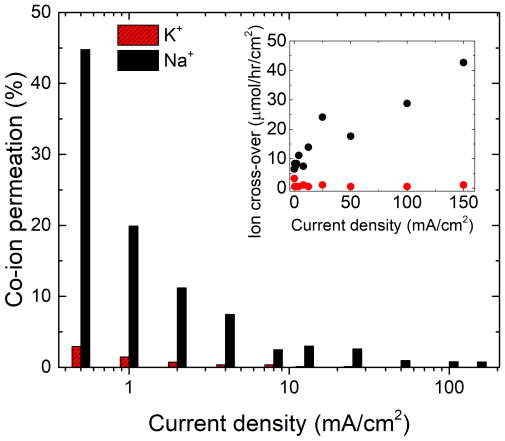

(a) Co-ion permeation (%) versus the current density for carbonate and Na^+. The CO_3^{2-} or HCO_3^- ions were not measured, therefore only the K^+ (red) cross over from the catholyte to the anolyte is given. The inset shows the absolute ion cross-over for both species versus current density.

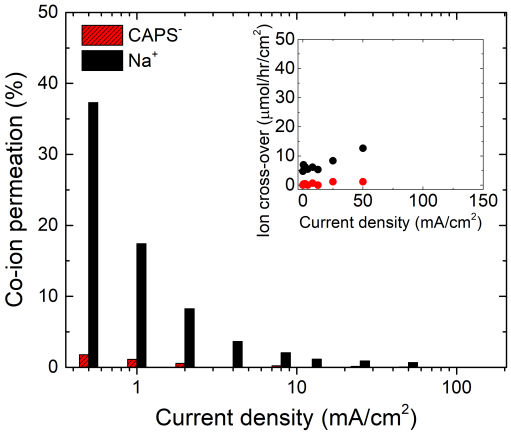

(b) Co-ion permeation (%) versus the current density for CAPS (red) and Na^+ ions (black). The inset shows the absolute ion cross-over for both species versus current density.

Figure 4.10: Co-ion permeation versus current density graphs for $KHCO_3$ (a) and CAPS (b).

4.6. Similarities and particularities for all pKa groups

Sections 4.2-4.5 describe the results for all pK_a groups. Subsequently, this section continues on the similarities and particularities that were observed for all results. This section is an important aspect of the thesis, since trends that can be observed for all data are relevant for the aim of this thesis and may be relevant for future work.

There are a few subjects that are applicable for all pK_a groups and appear interesting for further investigation. An aim of this thesis is to observe the effect of ion size on ion cross-over. This section begins with that subject, in subsection 4.6.1. Thereupon, the Na^+ cross-over is investigated in subsection 4.6.2. This cross-over has been measured for all catholytes, therefore it is critical to get a better understanding on the matter. Finally, the BPM voltage and the pH changes are discussed in subsection 4.6.3 and 4.6.4.

4.6.1. Ion cross-over versus molecular weight (MW)

Figure 4.11 displays the absolute ion cross-over against the molecular weight of all catholyte species for different current densities. A clear observation is that the ion cross-over for large molecules (>150 g/mol) is low at open circuit (0 mA/cm^2), and remains low for higher current densities. The radius of these ions is too large to permeate the membrane, therefore ion cross-over remains nearly constant for all current densities. Furthermore, it can be observed that glycine (the lightest measured molecule), experiences the most ion cross-over at open circuit, due to its size, but especially its valence (uncharged and positively charged) [9]. The positively charged glycine ions permeate the cation exchange layer, which increases the probability that it diffuses through the anion exchange layer, since there is a concentration gradient at that side of the BPM. It is assumed that the uncharged ion can permeate the membrane with ease since it is small, and because of the high measured ion cross-over at 0 mA/cm^2. For higher current densities the glycine ions are forced towards the cathode (by migration) or pushed out of the BPM by the WDR, therefore the glycine cross-over

drops steadily when the current density is increased. The same trend is observed for tricine, only the initial cross-over at open circuit is much lower, since it is more than two times the size of glycine.

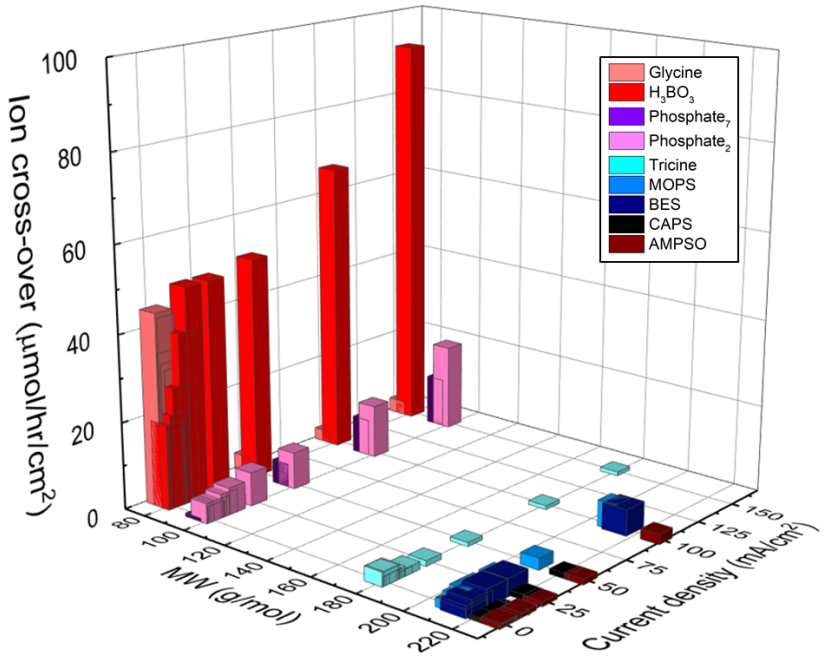

Figure 4.11: 3D graph demonstrating the absolute ion cross-over (µmol/hr/cm^2) versus the MW (g/mol) and the current density (mA/cm^2). The carbonate data is not present in the graph, since only potassium cross-over was measured. The glycine/tricine results are from 2019.

Boric acid (H_3BO_3), also merely small, shows a significant increase in ion cross-over for higher current densities. The electric field forces the negatively charged $B(OH)_4^-$ ions towards the anode, thus ion cross-over increases for higher current densities. However, the relative increase in ion cross-over is much steeper between 0 and 25 mA/cm^2 than between 25 and 100 mA/cm^2, as observed in section 4.4. This is related to the WDR that dominates migrations fluxes in the BPM at high current densities [3, 4, 71, 72].

Both phosphate buffers ($phosphate_2$ and $phosphate_7$), show similar behaviour for ion cross-over. $phosphate_7$ demonstrates negligible cross-over at open circuit since both ion formations are negatively charged, as mentioned in section 4.3, thus diffusion is limited. The ion cross-over for both phosphate buffers increases for higher current densities. It can be observed in figure 4.11, that the increase due to migration fluxes is lower than for the smaller molecules (<80 g/mol), but higher than the larger molecules (>150 g/mol).

Vermaas *et al.* already observed this effect, as given in figure 4.12 [3]. This figure displays that the co-ion permeation percentage drops for ions with a larger stokes radius. $H_2PO_4^-$ already shows a low co-ion permeation of around 2% for a phosphate buffer at 10 mA/cm^2. Ions that are bigger (in MW or ion radius) are expected to permeate even less, as proven in figure 4.11. However, for these large molecules a high overpotential was measured, as is observed in subfigure 4.13. Therefore, it is hypothesized that there is a ideal region, somewhere between 100 - 200 g/mol, in which the absolute ion cross-over remains low due to the size of the molecule, yet the BPM voltage does not increase due to a possible diffusion boundary layer of large molecules. This theory is of course dependent on the chosen BPM, since the density of the membrane influences the location of this ideal region.

Another theory for low cross-over for large molecules is membrane inhibition. It is assumed, that molecules can become embedded in the membrane layers, therefore inhibiting any mass transport through the BPM. Minor ion cross-over still occurs for large molecules, thus membrane inhibition is possible[2]. However, the current density range experiments were performed randomly, for every current density. Consequently, if

[2]If large molecules cannot permeate the membrane, due to their size, no ion cross-over occurs. Therefore, vastly large ions cannot immobilize in the membrane layers. If ion cross-over is observed, then membrane inhibition is a possibility.

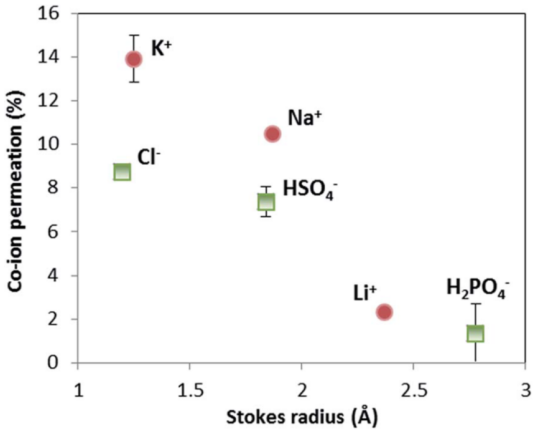

Figure 4.12: Co-ion permeation as a function of hydrated radius of ions. Data were obtained from 16 hour measurements at 10 mA/cm^2. From source [3].

membrane inhibition occurs, it would affect the results of the next experiments. Unexpected values for different current densities are not observed, therefore it is assumed that membrane inhibition does not have a significant effect on the ion cross-over. On the contrary, membrane inhibition may only affect the ion cross-over when an electrical field is applied, since the migration force pushes the large ions into the cation exchange layer. As soon as the applied electrical field is terminated, the large ions may migrate back into the catholyte. If this holds true, it may affect the opposing Na^+ cross-over, which is further discussed in the next section.

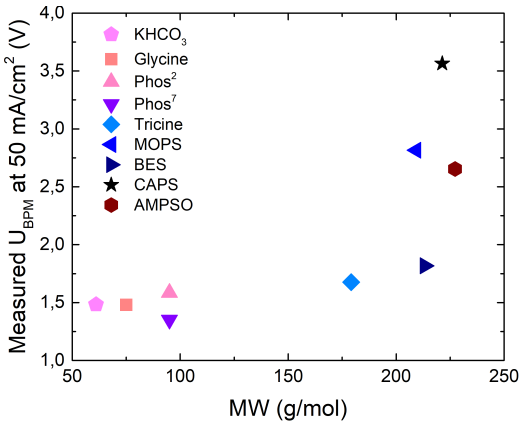

Figure 4.13: Voltage of BPM as a function of the molecular weight of the tested catholytes at 50 mA/cm^2. This specific current density is chosen, for certain large molecules did not provide any data for higher current densities. Boric acid is excluded from the graph, for its high overpotential is not understood and does not follow the expected trend.

4.6.2. Na+ cross-over for all catholytes

The previous section describes the effect of ion size and molecular weight on ion cross-over for all catholytes. However, in the anolyte a 0.5M NaOH solution was utilized for all experiments. This subsection describes the Na^+ cross-over for all catholytes and which factors influence this opposing ion cross-over.

Figure 4.14 presents the Na^+ cross-over for all catholytes at different current densities. It is assumed that the catholyte ion size and the trends that can be related to this ion size, as explained in the previous section, influence the Na^+ cross-over. Therefore, this section describes the opposing fluxes through the BPM. These fluxes must not be seen as actual flows of solution from one electrolyte to another, since the absolute ion cross-over is still significantly low for all catholytes at all current densities. Therefore, these fluxes do not oppose each other as forces of motion, but more as forces of charge imbalances. Furthermore, it is assumed that the flux from the catholyte to the anolyte may influence the opposing ion cross-over flow, due to

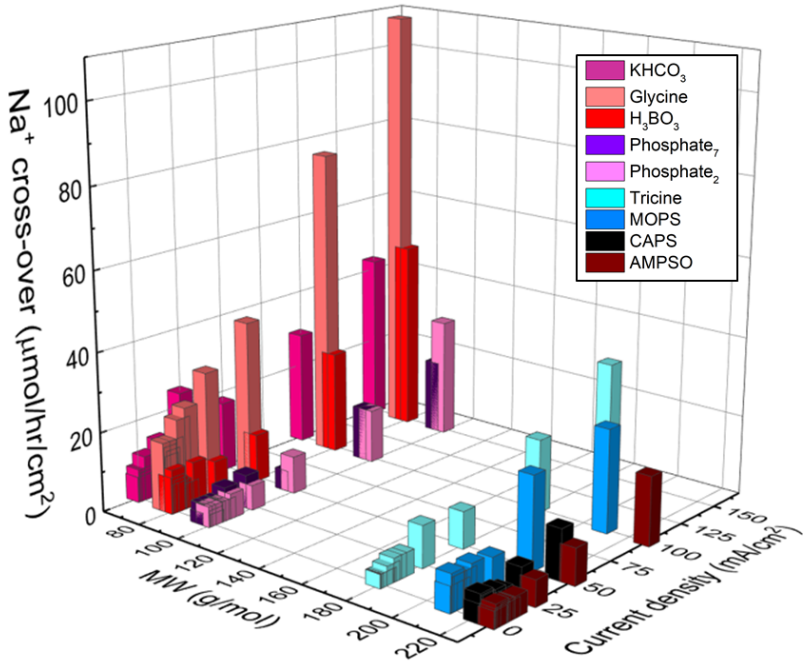

Figure 4.14: 3D graph demonstrating the absolute Na^+ cross-over (µmol/hr/cm^2) versus the MW (g/mol) of the catholyte ions and the current density (mA/cm^2). BES is excluded from the graph for its Na^+ cross-over results were unreliable. The glycine/tricine Na^+ cross-over results are from 2019.

membrane inhibition. It is not fully understood how these opposing flows influence each other, yet the results do indicate that a mutual effect is present, as is further described in this section.

Catholyte molecules with a low molecular weight (50-80 g/mol) permeate the membrane relatively easy, thus causing a diffusion flux towards the anolyte. It appears that for low current densities this flux reduces the Na^+ flow towards the catholyte. Glycine molecules, as shown in subsection 4.6.1, show high cross-over at open circuit (due to diffusion), while the opposing Na^+ flow is around 20 µmol/hr/cm^2. As soon as the glycine cross-over drops at higher current densities, as explained in the previous section, the Na^+ increases to 30 and 80 µmol/hr/cm^2 for 25 and 100 mA/cm^2, respectively. Boric acid, on the other hand, experiences an exponential increase in ion cross-over from 0 to 25 mA/cm^2, however, the Na^+ permeation remains constant at 10 µmol/hr/cm^2, while an increasing current density should increase Na^+ cross-over. This also indicates that the Na^+ flow is actually reduced by a high catholyte ion counter flow. As soon as the boric acid cross-over attenuates at higher current densities, as described in section 4.4, the Na^+ flow increases towards 30 µmol/hr/cm^2 at 100 mA/cm^2 (subfigure 4.14).

When comparing the phosphate buffers to the larger molecules (tricine, MOPS and AMPSO), the compensating behaviour of Na^+ cross-over is observed as well. Phosphate$_2$ and phosphate$_7$ experience slightly more cross-over at higher current densities than the large molecules (>150 g/mol). This balances the opposing Na^+ cross-over, as is confirmed in subfigure 4.14, where the Na^+ cross-over is indeed lower for the phosphate buffers compared to tricine, MOPS and AMPSO. However, in the previous subsection it is observed that the large molecules (>150 g/mol) experience negligible cross-over (even at high current densities), thus an even higher counter Na^+ flow is expected. This trend is not observed, and therefore it is assumed that the diffusion boundary layer created by the large molecules at the catholyte-CEL interface, moderately decreases the Na^+ cross-over towards the catholyte. It is hypothesized that this diffusion boundary layer blocks the transport of Na^+ into the catholyte, thus increasing the Na^+ concentration in the interface layer and CEL. This might reduce the Na^+ concentration gradient between the interface layer and the anolyte, thus reducing the ion cross-over from the anolyte, through the AEL, into the interface layer and CEL. A more obvious explanation is that the large molecules inhibit the membrane, therefore lowering the opposing Na^+ cross-over. It is assumed that the degree of membrane inhibition increases for higher current densities, since the large negatively charged ions are forced more vigorously into the cation exchange layer. Membrane inhibition blocks any mass transfer, therefore attenuating the opposing Na^+ flux for higher

current densities. This phenomena has not been observed between experiments, therefore it is only a possibility, if the large molecules migrate out of the cation exchange layer and back into the catholyte as soon as the electrical field is down. If the molecules remain immobilized within the membrane layers, it would effect the results of the next performed experiment, which has not been observed in this project.

Moussaoui *et al.* observed that Na^+ cross-over levels at a limiting value, with increased applied potential ΔV [72]. However, the results in this paper were obtained with a equal NaCl solution on both sides of the BPM. Therefore, the formed concentration gradient, as a result of Na^+ cross-over, opposes the migration force, which leads to this limiting value. In the results of this thesis, large molecules increase the BPM potential significantly, therefore it may be that the lower Na^+ cross-over is related to the increased BPM voltage, due to the assumed large molecule diffusion boundary layer. However, in this research the concentration gradient remains large for Na^+, as the absolute sodium cross-over during an experiment is insignificant compared to the concentration gradient. Thus, this theory cannot hold true for this thesis [72].

Another theory for Na^+ cross-over is that a higher BPM voltage actually increases the permeation of Na^+ ions towards the catholyte. Migration is caused by a potential gradient. This potential gradient (from the cathode to the anode) forces cations towards the cathode and anions towards the anode [45]. Consequently, the BPM has a potential gradient from the CEL to the AEL, where the AEL has has a more positive potential than the CEL. Thus, cations are drawn to the CEL and anions are drawn to the AEL. If the potential gradient over the BPM increases, the migration force for cations to the CEL and anions to the AEL increases as well. Therefore, a higher BPM potential can, theoretically, increase the Na^+ permeation from the AEL towards the CEL.

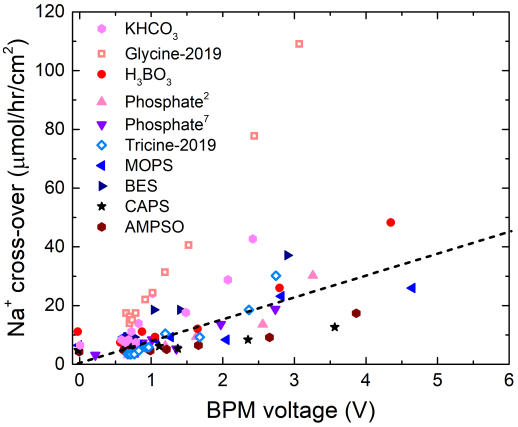

(a) Na^+ cross-over as a function of BPM voltage for all catholytes, including glycine-2019, tricine-2019 and BES.

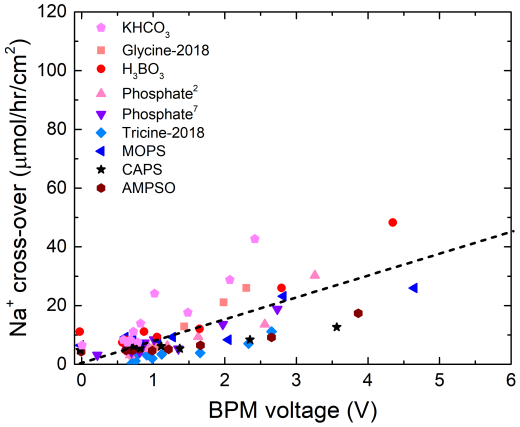

(b) Na^+ cross-over as a function of BPM voltage for all catholytes, including glycine-2018 and tricine-2018. BES is excluded from this graph for its Na^+ cross-over results were unreliable.

Figure 4.15: Na^+ cross-over as a function of BPM voltage, uncorrected (a) and corrected (b).

Subfigure 4.15a presents the BPM voltage versus Na^+ cross-over for all experimentally tested catholytes. All results so far include the 2019 tricine and glycine measurements, since the relation between cation and anion cross-over is discussed, and both the glycine/tricine cross-over and the opposing Na^+ cross-over were only measured for the 2019 experiment, as explained in section 4.1. However, as is demonstrated in subfigure 4.15a, the Na^+ cross-over for glycine and tricine is much higher than expected, due to the state of the BPM, and does not fall in line with the other results. Subfigure 4.15b gives the Na^+ cross-over results for all experiments that were performed with the first BPM batch, including glycine-2018 and tricine-2018. BES is excluded from the the second graph, since BPM leakage occurred during the experiment. The difference between the two graphs in figure 4.15, once more proves the influence of the state of the BPM on ion cross-over.

To verify if a high BPM voltage increases the Na^+ permeation, the sodium cross-over has been plotted against the BPM voltage and the current density in figure 4.16. The BPM voltage increases with higher current density, since the resistance theoretically remains constant and E=I·R [45]. Furthermore, a higher current density increases the ion cross-over for cations and anions in opposing directions, as is proven in all results thus far.

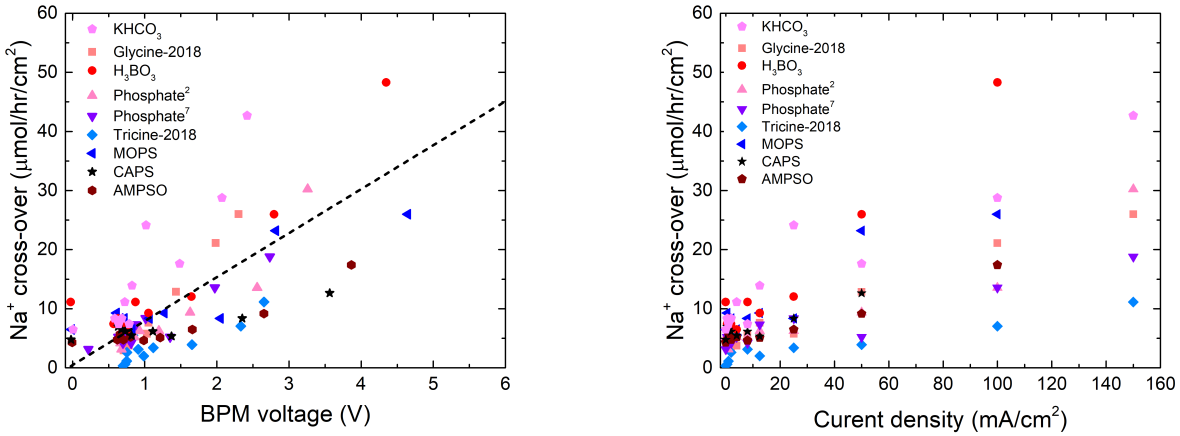

(a) (b)

Figure 4.16: Na^+ cross-over as a function of BPM voltage (a) and as a function of current density (b).

Therefore, to confirm that the BPM voltage has an additional effect on ion cross-over, and not only due to the relationship with current density, the data points around the trend line in subfigure 4.16a, should be more densely packed than the data points in subfigure 4.16b. It appears as if subfigure 4.16a shows a linear trend with the data points spread on both sides of the hypothetical trend line. The current density graph (4.16a) demonstrates this trend as well, but the data points lie further apart compared to data plotted against the BPM voltage. This could indicate that the Na^+ cross-over is indeed influenced by the BPM voltage. However, figure 4.16 demonstrates another interesting trend. It is noticed that in both graphs the lower region is dominated by the larger catholyte molecules, while the upper region is dominated by the smaller catholyte molecules. Again, this indicates that Na^+ cross-over is actually limited by larger molecules, as mentioned previously.

4.6.3. Measured BPM voltage versus theoretical values

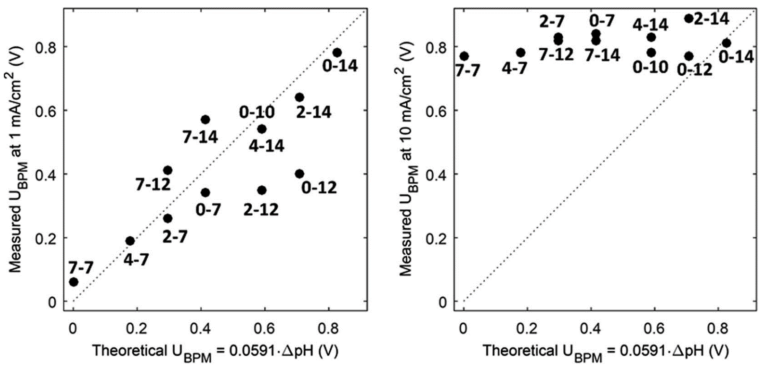

Figure 4.17: Measured potential versus thermodynamic membrane potential U_{BPM}=0.0591·ΔpH for 12 cases, for a current density of 1 mA/cm^2 and 10 mA/cm^2. Every case has a different pH difference, which is mentioned for every data point. From source: [3].

Chapter 2 introduces the typical I-V curve for a BPM, with a current density plateau, as is given in figure 2.6 in section 2.4.3. Figure 4.17 demonstrates how the BPM voltage changes for specific pH differences for a low current density (1 mA/cm^2) and higher current density (10 mA/cm^2) [3]. At the low current density the data points follow the theoretical value for the BPM voltage, while for the higher current density they increase towards the 0.82 V required for WDR [3, 4, 61, 71]. Thus, these results imply that the current density plateau appears between 1 and 10 mA/cm^2. However, during experiments in this thesis, the current density plateau has only been observed (in the 1-10 mA/cm^2 region) in rinsing curves, which were fast galvodynamic scans (150 seconds) from 0 to 150 mA/cm^2, with a scan rate of 1 mA/cm^2/s. Yet, the results in figure 4.17 were obtained by chronopotentiometric series of 300s, which is also a short time in comparison with the

45 minutes performed in this thesis for every current density point. Therefore, in the results of this project, the current density plateau can only be observed at lower current densities, between 0 and 0.5 mA/cm^2, as demonstrated in figure 4.18. Apparently, the BPM voltage reaches an equilibrium after some time, which results in a higher average BPM voltage than the voltage obtained from fast scans and short measurements.

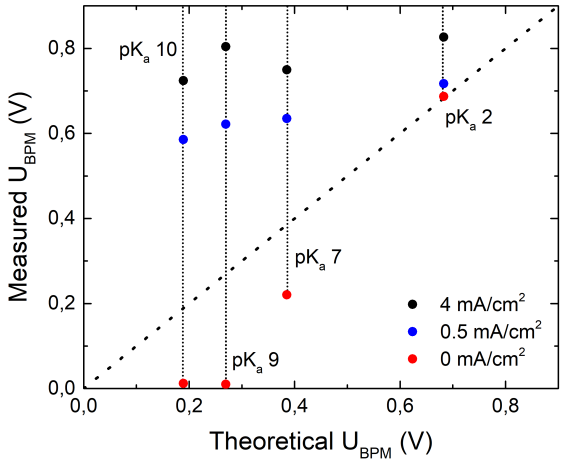

Figure 4.18: Measured potential versus thermodynamic membrane potential U_{BPM}=0.0591·ΔpH for the pK$_a$ groups in this research.

4.6.4. pH changes in experiments

Subsection 3.5.3 describes how the pH change in the catholyte during an experiment can be related to the pK$_a$ and ion cross-over. For all tested catholytes this calculation has been performed, as given in equation 4.3. This equation is similar to equation 3.16, except that the final value is defined as Z. Equation 4.3 gives the ratio between the pH meter data and the ICP-OES results. Therefore Z can be defined as a value indicating the accuracy of the correlation between ion cross-over and the pH change.

$$Z = \frac{\text{Total ion cross-over}}{\Delta[H^+] + \Delta X} \approx 1 \tag{4.3}$$

The final answer for equation 4.3 should be 1, since theoretically the total ion cross-over is equal to the sum of the change in pH and the change in the catholyte pK$_a$ ratio. Table 4.1 presents Z for the current density range of the tricine and phosphate$_7$ results. These experiments demonstrated the most reliable results for Z for all catholytes.

Table 4.1: The value Z versus current density for tricine and phosphate$_7$.

Current density (mA/cm^2)	**Tricine (Z)**	**Phosphate$_7$ (Z)**
0	-	-
0.5	1.9	-
1	5.8	5.8
2	1.2	1.6
4	1.7	3.5
8	1.1	2.1
12.5	1.2	1.8
25	1.1	0.9
50	1.1	0.7
100	0.4	0.9
150	0.3	1.2

It appears that the accuracy of the measurements is lowest in the low current density region (1 - 4 mA/cm^2). This is because of the relative high ion cross-over due to diffusion, and no explicit pH change measured by the pH meter. For some experiments the pH does not change at all, therefore no value for Z could be calculated. For higher current densities Z stays closer to one, since the absolute ion cross-over is larger and therefore the change in pH is more clearly observed. For all catholytes the answers of Z for the entire current density range stay within the same order of magnitude, therefore the results are reasonable.

4.7. Additional experiments

During this thesis, some additional experiments have been performed to investigate complications and questions that arose during initials tests. Additionally, an up-scaling experiment was done, since an initial aim for this research was the up-scaling of the electrochemical configuration.

4.7.1. Constant charge versus constant time

Most repetition experiments were performed with the phosphate$_2$ buffer, including a constant charge experiment. The results for all pK_a groups discussed in this chapter were all constant time experiments, since a specific current density was applied for 45 minutes. Therefore, the applied charge per current density differs. Thus, it was thought interesting to observe the system if the charge was kept constant for all current densities and the time changes per experiment.

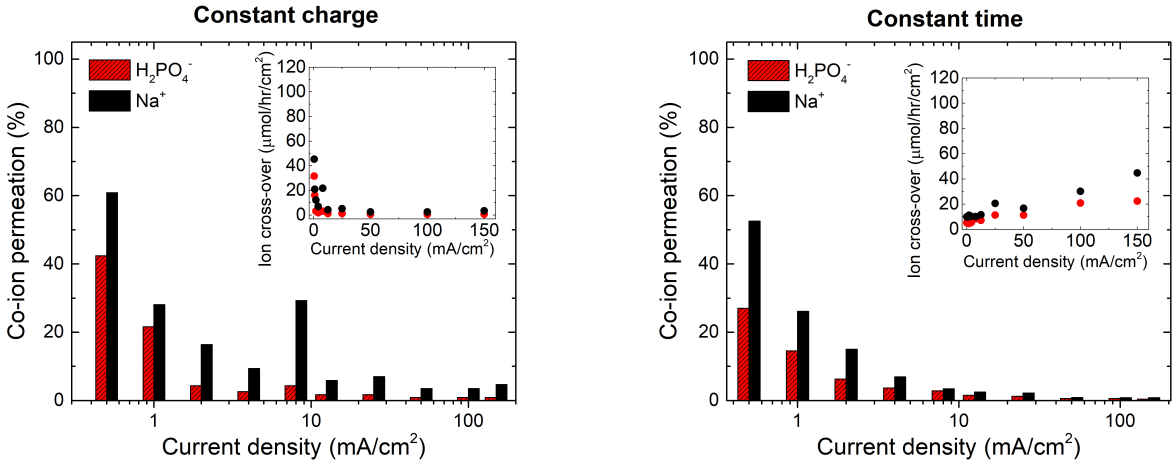

(a) (b)

Figure 4.19: Co-ion permeation (%) versus the current density for constant charge (a) and constant time (b). The phosphate ions (red) cross over from the catholyte to the anolyte and the Na^+ (black) travels from the anolyte to the catholyte. The insets show the absolute ion cross-over for both species versus current density. The experiments for 2mA/cm^2 are equal for constant charge and constant time (45 minutes), which show similar results.

The constant charge results demonstrate high ion cross-over at low current densities, after which it decreases rapidly and remains close to zero for higher current densities. This is not expected, since the same charge was applied for every experiment, thus the cross-over should be equal for all experiments. However, in the low current density region the performed experiments were much longer. For 0.5 mA/cm^2 it takes 180 minutes to achieve the same charge as 54 seconds for 100 mA/cm^2. This indicates that most ion cross-over, in the lower current density region, is diffusion related.

4.7.2. Valence of ions

Buffers were used for all experiments. The buffer capacity of these solutions prevents large pH changes in the bulk of the catholyte, which may occur due to ion cross-over. Therefore, a current density experiment was performed with a 0.5M K_2SO_4 solution as the catholyte, at 4, 12.5 and 50 mA/cm^2 (figure 4.20). If ion cross-over occurs, it is visible as a pH change. This change was indeed visible for these experiments, since

the pH would increase rapidly from pH 9 to pH 12, after an experiment was started. This might appear as a significant pH change, but the change in $\Delta[H^+]$ is relatively small compared to the amount of measured cross-over, thus reasonable. The relationship between pH/pK_a and ion cross-over was calculated, as explained in the previous subsection. However, the final outcome was not exactly 1 (but the same order of magnitude), since the pH meter has an error which, especially at low current densities, increases the total error.

Another interesting results is the relatively low ion cross-over of sulfate. SO_4^{2-} has a stokes radius of 2.58 Å [101, 102]. This stokes radius is similar to that of $H_2PO_4^-$ (2.56 Å), however the results in table 4.2 indicate that the sulfate cross-over is lower than both phosphate buffers [3, 95]. This low cross-over is a consequence of the valence of SO_4^{2-}, since it is strongly repelled from the cation exchange layer. Section 4.6.2 hypothesizes that a correlation between the catholyte ion cross-over and the opposing Na^+ cross-over exists. Table 4.3 appears to confirm this assumption, since an increase in sodium cross-over is observed for lower catholytic cross-over.

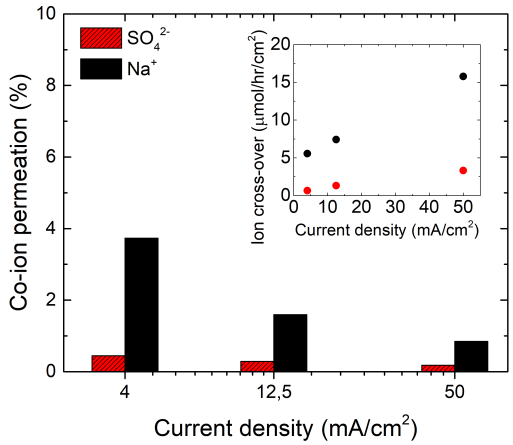

(a) Co-ion permeation (%) versus 4, 12.5 and 50 mA/cm^2. The sulfate ions (red) cross over from the catholyte to the anolyte and the Na^+ (black) travels from the anolyte to the catholyte. The inset shows the absolute ion cross-over for both species versus current density.

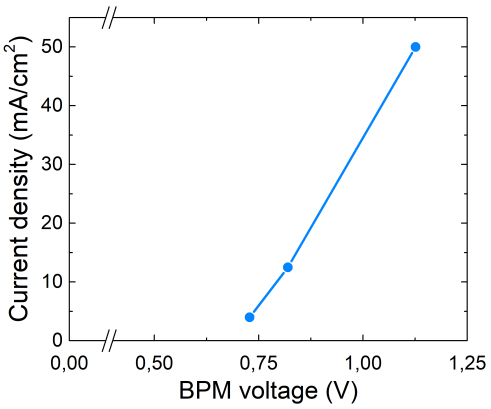

(b) I-V curve for 4, 12.5 and 50 mA/cm^2 versus the BPM voltage (V). The catholyte is 0.5M K_2SO_4 and the anolyte is a 0.5M NaOH buffer. The curve is corrected for conductivity with a specific conductivity for K_2SO_4, $\kappa_{(K_2SO_4)}$ = 72 mS/cm [93].

Figure 4.20: I-V curve (a) and ion permeation graph (b) for 0.5M K_2SO_4 experiments.

Table 4.2: Ion cross-over versus current density for the phosphate buffers and sulfate. Phosphate$_2$ is $H_3PO_4/H_2PO_4^-$ and phosphate$_7$ is $H_2PO_4^-/HPO_4^{2-}$.

Current density	**4 mA/cm^2**	**12.5 mA/cm^2**	**50 mA/cm^2**
Phosphate$_2$ cross-over (µmol/hr/cm^2)	4.6	6.2	8.5
Phosphate$_7$ cross-over (µmol/hr/cm^2)	0.8	1.5	5.4
SO_4^{2-} cross-over (µmol/hr/cm^2)	0.7	1.3	3.3

Table 4.3: Na^+ cross-over versus current density for the phosphate buffers and sulfate. The value for Na^+ cross-over for phosphate$_7$ at 50 mA/cm^2 is theoretical, since its true value did not lie within the trend confirmed by the phosphate$_7$ ICP-OES results.

Current density	**4 mA/cm^2**	**12.5 mA/cm^2**	**50 mA/cm^2**
Phosphate$_2$: Na^+ cross-over (µmol/hr/cm^2)	5.2	6.3	9.4
Phosphate$_7$: Na^+ cross-over (µmol/hr/cm^2)	5.2	7.3	11.0
SO_4^{2-}: Na^+ cross-over (µmol/hr/cm^2)	5.6	7.4	15.8

4.7.3. Up-scaling of the BPM surface area

Chapter 3 mentions that a scaled-up configuration is used for experiments, with a BPM surface area of 100 cm^2, instead of 10 cm^2. The results for this set-up are presented in this subsection. Figure 4.21 gives the I-V curve for $Phosphate_7$ with a BPM surface area of 10 cm^2 and 100 cm^2. $phosphate_7$ was chosen for this experiment, since it demonstrated the least amount of cross-over and overpotential with the 10 cm^2 BPM surface area from all tested catholytes (at that point in the project).

The I-V curve demonstrates that the larger BPM surface area has a lower BPM voltage. This indicates that more ion cross-over occurs in the 100 cm^2 set-up, which is indeed confirmed by figure 4.22. However, this does not necessarily reflect the used configuration. For this experiment, a customized BPM sheet was used, that had been stored for over 2 years. As given in section 4.1, the state of the membrane has a large impact on ion cross-over, especially the cross-over of Na^+. It is given in subfigure 4.22a that the Na^+ cross-over is already high at open circuit (due to diffusion), and remains high at higher current densities. The phosphate cross-over shows a similar trend compared to the 10 cm^2 set-up, but is slightly higher as well.

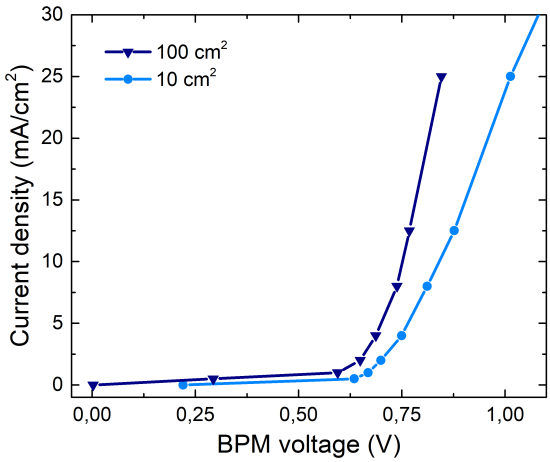

Figure 4.21: I-V curve for a current density range of 0 - 25 mA/cm^2 versus the BPM voltage (V), with a BPM surface area of 10 and 100 cm^2. The catholyte is 0.5M $phosphate_7$ and the anolyte is a 0.5M NaOH buffer.

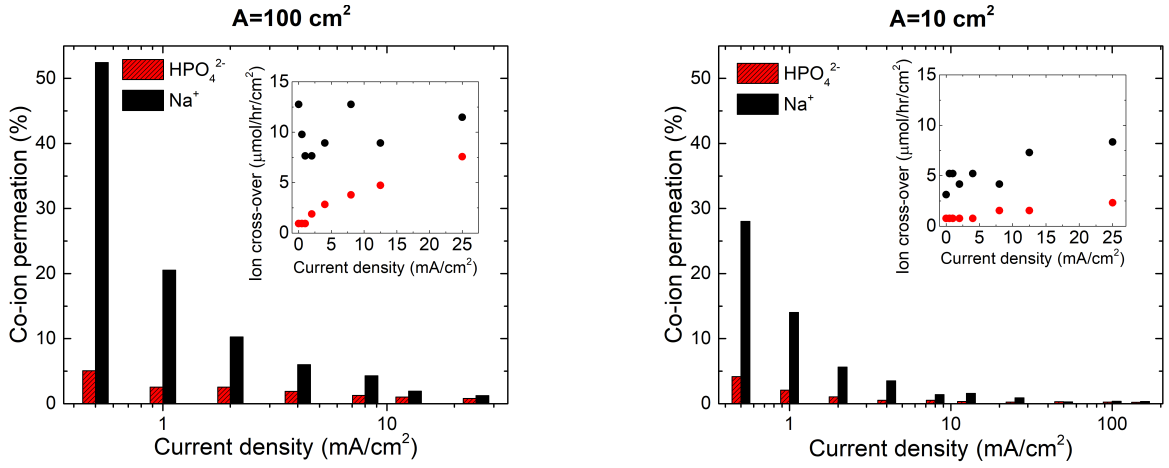

(a) (b)

Figure 4.22: Co-ion permeation (%) versus the current density for a 100 cm^2 (a) and a 10 cm^2 (b) BPM surface area. The phosphate ions (red) cross over from the catholyte to the anolyte and the Na^+ (black) travels from the anolyte to the catholyte. The insets show the absolute ion cross-over for both species versus current density.

4.8. Summary

Ion cross-over for all pK$_a$ groups

This chapter describes the ion cross-over through a BPM for all pK$_a$ groups. All 0.5M catholytes were tested with an opposing 0.5M NaOH anolyte. A summary of the results is given in this section. Chapter 5 continues with the discussion and conclusion of these results.

pK$_a$ 2: glycine, tricine and phosphate$_2$
The I-V curves for all pK$_a$ 2 experiments are similar and start at the theoretical BPM potential value for this specific electrolyte pH difference. The absolute ion cross-over for glycine and tricine decreases with higher current densities, since their ions are positively charged or uncharged, therefore unaffected by the increased migration force for anions towards the anode. The phosphate ions do follow the expected trend, as ion cross-over increases with higher current densities.

pK$_a$ 7: MOPS, BES and phosphate$_7$
The I-V curves for MOPS and BES demonstrate higher BPM potentials for higher current densities compared to the phosphate$_7$ I-V curve. It is assumed that large molecules create a diffusion boundary layer, thus increasing the BPM potential. Phosphate$_7$ experiences less cross-over compared to phosphate$_2$ (pK$_a$ group 2), for all its ions are negatively charged and cannot permeate the cation exchange layer.

pK$_a$ 9: boric acid and AMPSO
Boric acid and AMPSO have a similar I-V curve. This is unexpected since boric acid demonstrates high ion cross-over, which theoretically lowers the BPM potential. AMPSO is a large molecule, therefore a high BPM voltage with negligible ion cross-over is expected and confirmed.

pK$_a$ 10: carbonate and CAPS
Unfortunately, the cross-over for the carbonate ions has not been measured. However, the BPM potential is significantly lower for carbonate than for CAPS, therefore relatively high ion cross-over is expected. CAPS (large molecule) demonstrates similar behaviour as AMPSO, MOPS and BES.

Molecular weight versus ion cross-over
Negligible catholytic ion cross-over is observed for large molecules, while boric acid and glycine (<100 g/mol) exhibit relatively high co-ion permeation. Furthermore, it appears that the opposing Na^+ cross-over is influenced by the catholyte ions.

All catholytes demonstrate negligible co-ion permeation at high current densities. Furthermore, diffusion dominates ion cross-over at low current densities, therefore co-ion permeation is larger in this region. Additionally, it has been observed that the state of the membrane has a significant influence on the degree of ion cross-over and that the valence of an ion significantly influences its ion permeation.

5

Discussion & Conclusion

In this thesis, multiple catholytes with different ionic characteristics were tested in an electrochemical configuration with a BPM. The experiments were performed for a current density range of 0-150 mA/cm^2, with different pH values, according to the pK_a value of the catholytic solution. Chapter 4 presents the obtained experimental data of this research, thereupon this chapter continues on the final discussion and conclusion of these results. The main research question for this thesis is, as stated in chapter 1: **How do ion characteristics influence ion cross-over through a bipolar membrane (BPM)?**

This main question is answered with these supporting research questions:

- *How does ion size affect the degree of co-ion permeation?*
- *Does the ion type affect the opposing ion cross-over flux?*
- *How does ion valence influence the degree of co-ion permeation?*
- *What is the relation between ion cross-over and the electrochemical response of the BPM?*

First, these supporting research questions are discussed, after which the main research question is answered.

To observe the effect of ion size, the ionic solutions varied in molecular weight (MW) between 50 and 250 g/mol. It has been proven that the ion size and the stokes radius have a direct effect on ion cross-over through a BPM, since larger molecules (>100 g/mol) demonstrate significantly lower cross-over compared to smaller (<100 g/mol) ions [3]. There are a few factors that have to be taken into account when discussing ion size. The MW of an ion might not be the strongest indication, since ions of similar weight can differ in stokes radius. However, literature has already observed that ions with a stokes radius larger than 2.5 Å show negligible co-ion permeation (<1 %) at high current densities [3]. Phosphate ($H_2PO_4^-$, 97 g/mol) is such an ion, thus significantly larger molecules are expected to have an even larger ionic (or stokes) radius and therefore follow the trend described by literature [3]. In addition, this effect is observed in the experiments performed for this thesis, since large molecules (>100 g/mol) show negligible cross-over for all current densities, as is described in section 4.6.1.

In the anolyte, a constant 0.5M NaOH solution was used for all experiments while altering the catholyte type. The second supporting research question relates to the anolyte, as the Na^+ cross-over is analysed. Na^+ permeation appears to be influenced by multiple factors, such as the state of the membrane, the membrane potential and the opposing catholyte ion. Moussaoui *et al.* proved that the current efficiency of water dissociation in the bipolar membrane generally is predominantly affected by cationic leakage occurring through the anion exchange layer (AEL), because of its lower permselectivity [72]. This trend has been observed in multiple papers, and is confirmed throughout this thesis as well [3, 72]. The Na^+ cross-over is always larger than the opposing cross-over for the catholyte ions, due to its small stokes radius. Except for boric acid, which has an even smaller stokes radius than Na^+ [9, 99, 100]. The high sodium ion cross-over is not only related to its small stokes radius. Vermaas *et al.* already demonstrated that anions with the same stokes radius show less cross-over, due to the lower permselectivity of the AEL [3, 72, 95]. Consequently, this confirms why the state of the membrane has such a significant effect on the Na^+ cross-over. Section 4.1

indicates that the Na^+ cross-over is 2-5 times higher for an older membrane compared to the relative smaller increase in cross-over for the catholyte anions. Furthermore, sodium permeation depends on the opposing anion flux. A higher ion cross-over flux from the catholyte to the anolyte decreases the opposing Na^+ flow and vice versa, as given in section 4.6.2. For large molecules that show negligible cross-over, the opposing sodium flux reaches a limiting value, since the absolute Na^+ cross-over is quite similar for all large catholytic molecules. It is assumed that the Na^+ flow attenuates for higher current densities in combination with large molecules on the other side of the membrane. This behaviour is, either related to membrane inhibition of the cation exchange layer by large molecules, or is related to the increased BPM potential due to a diffusion boundary layer formed by these large molecules. It is not understood which effect is stronger, however it does confirm that the catholyte ion size influences the opposing Na^+ cross-over.

The third supporting research question is related to the valence of an ion and the influence this has on the cross-over of ions through the BPM. The results given in section 4.7.2 indicate that a higher ratio of 2- ions in the catholyte solution decreases the overall cross-over. Therefore, it appears that a higher valence, decreases the ion cross-over. This has already been assumed in literature, but has not been proven yet [3]. It seems that the increased repellent force between the cation exchange layer and the 2- ion, outweighs the increased migration effect on the ion. This effect of ion valence has also been observed for glycine and tricine, which form uncharged or positively charged ions in the catholyte solutions. Glycine and tricine demonstrate low cross-over for high current densities, because the positively charged ions are pushed towards the cathode and thus away from the BPM. Neutral ions, however, can easily permeate through the membrane, but at higher current densities the water dissociation reaction dominates the mass transfer in the BPM, forcing the uncharged ions out of the BPM [3, 4, 71].

The fourth supporting research question relates to co-ion permeation as a function of the electrochemical response of the BPM, which according to literature, influences each other [3, 4, 71]. It is known that ion cross-over can lower the BPM voltage, since a part of the current is carried by the co-ions [3]. This trend has been observed in the performed experiments, since an increase in ion cross-over, in relatively similar conditions, proves to lower the BPM voltage. This is demonstrated in section 4.1, where the state of the BPM is discussed. An older BPM shows a lower permselectivity, allowing more ion cross-over and thus lowering the BPM voltage. Furthermore, the results indicate that when molecules reach a certain size, the BPM voltage increases significantly. It is assumed that this is related to a diffusion boundary layer that is formed by the large molecules. Consequently, it is hypothesized that there is an ideal region for the size of an ion, where the ion cross-over can be limited to a negligible amount, but the BPM voltage does not increase greatly yet.

The effect of ion cross-over on the pH, and therefore the stability of the system has been observed during this thesis. The pH remains relatively constant for all tested catholytes, and no significant pH changes have been seen. The calculations, as described in section 3.5.3, did not achieve the expected value for the relationship between the pH, pK_a and ion cross-over. At low current densities the diffusion related mass transfer was significant, thus increasing the ratio of the final answer in equation 3.16. Additionally, the accuracy of the pH meter has a large effect on the error, which together with the error of the ICP-OES results for ion cross-over, further decreases the accuracy of the calculated value. However, the final answers for all tested catholytes were in the expected order of magnitude.

As an answer to the main research question, it is clear that the ion characteristics have an important effect on the ion cross-over through a bipolar membrane. The ion size and valence greatly influence the degree of cross-over, which therefore influences the BPM potential. An interesting observed side effect is that the opposing cation flux from the anolyte to the catholyte is indirectly linked to the chosen catholyte ion type. Furthermore, the co-ion permeation at high current densities is low for all tested catholytes, thus ideal for industrial high performance applications. If the ion size for both electrolytes is chosen cleverly, the total ion cross-over through the BPM can be reduced significantly, therefore increasing the overall stability in the long run. It is observed in the up-scaling experiment, that a larger set-up demonstrates the expected BPM behaviour and that a similar trend for co-ion permeation remains. Thus, future research can continue with up-scaling the process by utilising the results presented in this thesis.

6

Recommendations

The results from this thesis are promising for understanding the behaviour of the bipolar membrane (BPM) in an electrochemical cell. The obtained knowledge on ion cross-over can be an interesting starting point for further improvements on the electrochemical configuration. Building towards an industrial application is essential, however, more research is required. Therefore, this chapter discusses unanswered questions for this thesis and provides recommendations for further research.

First, the state of the BPM has an enormous effect on ion cross-over. Therefore the BPM should be tested for stability and quality for a longer period of time. Consequently, literature mentions that the permselectivity of the anion exchange layer of commercial bipolar membranes is lower than the cation exchange layer [3, 72]. Therefore, it might be interesting to test multiple commercial bipolar membranes to observe if this effect is indeed true for all manufactured bipolar membranes. If so, the permselectivity of the anion exchange layer (AEL) should be increased. A large segment of ion cross-over through the BPM comes from the cation flux from the anolyte to the catholyte, through the AEL, which effects the stability of the system. Additionally, membrane inhibition can be an issue. During this research all current density experiments were performed randomly, therefore, if membrane inhibition would occur, it should have been seen in the results. However, the degree of inhibition may be quite small and was not noticed during experiments. Membrane inhibition decreases the efficiency of the WDR and reduces the stability of the system and must be investigated.

Second, the choice of electrolytes can significantly decrease the degree of co-ion permeation. The catholytes have been tested in this research, however, the Na^+ ions from the anolyte demonstrate most cross-over. Therefore, a similar alkaline solution (stabilizes the oxygen revolution reaction) can be used [3, 48]. For instance, a LiOH solution, since Li^+ has a larger stokes radius than Na^+ and this lowers ion cross-over [3]. For the catholyte it appears that there is an ideal ion size region, in which the ion cross-over is negligible and the BPM overpotential remains reasonable. Therefore, if a clever combination of catholyte and anolyte solutions are chosen, the ion cross-over could be extremely low, while the BPM overpotential remains practical. This could increase the stability and the energy efficiency of the system. Literature proved that the total cell voltage can be lowered with a BPM configuration [19]. Therefore, more research on favorable electrolytes and electrodes to further decrease this potential can be done, while observing the total cell potential. Future research must focus on implementing the knowledge on ion cross-over in an up-scaled configuration while measuring the overpotential, selectivity and stability.

An up-scaled configuration is utilized during this project. However, in this set-up high current densities (>25 mA/cm^2) could not be reached. Therefore, an experiment should be performed with the correct equipment and set-up, to achieve high current densities for a larger BPM surface area. The electrochemical response of the BPM must be observed to ensure that the results are similar to the high current density small-scale experiments that have been preformed in this thesis.

In these experiments most buffers were modified with an acid or base to reach the pH=pK_a value. The effect of these modifications on ion cross-over has not been studied. Therefore, only buffer solutions that reach their pK_a value without modifications (*e.g.*, phosphate buffers) should be used in experiments, or the effect of these modifications must be further investigated. Additionally, the results for boric acid and BES were

unexpected. Boric acid experienced a high overpotential and high ion cross-over. No explanation for this behaviour could be found, therefore this experiment must be repeated to be certain that this overpotential was not related to flaws in the electrochemical set-up (*e.g.*, BPM leakage/inhibition, electrolyte leakage, potentiostat issues and/or contamination). BES demonstrated high opposing Na^+ cross-over, which could indicate that there were issues with the BPM, as explained previously. The experiment can be repeated to check if these results were indeed BPM related. In the experiment for carbonate the catholyte ion cross-over has not been measured (not possible with ICP-OES/NMR). It is assumed due to the low overpotential and the small stokes radius of the carbonate ions, that high ion cross-over occurs. However, the experiment should be re-done and the carbonate ion cross-over must be measured with a different analytical measurement technique, to ensure that this is indeed the case.

A BPM configuration is applicable for electrochemical CO_2 reduction and water splitting [3, 19, 39]. The research field is continuously improving the stability, selectivity, energy efficiency and performance rate of convenient systems for these electrochemical reactions. This research proves that the chosen electrolytes can influence the degree of ion cross-over, therefore a proper selection of these electrolytes can lead to a stable, high energy efficient system. Consequently, the main recommendation is to implement this knowledge in an electrochemical reduction set-up and to observe the further required improvements necessary for an industrially relevant application.

Bibliography

[1] BP Statistical Review of World Energy. BP Statistical Review of World Energy 2018. Technical report, 2018.

[2] M A van Oorschot. System configurations for stable electrochemical CO2 reduction to CO. Technical report, TU Delft, 2019.

[3] David A Vermaas, Sandra Wiegman, Tetsuro Nagaki, and Wilson A Smith. Ion transport mechanisms in bipolar membranes for (photo)electrochemical water splitting. *Sustainable Energy & Fuels*, 2(9): 2006–2015, 2018. doi: 10.1039/C8SE00118A. URL http://dx.doi.org/10.1039/C8SE00118A.

[4] Amir M. Ashrafi, Nupur Gupta, and David Neděla. An investigation through the validation of the electrochemical methods used for bipolar membranes characterization. *Journal of Membrane Science*, 2017. ISSN 18733123. doi: 10.1016/j.memsci.2017.09.026.

[5] FuelCellStore. Fumasep FBM, 1999. URL https://www.fuelcellstore.com/fuel-cell-components/membranes/fumatech-membranes/fumasep-fbm.

[6] Princeton Applied Research. PARSTAT MC Potentiostat. URL https://www.ameteksi.com/products/potentiostats/multichannel/parstat-mc.

[7] Solartron Analytical. EnergyLab XM Potentiostat Galvanostat. URL https://www.ameteksi.com/products/potentiostats/single-channel/apps-xm-series/energylab-xm.

[8] ElectroCell. Electrochemical Flow Cells, 2017. URL https://www.electrocell.com/media/1220/all-ec-cells_technical-data.pdf.

[9] Robert N. Goldberg, Nand Kishore, and Rebecca M. Lennen. Thermodynamic quantities for the ionization reactions of buffers, 2002. ISSN 00472689.

[10] Hannah Ritchie and Max Roser. CO2 and other Greenhouse Gas Emissions. *OurWorldInData.org*, 2015. ISSN 00099163. doi: 10.1034/j.1399-0004.2002.610606.x.

[11] IPCC. *Climate Change 2014: Impacts, Adaptation, and Vulnerability. Summaries, Frequently Asked Questions, and Cross-Chapter Boxes.* 2014. ISBN 9789291691418. doi: 10.1016/j.renene.2009.11.012.

[12] IPCC. IPCC Special Report 1.5 - Summary for Policymakers. In *Global warming of 1.5°C. An IPCC Special Report on the impacts of global warming of 1.5°C above pre-industrial levels and related global greenhouse gas emission pathways, in the context of strengthening the global response to the threat of climate change,*. 2018. ISBN 9789291691432. doi: 10.1017/CBO9781107415324.

[13] European Commission. A Clean Planet for all - A European long-term strategic vision for a prosperous , modern , competitive and climate neutral economy. Technical report, 2018.

[14] Colin P. Morice, John J. Kennedy, Nick A. Rayner, and Phil D. Jones. Quantifying uncertainties in global and regional temperature change using an ensemble of observational estimates: The HadCRUT4 data set. *Journal of Geophysical Research Atmospheres*, 2012. ISSN 01480227. doi: 10.1029/2011JD017187.

[15] T.A. Boden, G. Marland, and R.J. Andres. Global, Regional, and National Fossil-Fuel CO2 Emissions, 2016.

[16] Max Roser. Future Population Growth. *Global Environmental Change*, 2017. doi: 10.1016/j.gloenvcha.2014.06.004.

[17] Hannah Ritchie and Max Rose. Energy Production & Changing Energy Sources. *Our World in Data*, 2019.

[18] F. M. Mulder. Implications of diurnal and seasonal variations in renewable energy generation for large scale energy storage. *Journal of Renewable and Sustainable Energy*, 2014. ISSN 19417012. doi: 10.1063/1.4874845.

[19] David A. Vermaas and Wilson A. Smith. Synergistic Electrochemical CO2Reduction and Water Oxidation with a Bipolar Membrane. *ACS Energy Letters*, 2016. ISSN 23808195. doi: 10.1021/acsenergylett.6b00557.

[20] Charles J. Barnhart and Sally M. Benson. On the importance of reducing the energetic and material demands of electrical energy storage. *Energy and Environmental Science*, 2013. ISSN 17545706. doi: 10.1039/c3ee24040a.

[21] Grigorii L. Soloveichik. Battery Technologies for Large-Scale Stationary Energy Storage. *Annual Review of Chemical and Biomolecular Engineering*, 2011. ISSN 1947-5438. doi: 10.1146/annurev-chembioeng-061010-114116.

[22] Fernando J. de Sisternes, Jesse D. Jenkins, and Audun Botterud. The value of energy storage in decarbonizing the electricity sector. *Applied Energy*, 2016. ISSN 03062619. doi: 10.1016/j.apenergy.2016.05.014.

[23] Devin T. Whipple and Paul J.A. Kenis. Prospects of CO2 utilization via direct heterogeneous electrochemical reduction. *Journal of Physical Chemistry Letters*, 2010. ISSN 19487185. doi: 10.1021/jz1012627.

[24] Edward J. Maginn. What to do with CO 2, 2010. ISSN 19487185.

[25] Mark E. Dry. The Fischer-Tropsch process: 1950-2000. In *Catalysis Today*, 2002. doi: 10.1016/S0920-5861(01)00453-9.

[26] Sumit Verma, Xun Lu, Sichao Ma, Richard I. Masel, and Paul J.A. Kenis. The effect of electrolyte composition on the electroreduction of CO2 to CO on Ag based gas diffusion electrodes. *Physical Chemistry Chemical Physics*, 2016. ISSN 14639076. doi: 10.1039/c5cp05665a.

[27] Y. Hori. Electrochemical CO2 Reduction on Metal Electrodes. In *Modern Aspects of Electrochemistry*. 2008. ISBN 978-0-387-49488-3. doi: 10.1007/978-0-387-49489-0{_}3.

[28] Huei Ru Molly Jhong, Sichao Ma, and Paul Ja Kenis. Electrochemical conversion of CO2 to useful chemicals: Current status, remaining challenges, and future opportunities, 2013. ISSN 22113398.

[29] Marcel Schreier, Laura Curvat, Fabrizio Giordano, Ludmilla Steier, Antonio Abate, Shaik M. Zakeeruddin, Jingshan Luo, Matthew T. Mayer, and Michael Grätzel. Efficient photosynthesis of carbon monoxide from CO<inf>2</inf> using perovskite photovoltaics. *Nature Communications*, 2015. ISSN 20411723. doi: 10.1038/ncomms8326.

[30] Tooru Inoue, Akira Fujishima, Satoshi Konishi, and Kenichi Honda. Photoelectrocatalytic reduction of carbon dioxide in aqueous suspensions of semiconductor powders [3], 1979. ISSN 00280836.

[31] Joan M Ogden. PROSPECTS FOR BUILDING A HYDROGEN ENERGY INFRASTRUCTURE. *Annual Review of Energy & the Environment*, 1999. ISSN 1056-3466. doi: 10.1146/annurev.energy.24.1.227.

[32] Philippe Jeanty, Christian Scherer, Erhard Magori, Kerstin Wiesner-Fleischer, Olaf Hinrichsen, and Maximilian Fleischer. Upscaling and continuous operation of electrochemical CO2 to CO conversion in aqueous solutions on silver gas diffusion electrodes. *Journal of CO2 Utilization*, 2018. ISSN 22129820. doi: 10.1016/j.jcou.2018.01.011.

[33] Meenesh R. Singh, Jason D. Goodpaster, Adam Z. Weber, Martin Head-Gordon, and Alexis T. Bell. Mechanistic insights into electrochemical reduction of CO 2 over Ag using density functional theory and transport models . *Proceedings of the National Academy of Sciences*, 2017. ISSN 0027-8424. doi: 10.1073/pnas.1713164114.

[34] Michael B. McDonald, Shane Ardo, Nathan S. Lewis, and Michael S. Freund. Use of bipolar membranes for maintaining steady-state pH gradients in membrane-supported, solar-driven water splitting. *ChemSusChem*, 2014. ISSN 1864564X. doi: 10.1002/cssc.201402288.

[35] Nella M. Vargas-Barbosa, Geoffrey M. Geise, Michael A. Hickner, and Thomas E. Mallouk. Assessing the utility of bipolar membranes for use in photoelectrochemical water-splitting cells. *ChemSusChem*, 2014. ISSN 1864564X. doi: 10.1002/cssc.201402535.

[36] Jingshan Luo, David A. Vermaas, Dongqin Bi, Anders Hagfeldt, Wilson A. Smith, and Michael Grätzel. Bipolar Membrane-Assisted Solar Water Splitting in Optimal pH. *Advanced Energy Materials*, 2016. ISSN 16146840. doi: 10.1002/aenm.201600100.

[37] Ronald S. Reiter, William White, and Shane Ardo. Communication—Electrochemical Characterization of Commercial Bipolar Membranes under Electrolyte Conditions Relevant to Solar Fuels Technologies. *Journal of The Electrochemical Society*, 2016. ISSN 0013-4651. doi: 10.1149/2.0201604jes.

[38] Ke Sun, Rui Liu, Yikai Chen, Erik Verlage, Nathan S. Lewis, and Chengxiang Xiang. Solar-Driven Water Splitting: A Stabilized, Intrinsically Safe, 10% Efficient, Solar-Driven Water-Splitting Cell Incorporating Earth-Abundant Electrocatalysts with Steady-State pH Gradients and Product Separation Enabled by a Bipolar Membrane (Adv. Energy, 2016. ISSN 16146840.

[39] S. Z. Oener, S. Ardo, and S. W. Boettcher. Ionic Processes in Water Electrolysis: The Role of Ion-Selective Membranes. *ACS Energy Letters*, 2017. ISSN 23808195. doi: 10.1021/acsenergylett.7b00764.

[40] David A. Vermaas, Mark Sassenburg, and Wilson A. Smith. Photo-assisted water splitting with bipolar membrane induced pH gradients for practical solar fuel devices. *Journal of Materials Chemistry A*, 2015. ISSN 20507496. doi: 10.1039/c5ta06315a.

[41] Xinghao Zhou, Rui Liu, Ke Sun, Yikai Chen, Erik Verlage, Sonja A. Francis, Nathan S. Lewis, and Chengxiang Xiang. Solar-Driven Reduction of 1 atm of CO2 to Formate at 10% Energy-Conversion Efficiency by Use of a TiO2-Protected III-V Tandem Photoanode in Conjunction with a Bipolar Membrane and a Pd/C Cathode. *ACS Energy Letters*, 2016. ISSN 23808195. doi: 10.1021/acsenergylett.6b00317.

[42] Sakineh Chabi, Andrew G. Wright, Steven Holdcroft, and Michael S. Freund. Transparent Bipolar Membrane for Water Splitting Applications. *ACS Applied Materials and Interfaces*, 2017. ISSN 19448252. doi: 10.1021/acsami.7b04402.

[43] Yuguang C. Li, Dekai Zhou, Zhifei Yan, Ricardo H. Gonçalves, Danielle A. Salvatore, Curtis P. Berlinguette, and Thomas E. Mallouk. Electrolysis of CO2to Syngas in Bipolar Membrane-Based Electrochemical Cells. *ACS Energy Letters*, 2016. ISSN 23808195. doi: 10.1021/acsenergylett.6b00475.

[44] Zhifei Yan, Liang Zhu, Yuguang C. Li, Ryszard J. Wycisk, Peter N. Pintauro, Michael A. Hickner, and Thomas E. Mallouk. The balance of electric field and interfacial catalysis in promoting water dissociation in bipolar membranes. *Energy and Environmental Science*, 2018. ISSN 17545706. doi: 10.1039/c8ee01192c.

[45] Allen J. Bard and Larrz R. Faulkner. *: Fundamentals and Applications*. 1980. ISBN 3175723993. doi: 10.1146/annurev.matsci.30.1.117.

[46] R. E.W. Jansson. Electrochemical reaction engineering. *Chemical Engineering Science*, 1980. ISSN 00092509. doi: 10.1016/0009-2509(80)80138-2.

[47] IUPAC. *Compendium of Chemical Terminology*. 1997. ISBN 0-9678550-9-8. doi: http://dx.doi.org/10.1351/goldbook.I03352.

[48] Charles C.L. McCrory, Suho Jung, Jonas C. Peters, and Thomas F. Jaramillo. Benchmarking heterogeneous electrocatalysts for the oxygen evolution reaction. *Journal of the American Chemical Society*, 2013. ISSN 00027863. doi: 10.1021/ja407115p.

[49] Seunghwa Lee, Hyung Kuk Ju, Revocatus Machunda, Sunghyun Uhm, Jae Kwang Lee, Hye Jin Lee, and Jaeyoung Lee. Sustainable production of formic acid by electrolytic reduction of gaseous carbon dioxide. *Journal of Materials Chemistry A*, 2015. ISSN 20507496. doi: 10.1039/c4ta03893b.

[50] Revocatus L. MacHunda, Hyungkuk Ju, and Jaeyoung Lee. Electrocatalytic reduction of CO2 gas at Sn based gas diffusion electrode. *Current Applied Physics*, 2011. ISSN 15671739. doi: 10.1016/j.cap.2011.01.003.

[51] Sumit Verma, Byoungsu Kim, Huei Ru Molly Jhong, Sichao Ma, and Paul J.A. Kenis. A gross-margin model for defining technoeconomic benchmarks in the electroreduction of CO2. *ChemSusChem*, 2016. ISSN 1864564X. doi: 10.1002/cssc.201600394.

[52] Martin M. Halmann Meyer Steinberg. Greenhouse gas carbon dioxide mitigation: science and technology. In *Greenhouse gas carbon dioxide mitigation: science and technology*. 1999. ISBN 1566702844.

[53] Brian A. Rosen, Amin Salehi-Khojin, Michael R. Thorson, Wei Zhu, Devin T. Whipple, Paul J.A. Kenis, and Richard I. Masel. Ionic liquid-mediated selective conversion of CO2 to CO at low overpotentials. *Science*, 2011. ISSN 10959203. doi: 10.1126/science.1209786.

[54] Michael R. Thorson, Karl I. Siil, and Paul J. A. Kenis. Effect of Cations on the Electrochemical Conversion of CO 2 to CO . *Journal of The Electrochemical Society*, 2012. ISSN 0013-4651. doi: 10.1149/2.052301jes.

[55] Jing Jing Lv, Matthew Jouny, Wesley Luc, Wenlei Zhu, Jun Jie Zhu, and Feng Jiao. A Highly Porous Copper Electrocatalyst for Carbon Dioxide Reduction. *Advanced Materials*, 2018. ISSN 15214095. doi: 10.1002/adma.201803111.

[56] Cao Thang Dinh, Thomas Burdyny, Golam Kibria, Ali Seifitokaldani, Christine M. Gabardo, F. Pelayo García De Arquer, Amirreza Kiani, Jonathan P. Edwards, Phil De Luna, Oleksandr S. Bushuyev, Chengqin Zou, Rafael Quintero-Bermudez, Yuanjie Pang, David Sinton, and Edward H. Sargent. CO2 electroreduction to ethylene via hydroxide-mediated copper catalysis at an abrupt interface. *Science*, 2018. ISSN 10959203. doi: 10.1126/science.aas9100.

[57] Fred C. Anson. Double-layer and electrode kinetics (Delahay, Paul). *Journal of Chemical Education*, 2009. ISSN 0021-9584. doi: 10.1021/ed043p54.2.

[58] H. Strathmann. *ION-EXCHANGE MEMBRANE SEPARATION PROCESSES*. 2004. ISBN 9780874216561. doi: 10.1007/s13398-014-0173-7.2.

[59] M C Porter. *Handbook of industrial membrane technology*. 1990. doi: 10.1016/0376-7388(90)80022-E.

[60] Xianhui Li and Jianxin Li. Fluxes and Driving Forces in Membrane Separation Processes. In *Encyclopedia of Membranes*. 2016. doi: 10.1007/978-3-642-40872-4{_}2197-1.

[61] F.G.Donnan. The theory of membrane equilibrium and membrane potential in the presence of a non-dialyzable electrolyte. A contribution to physical-chemical physiology. *Zeitschrift für Elektrochemie und angewandte physikalische Chemie*, 1911. ISSN 03767388. doi: 10.1016/0376-7388(94)00297-C.

[62] Toshikatsu Sata. *Ion Exchange Membranes Preparation, Characterization, Modification and Application*. 2002. ISBN 9780874216561. doi: 10.1007/s13398-014-0173-7.2.

[63] Tongwen Xu. Ion exchange membranes: State of their development and perspective, 2005. ISSN 03767388.

[64] Jin Ran, Liang Wu, Yubin He, Zhengjin Yang, Yaoming Wang, Chenxiao Jiang, Liang Ge, Erigene Bakangura, and Tongwen Xu. Ion exchange membranes: New developments and applications, 2017. ISSN 18733123.

[65] David M. Weekes, Danielle A. Salvatore, Angelica Reyes, Aoxue Huang, and Curtis P. Berlinguette. Electrolytic CO2 Reduction in a Flow Cell. *Accounts of Chemical Research*, 2018. ISSN 15204898. doi: 10.1021/acs.accounts.8b00010.

[66] Y. Hori, H. Ito, K. Okano, K. Nagasu, and S. Sato. Silver-coated ion exchange membrane electrode applied to electrochemical reduction of carbon dioxide. *Electrochimica Acta*, 2003. ISSN 00134686. doi: 10.1016/S0013-4686(03)00311-6.

[67] B. Smitha, S. Sridhar, and A. A. Khan. Solid polymer electrolyte membranes for fuel cell applications - A review. *Journal of Membrane Science*, 2005. ISSN 03767388. doi: 10.1016/j.memsci.2005.01.035.

[68] D. Woermann. Transport of ions against their concentration gradient across cation-exchange membranes with very small mechanical permeabilities. *Journal of the American Chemical Society*, 1968. ISSN 15205126. doi: 10.1021/ja01014a005.

[69] Mitsuru Higa, Akihiko Tanioka, and Keizo Miyasaka. Simulation of the transport of ions against their concentration gradient across charged membranes. *Journal of Membrane Science*, 1988. ISSN 03767388. doi: 10.1016/S0376-7388(00)82432-1.

[70] Meenesh R. Singh, Ezra L. Clark, and Alexis T. Bell. Effects of electrolyte, catalyst, and membrane composition and operating conditions on the performance of solar-driven electrochemical reduction of carbon dioxide. *Physical Chemistry Chemical Physics*, 2015. ISSN 14639076. doi: 10.1039/c5cp03283k.

[71] H. Strathmann, J. J. Krol, H. J. Rapp, and G. Eigenberger. Limiting current density and water dissociation in bipolar membranes. *Journal of Membrane Science*, 1997. ISSN 03767388. doi: 10.1016/S0376-7388(96)00185-8.

[72] Rachid El Moussaoui, Gérald Pourcelly, Maurice Maeck, Henry D. Hurwitz, and Claude Gavach. Co-ion leakage through bipolar membranes Influence on I-V responses and water-splitting efficiency. *Journal of Membrane Science*, 1994. ISSN 03767388. doi: 10.1016/0376-7388(94)80078-2.

[73] Charles C L McCrory, Suho Jung, Ivonne M. Ferrer, Shawn M. Chatman, Jonas C. Peters, and Thomas F. Jaramillo. Benchmarking Hydrogen Evolving Reaction and Oxygen Evolving Reaction Electrocatalysts for Solar Water Splitting Devices. *Journal of the American Chemical Society*, 2015. ISSN 15205126. doi: 10.1021/ja510442p.

[74] F. G. Wilhelm, N. F.A. Van Der Vegt, H. Strathmann, and M. Wessling. Comparison of bipolar membranes by means of chronopotentiometry. *Journal of Membrane Science*, 2002. ISSN 03767388. doi: 10.1016/S0376-7388(01)00696-2.

[75] Matthew D. Eisaman, Luis Alvarado, Daniel Larner, Peng Wang, Bhaskar Garg, and Karl A. Littau. CO2 separation using bipolar membrane electrodialysis. *Energy and Environmental Science*, 2011. ISSN 17545692. doi: 10.1039/c0ee00303d.

[76] J J Krol. Monopolar and bipolar ion exchange membranes. *Membrane Technology Group*, 1997.

[77] J. J. Krol, M. Wessling, and H. Strathmann. Concentration polarization with monopolar ion exchange membranes: Current-voltage curves and water dissociation. *Journal of Membrane Science*, 1999. ISSN 03767388. doi: 10.1016/S0376-7388(99)00133-7.

[78] J. Balster, M. H. Yildirim, D. F. Stamatialis, R. Ibanez, R. G.H. Lammertink, V. Jordan, and M. Wessling. Morphology and microtopology of cation-exchange polymers and the origin of the overlimiting current. *Journal of Physical Chemistry B*, 2007. ISSN 15206106. doi: 10.1021/jp068474t.

[79] Roel Van De Krol and Joop Schoonman. Photo-electrochemical production of hydrogen. In *Sustainable Energy Technologies: Options and Prospects*. 2008. ISBN 9781402067235. doi: 10.1007/978-1-4020-6724-2{_}6.

[80] Gabriele Centi, Siglinda Perathoner, Gauthier Winè, and Miriam Gangeri. Electrocatalytic conversion of CO2 to long carbon-chain hydrocarbons. In *Green Chemistry*, 2007. doi: 10.1039/b615275a.

[81] Danielle A. Salvatore, David M. Weekes, Jingfu He, Kevan E. Dettelbach, Yuguang C. Li, Thomas E. Mallouk, and Curtis P. Berlinguette. Electrolysis of Gaseous CO2 to CO in a Flow Cell with a Bipolar Membrane. *ACS Energy Letters*, 2018. ISSN 23808195. doi: 10.1021/acsenergylett.7b01017.

[82] Hanna Instruments. Benchtop pH meter HI5222-02. URL `https://www.hannainstruments.nl/toepassingen-meten-analyseren/benchtop-ph-mv-ise-meter-met-grafisch-kleurendisplay-en-complete-ki?c=454`.

[83] Masanobu Yamauchi. General Chemistry. 4th edition (Whitten, Kenneth W.; Gailey, Kenneth D.; Davis, Raymond E.). *Journal of Chemical Education*, 2009. ISSN 0021-9584. doi: 10.1021/ed069pa207.1.

[84] Jae Goo Shim, Dong Woog Lee, Ji Hyun Lee, and No Sang Kwak. Experimental study on capture of carbon dioxide and production of sodium bicarbonate from sodium hydroxide. *Environmental Engineering Research*, 2016. ISSN 2005968X. doi: 10.4491/eer.2016.042.

[85] Metrohm. 848 Titrino plus. URL https://www.metrohm.com/nl-nl/producten/titratie/titrino-plus/28480010.

[86] Solartron Analytical. Solartron Power Boosters. URL https://www.ameteksi.com/products/electrochemical-accessories/power-boosters/high-power-boosters.

[87] Radboud University. General Instrumentation ICP-OES. URL https://www.ru.nl/science/gi/facilities-activities/elemental-analysis/icp-oes/.

[88] JOHN W. OLESIK. ICP-OES. In *Encyclopedia of Materials Characterization*. 2013. doi: 10.1016/b978-0-08-052360-6.50059-x.

[89] John F. Watts. Encyclopedia of materials characterization. *Materials & Design*, 2003. ISSN 02613069. doi: 10.1016/0261-3069(93)90020-v.

[90] PerkinElmer. PerkinElmer Optima 5300. URL https://www.perkinelmer.com/.

[91] F. Malz and H. Jancke. Validation of quantitative NMR. *Journal of Pharmaceutical and Biomedical Analysis*, 2005. ISSN 07317085. doi: 10.1016/j.jpba.2005.01.043.

[92] EXW Foxboro. Table of conductivity vs concentration for common solutions, 1999.

[93] Electrical conductivity of aqueous solutions. URL https://sites.chem.colostate.edu/diverdi/all_courses/CRCreferencedata/electricalconductivityofaqueoussolutions.pdf.

[94] P.C. Ho and D.A. Palmer. Electrical Conductivity Measurement of Aqueous Boric Acid at 25-350C at Saturation Vapor Pressure, 1995. URL https://inis.iaea.org/collection/NCLCollectionStore/_Public/27/058/27058729.pdf.

[95] Laura Paltrinieri. Membrane for phosphate removal and recovery. URL https://www.wetsus.nl/includes/downloadFile.asp?id=ZTAxTmpNeU53PT1jNTQ%3D&date=e01c54.

[96] E. J. Billo. Modern Inorganic Chemistry (Jolly, William L.). *Journal of Chemical Education*, 2009. ISSN 0021-9584. doi: 10.1021/ed062pa137.1.

[97] Catherine E Housecroft and Alan G Sharpe. *Stability Constants of Coordination Complexes*. 2005. ISBN 0130399132.

[98] Mahendra Jain. Competition Science Vision. *Pratiyogita Darpan Group*, 2004.

[99] Shiran Shultz, Maria Bass, Raphael Semiat, and Viatcheslav Freger. Modification of polyamide membranes by hydrophobic molecular plugs for improved boron rejection. *Journal of Membrane Science*, 2018. ISSN 18733123. doi: 10.1016/j.memsci.2017.10.003.

[100] Jong Kil Park and Kun Jai Lee. Diffusion Coefficients for Aqueous Boric Acid. *Journal of Chemical and Engineering Data*, 1994. ISSN 15205134. doi: 10.1021/je00016a057.

[101] Thermochemical Radii - Anions. URL http://www.wiredchemist.com/chemistry/data/thermochemical-radii-anions.

[102] H. D. B. Jenkins and K. P. Thakur. Reappraisal of thermochemical radii for complex ions. *Journal of Chemical Education*, 2009. ISSN 0021-9584. doi: 10.1021/ed056p576.

[103] Qiang Zhang, Hailong Chen, Tianmin Wu, Tan Jin, Zhijun Pan, Junrong Zheng, Yiqin Gao, and Wei Zhuang. The opposite effects of sodium and potassium cations on water dynamics. *Chemical Science*, 2017. ISSN 20416539. doi: 10.1039/c6sc03320b.

A

I-V curves for pH differences over a BPM

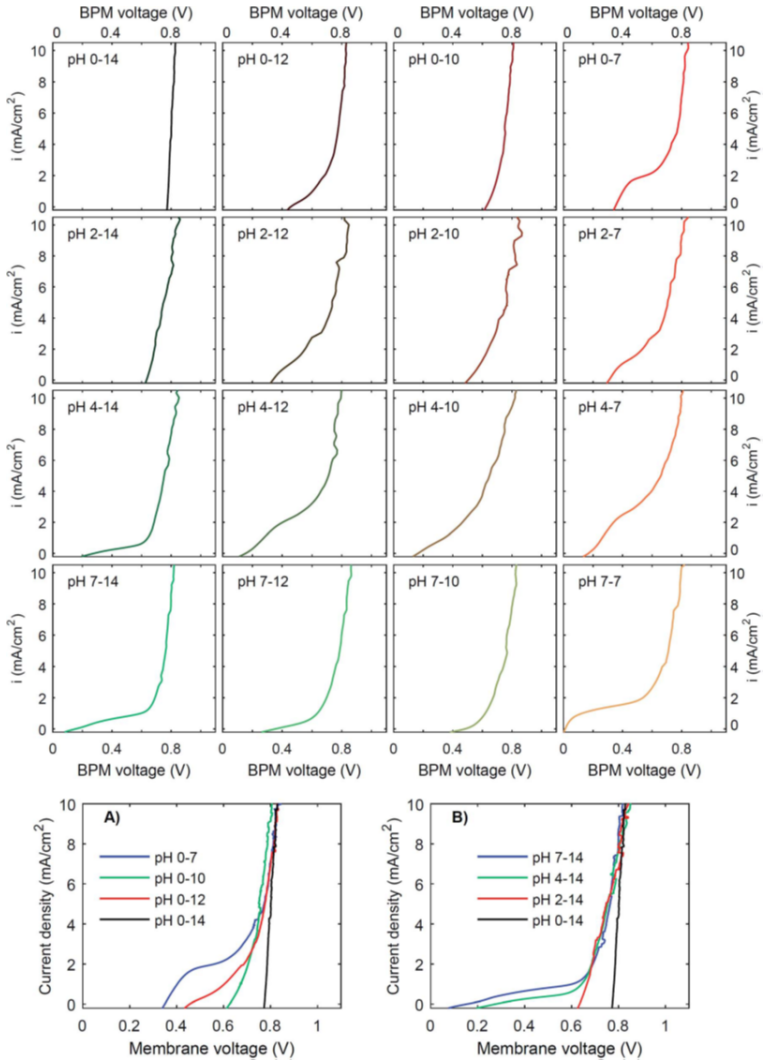

Figure A.1: I-V curves for pH differences over a bipolar membrane. Data are obtained from galvodynamic scans, from high current density (20 mA/cm^2/s) to low current density (-0.5 mA/cm^2/s), at a scan rate of 0.03 mA/cm^2/s. For comparison, selections of I-V curves are made with pH=0 in the catholyte (A) and pH=14 in the anolyte (B) [3].

B

BPM and flow-cell specifications

Table B.1: Fumasep BPM specifications [5].

Membrane	Bipolar
Thickness	130 - 160 µm (microns)
Appearance / Color	Transparent / Brown
Backing Foil	None
Delivery Form	Wet in NaCl solution
Reinforcement	PK
Density	15 - 17 mg cm-2
Counter Ion	Na (CEM layer) / Cl (AEM) layer
Max Temperature	40 °C
Dimensional Swelling in H_2O at 25 °C	0 %
Water Splitting Voltage at 100 mA cm^{-2}	< 1.2V
Water Splitting Efficiency at 100 mA cm^{-2}	> 98 %

Electrochemical Flow Cells

ElectroCell

Technical Data

(V1_2017)

SPECIFICATIONS	Micro Flow Cell	Electro MP Cell	Electro Syn Cell	Electro Prod Cell
Electrical data				
Projected electrode area, min. [m^2] [1]	0.001	0.01	0.04	0.4
Projected electrode area, max. [m^2] [2]	-	0.2	1.04	16
Current density, max. [kA/m^2] [3]	4	4	4	4
Electrode gap range [mm] [2]	0.7-8	2-16	1-5	1-10
Standard electrode gap [mm]	4	8	5	4
Dimensions				
Height [mm]	120	306	550	1030
Width [mm]	70	182	238	1040
Length [mm] [4]	> 33	> 38	> 43 [5]	> 300 [6, 7]
Pipe connections				
Connections	female 1/8" NPT	female 1/2" NPT	G1 1/2" (union 32mm)	Flanges [8]
Outer pipe diameter [10]	-	-	32mm	90mm
Electrolyte flow data				
Max number of separate flows (compartments) [9]	4	4	2	3
Electrolyte Flow per max. module, stack [L/min] [3, 11]	-	20-80	65-117	100-600
Electrolyte Flow per frame, Cell [L/min] [3, 11]	0.18-1.5	1-4	5-9	5-30
Electrolyte volume per frame, Cell [L] [2]	0.01	0.2	0.6	-
Flow rate in each cell [m/sec] [3]	0.05-0.4	0.03-0.12	0.2-0.38	0.05-0.4
Pressure drop in a module (water 25C) [kPa]	-	5-50	8-50	0.5-16
Max working temperature [2, 3]	-	-	-	-
Materials [9]				
Flow frame materials, standard	PTFE	PP, PVDF	PP, PVDF	PP, PVDF
Sealing, gasket materials, standard	EPDM, FPM (Viton)			
Ion exchange/selective membranes, diaphragms	Nafion, other various types			
End plate materials (not in contact with media)	Stainless steel			
Electrode materials:	Stainless steel, Ti, Ni, Hastelloy, Nb, Ta, graphite, Zn, Sn, Fe, Pb, Pt foil, …			
Coated electrodes	Pt on Ti, DSA® for Cl_2 or O_2 evolution (Ir-, Ru-MMO), PbO_2, Boron Doped Diamond, …			
3 dimensional electrode materials	Graphite/carbon (felt, granulate, RVC), Ni foam, Cu foam, …			
GDE sheet materials	Catalyzed and uncatalyzed types with/without metal screens			

Remarks:

1) Area can be minimized/modified on request
2) Depends on configuration and choice of sealing and frame materials
3) Depends on application, configuration and choice of electrode materials etc.
4) Depends on configuration and stack size (excl. Pipe/ connectors)
5) Max length approx 280mm at 1.04m^2 stack size
6) Max length approx 1160mm for 2 compartment 16m^2 stack size
7) Max length approx 1120mm for 3 compartment 12m^2 stack size
8) DIN 2501 PN 10. Others on request
9) Depends on Cell type. Other materials on request
10) In general use piping with large openings (ID) in order to avoid back pressure and improve gas release
11) Max working pressure 0.5 bar (50 kPa). For higher pressure consult your local ElectroCell representative

ElectroCell - ec@electrocell.com - www.electrocell.com

Figure B.1: Technical data for electrochemical flow-cells provided by ElectroCell [8]. In this research the Micro Flow Cell® and the Electro MP Cell®, column 1 and 2, respectively, were used.

C

Chemical specifications

Table C.1: Specifications of used chemicals for this research.

Chemical	Chemical formula	Company	Purity	Form
Tricine	$C_6H_{13}NO_5$	Sigma-Aldrich	>99%	Powder
Phosphoric acid	H_3PO_4	Sigma-Aldrich	>99%	Crystalline
Glycine	$C_2H_5NO_2$	Sigma-Aldrich	>99%	Powder
MOPS	$C_7H_{15}NO_4S$	Sigma-Aldrich	>99.5%	Powder
BES	$C_6H_{15}NO_5S$	Sigma-Aldrich	>99%	Powder
Potassium phosphate monobasic	H_2KPO_4	Sigma-Aldrich	>99%	Powder
Potassium phosphate dibasic	HK_2PO_4	Sigma-Aldrich	>98%	Powder
AMPSO	$C_7H_{15}NO_5S$	Sigma-Aldrich	>99%	Powder
Boric acid	H_3BO_3	Sigma-Aldrich	>99.5%	Powder
Potassium bicarbonate	$KHCO_3$	Sigma-Aldrich	>99.5%	Powder
CAPS	$C_9H_{19}NO_3S$	Sigma-Aldrich	>99%	Powder
Sodium hydroxide	NaOH	J.T.Baker	>99%	Pellets
Hydrobromic acid	HBr	Sigma-Aldrich	48 wt.% in H_2O	Solution
Potassium hydroxide	KOH	Sigma-Aldrich	45 wt.% in H_2O	Solution
Potassium sulfate	K_2SO_4	Sigma-Aldrich	>99%	Powder

Table C.2: pH modifications for buffer solutions.

Chemical solution (0.5M)	Initial pH	Modification	Final pH
Tricine	5.3	82.5 mL 1M HBr	2.0
Glycine	6.3	142.0 mL 1M HBr	2.4
MOPS	3.6	91.8 mL 1M KOH	7.2
BES	2.9	106.0 mL 1M KOH	7.1
AMPSO	3.0	8.9 mL saturated KOH	9.1
Boric acid	3.7	105.0 mL 1M KOH	9.2
Potassium bicarbonate	8.4	169.0 mL 1M KOH	10.3
CAPS	4.2	8.6 mL saturated KOH	10.4

D

NMR spectroscopy results

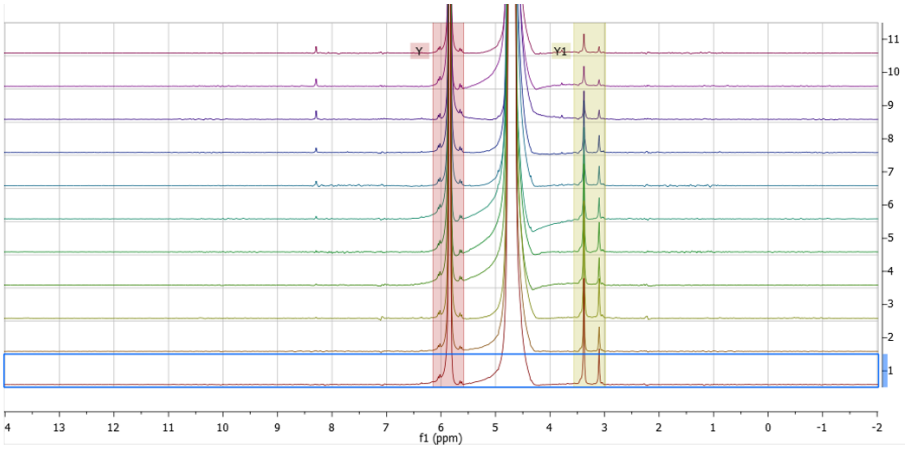

Figure D.1: Quantitative NMR spectroscopy results for tricine ion cross-over in NaOH samples. The tricine peak at 3.4 ppm decreases from 1 to 11 (0-150 mA/cm^2).

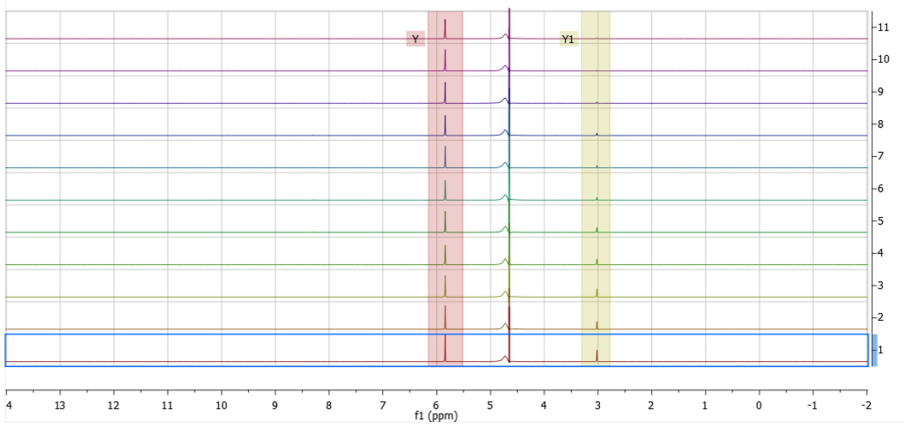

Figure D.2: Quantitative NMR spectroscopy results for glycine ion cross-over in NaOH samples. The glycine peak at 3.0 ppm decreases from 1 to 11 (0-150 mA/cm^2).

E

I-V curves and co-ion permeation for glycine and tricine with standard deviation

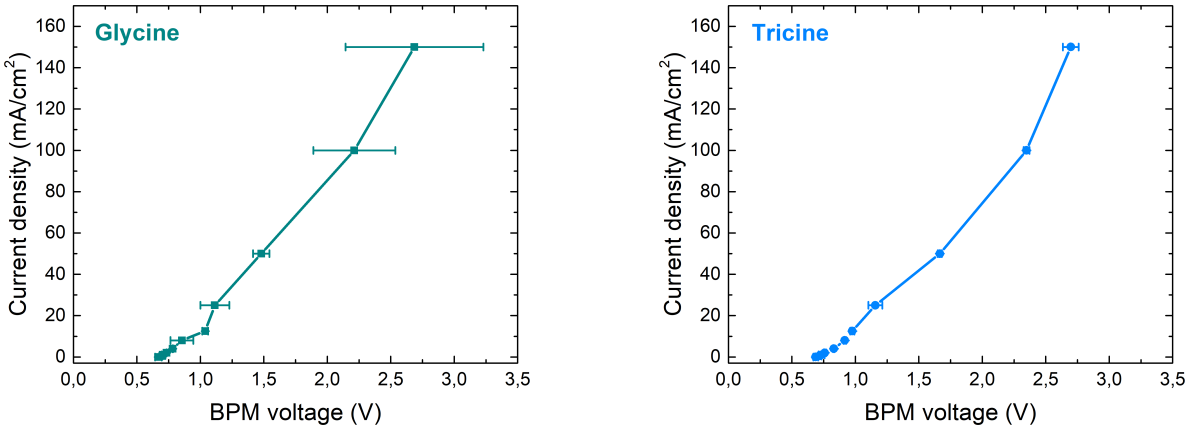

(a)

(b)

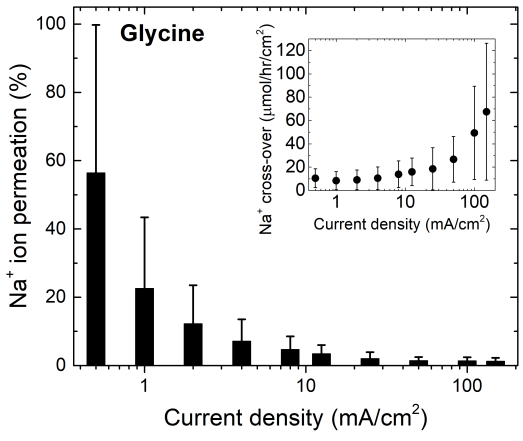

(c)

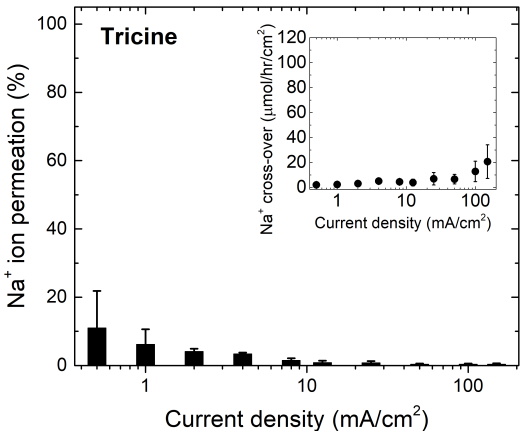

(d)

Figure E.1: Graphs displaying an I-V curve for a current density range of 0 - 150 mA/cm^2 versus the BPM voltage (V) for glycine (a) and tricine (b), and graphs displaying the Na^+ permeation from the anolyte to the catholyte for glycine (c) and tricine (d). The catholyte is a 0.5M tricine solution and the anolyte is a 0.5M NaOH solution. All measurements (45 minutes) have been performed twice and the standard deviation of these results is indicated by an error bar.